University of Nottingham

School of Physics and Astronomy

X-ray Magnetic Circular Dichroism Studies of III-Mn-V Compounds and Heterostructures

Author:

Peter Wadley, Mphys

Supervisor:

Dr. Kevin Edmonds

Thesis submitted to the University of Nottingham

for the degree of Doctor of Philosophy

March 2012

Contents

Acknowledgements

Firstly and foremost I would like to thank my supervisor, Dr Kevin Edmonds, without whose unparalleled support, patience, encouragement and ideas, my PhD would have been less rewarding, less successful and less fun. I would also like to express my gratitude to the entire physics department of the University of Nottingham. It has been a very supportive, stimulating and professional place to have studied.

I have been helped and encouraged by so many people along the way, but I would like to say thank you in particular to: Andrew Rushforth for help with many things, advice, encouragement and collaboration. Richard Campion for growing all of the samples perfectly, and also for many useful and philosophical discussions. Laurence Eaves and Amalia Patane for their time and enthusiasm with some very good, additional, experiments outside of my thesis studies. Brian Gallagher for very useful and always interesting discussions. Stuart Cavill, Sarnjeet, Dhesi, Elke Arenholz, Andrei Rogalev, Alevtina Smekhova and Fabrice Wilhelm for a huge amount of support during beamtimes. Gerrit van der Laan for support, humour, insights and some great selected reading. Chris Staddon, Nicola Farley and Jackie Hall for teaching me how to use the XRD machine and how to understand the results, and for patience with my endless requests for machine time.

I would also like to thank my fellow PhD students for all of the help and company they have given: Adam Freeman, Antonia May, Arianna Casiraghi, Duncan Parkes, Jackie Hall, James Haigh, Lucy Goff, Mu Wang, Marta Terramoto, Robin Marshall, Ryan Beardsley, Suzi Abbs, Victoria Grant.

A special thank you is reserved for my family, who have all been supportive in their different ways from start to finish.

Lastly I would like to thank Dominique Brady for putting up with me during the writing up period, and for help and support throughout.

List of Publications

[1] Wadley, P., Freeman, A. A., Edmonds, K. W., van der Laan, G., Chauhan, J. S., Campion, R. P., Rushforth, A. W., Gallagher, B. L., Foxon, C. T., Wilhelm, F., Smekhova, A. G., and Rogalev, A. (2010). Element-resolved orbital polarization in (III,Mn)As ferromagnetic semiconductors from K -edge x-ray magnetic circular dichroism. *Phys. Rev. B*, 81(23):235208.

[2] Wadley, P., Casiraghi, A., Wang, M., Edmonds, K. W., Campion, R. P., Rushforth, A. W., Gallagher, B. L., Staddon, C. R., Wang, K. Y., van der Laan, G., and Arenholz, E. (2011). Polarized x-ray spectroscopy of quaternary ferromagnetic semiconductor (Ga,Mn)(As,P) thin films. *Applied Physics Letters*, 99(2):022502.

[3] Olejnik, K., Wadley, P., Haigh, J. A., Edmonds, K. W., Campion, R. P., Rushforth, A. W., Gallagher, B. L., Foxon, C. T., Jungwirth, T., Wunderlich, J., Dhesi, S. S., Cavill, S. A., van der Laan, G., and Arenholz, E. (2010). Exchange bias in a ferromagnetic semiconductor induced by a ferromagnetic metal: Fe/(Ga,Mn)As bilayer films studied by XMCD measurements and SQUID magnetometry. *Phys. Rev. B*, 81(10):104402.

[4] Casiraghi, A., Rushforth, A. W., Wang, M., Farley, N. R. S.,Wadley, P., Hall, J. L., Staddon, C. R., Edmonds, K. W., Campion, R. P., Foxon, C. T., and Gallagher, B. L. (2010). Tuning perpendicular magnetic anisotropy in (Ga,Mn)(As,P) by thermal annealing. *Applied Physics Letters*, 97(12):122504.

[5] Mäca, F., Masek, J., Stelmakhovych, O., Marti, X., Reichlova, H., Uhlirova, K., Beran, P., Wadley, P., Novak, V., and Jungwirth, T. (2012). Room-temperature antiferromagnetism in CuMnAs. *Journal of Magnetism and Magnetic Materials*, 324(8):1606 – 1612.

Abstract

This thesis describes the characterisation of (Ga,Mn)As, related compounds and heterostructures. (Ga,Mn)As and other (III,Mn)V compounds have provided many interesting insights into fundamental physics, and are of considerable potential interest commercially in the field of spintronics. This study examines a set of samples grown by molecular beam epitaxy and characterised using several techniques: primarily this study makes use of the x-ray absorption techniques, x-ray magnetic circular dichroism(XMCD) and x-ray absorption spectroscopy (XAS). In addition, x-ray diffraction (XRD), transport measurements and super conducting quantum interference device (SQUID) magnetometry were used as complimentary techniques.

(Ga,Mn)As layers with epitaxial Fe grown on top, are shown to have a sub-nanometre interfacial layer which remains polarised above room temperature. A detailed understanding of these systems is obtained by applying the element specific nature of XMCD in combination with two different probing depths to explore separately the nature of the coupling of the bulk and interfacial region. The coupling between the interfacial layer and the Fe is shown to be strongly antiferromagnetic (AF). A weaker coupling is also shown to exist between the Fe and the bulk of the (Ga,Mn)As layer below the Curie temperature (T_C). This coupling is also AF at low fields, leading to an exchange bias for the entire layer.

Doping of (Ga,Mn)As with P is shown to have several effects on the magnetic properties of the (Ga,Mn)As layer. Changes in the layer strain are observed using high resolution XRD. This strain also manifests itself in the Mn $L_{3,2}$ XMCD spectra and the relationship between the two is shown to be linear. A pronounced effect on the magnetic anisotropy is observed using SQUID measurements, with the easy axis switching from in-plane, in the compressively strained (Ga,Mn)As, to out-of-plane in the higher doped (Ga,Mn)(As,P) layers. A decrease in total magnetic moment per Mn atom and T_C are observed with increased doping. This

is inferred not to be due to a direct effect of the P on the local surrounding of the Mn ions, owing to the striking similarity of the XMCD spectra. This is instead attributed to reduced participation of Mn ions in the magnetic ordering.

Finally, K edge XMCD is used to reveal the element specific nature of unoccupied states near the Fermi level in a set of (Ga,Mn)As and (In,Ga,Mn)As samples with differing Mn doping levels . The character of the holes in low-doped samples is shown to be markedly different than for those in the highly doped metallic samples. A transfer of orbital magnetic moment from the Mn to the As sites is observed on crossing the metal-insulator transition, with the large XMCD on Mn sites in low doped samples interpreted as a sign of hole localisation around the Mn ion.

Chapter 1

Introduction

Preface

This thesis study is concerned with the fundamental properties and behaviour of a class of materials called dilute magnetic semiconductors (DMS). In particular (Ga,Mn)As and related compounds and heterostructures. The purpose of this chapter is to provide some background on the material systems which are the focus of this study, and the motivation behind their continued research.

1.1 Background

The field of spintronics is concerned with the study of spin related electronic transport behaviour. Spintronic devices are those which rely partly or entirely on the spin property of electrons rather than solely their charge, which is the case for the majority of commercial electronics at time of writing. The development of spintronics into a highly active area of research came with the discovery of giant magnetoresistance (GMR) by Baibich *et al.* in 1988 [1], which demonstrated that the transport properties of a device could be significantly altered through spin manipulation alone. The technological significance of GMR was realised immediately and found multiple applications, perhaps the most significant of which was as a magnetic field sensor in the read heads of hard disks. In 2007 Albert Fert and Peter Grünberg were awarded the Nobel prize for the discovery of GMR.

Spintronics has been rapidly driven forward by the prospect of a new generation of devices which use the spin property of electrons to provide faster and more efficient operation and entirely new functionality. Despite this long standing promise, many of these functionalities are yet to be realised at practical temperatures, owing to the many difficulties of working with and preserving spin polarisation. Many potential benefits and new functionalities for spintronic devices were summarised by Wolf *et al.* [2]. However, significant obstacles have prevented spintronics from fulfilling this potential. Many of these difficulties arise when trying to replicate existing functionality, such as logic gates, at room temperature. This stems from the fact that although it is easy to generate a spin polarised current at room temperature, it is not easy to do so in a material which is gateable. Broadly speaking this has lead to two different material approaches to circumventing this issue, utilising dilute magnetic semiconductors and ferromagnetic metals respectively.

With the metal based approach it is easy to realise spin polarisation at room temperature as ferromagnetic metals have inherently spin-polarised electron bands. The big advantage of this approach is that there are an abundance of room temperature ferromagnetic metals, however they are difficult to integrate with existing technologies. Since it is usually not possible to gate or dope metals in the same way as you can semiconductors, devices such as transistors are more difficult to construct. For more complex functionality it is necessary to inject or in some way convey the spin polarised current into a medium where further functionality is possible.

Another approach, which is perhaps more elegant, is taken by doping a semiconductor with magnetic ions until it becomes itself magnetic. These materials are called dilute magnetic semiconductors (DMS) and are the subject of this study. The successful incorporation of magnetic ions into a semiconductor lattice means that the resulting compound can still be sensitive to gating and doping, an important advantage over metal based spintronics. This offers the possibility of realising the rich functionality afforded by semiconductors combined with the spin polarised currents of a ferromagnet, and offers the exciting prospect of persistent memory and logic applications on a single device. In addition, information encoded in electron spins is potentially suitable for quantum computing applications, and ultrafast manipulation of spin using optical pulses has been previously demonstrated [3]. This hints at the possibility of integrating photonics and quantum computing with spintronics.

1.2 (Ga,Mn)As as a dilute magnetic semiconductor

Although a lot of earlier work on DMS focused on the (II,VI) systems, most of the resulting materials were at best paramagnetic [4]. These materials tend to be insulating and difficult to dope with electrons or holes. The discovery of ferromagnetism in (In,Mn)As and subsequently (Ga,Mn)As, where Mn is a p-type dopant, pushed these materials to the forefront of DMS research. (Ga,Mn)As has established itself as the most studied DMS for a few reasons: It exhibits robust ferromagnetism with Curie temperatures (T_C) of up to 185 K at time of writing, and it is based on the second most widely used semiconductor, and so provides ready integration with existing technologies. It can be grown pseudomorphically on top of GaAs. In terms of fundamental research (III,V) DMS have already provided a rich playground for the study of the interplay between magnetic and electronic properties, and led to several important experimental achievements. These include spin injection into a non magnetic material [5], bias voltage control of the ferromagnetic to paramagnetic phase transition [6], electric field assisted magnetisation reversal [7], and current-driven domain wall dynamics [8]. Two other important effects first observed in (Ga,Mn)As are tunnelling anisotropic magnetoresistance (TAMR) [9] and Coulomb blockade anisotropic magnetoresistance (CBAMR) [10].

However, for (Ga,Mn)As to become commercially viable the T_C needs to be extended comfortably above room temperature. After its inception, the T_C of (Ga,Mn)As quickly rose from ~ 60 K to 110 K mainly through improvements in growth technique. This remained the upper limit for some years and was suggested as a fundamental limit for (Ga,Mn)As. This limit was exceeded by the technique of low temperature annealing, which proved hugely successful in improving material quality [11]. At time of writing the T_C of (Ga,Mn)As has peaked at around 185 K and further efforts to improve this have met with diminishing returns.

1.3 Growth of (III,V) DMS

The growth of (III,V) DMS was initiated by Munekata et al [12] with the growth of (In,Mn)As using a technique called molecular beam epitaxy (MBE). MBE is essentially a form of crystal growth performed in ultra high vacuum(UHV) conditions [13]. The experimental set-up involves several solid(or sometimes liquid)

effusion cells which are heated until sublimation(or evaporation) occurs. These cells are separated from the target substrate by shutters. When the shutters are open atomic or molecular beams impact from the cells directly onto the target. The temperature of the target is carefully controlled so as to prevent re-evaporation but allow a certain amount of reordering to occur on the target. The sample growth is monitored using the technique of reflection high energy electron diffraction (RHEED). RHEED uses low angle electron reflection, which is so surface sensitive that it relies primarily on the top layer of atoms [14]. In this way it is possible to see, and measure, the surface reconstruction. Combined with the low deposition rates of MBE, this enables carefully monitored epitaxial growth. In addition, since the growth rate is slow in comparison to the shutter speeds, atomically sharp interfaces are possible.

Mn solubility in (III,V) semiconductor lattices is very poor, and initial efforts resulted in phase segregation and the formation of ferromagnetic MnAs. While growing (In,Mn)As, Ohno et al found by lowering the growth temperature, enough energy existed for some surface reordering but not enough for secondary phases to form [15]. In this way it was possible to include Mn substitutionally, at higher doping levels. The resulting material was mainly paramagnetic but had a component that appeared to be ferromagnetic below 10 K. A report on the magnetotransport properties of (In,Mn)As revealed large negative magnetoresistance as well as a dominant anomalous Hall effect (AHE), and also went on to briefly introduce a new class of (III,V) DMS, (Ga,Mn)As [16]. Ohno et al revisited (Ga,Mn)As in 1996 [17] and showed that incorporation of Mn into GaAs produced a DMS which was robust with a higher T_C than ever seen before (~ 60 K).

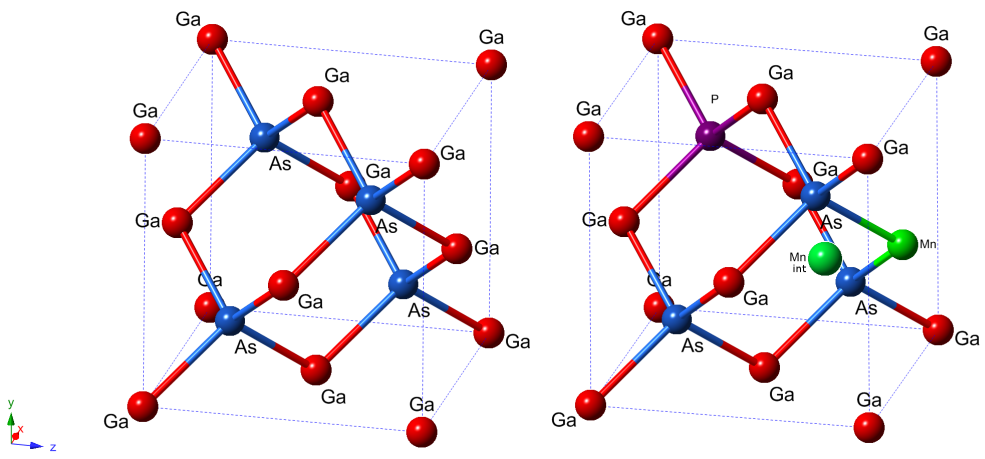

Figure 1.1 – Mn and P incorporated into a GaAs zinc blende lattice. In one case the Mn is shown substituting for Ga and in one case sitting interstitially. The P is shown substituting for As

1.4 Properties of (Ga,Mn)As and related compounds

1.4.1 Structure

The structure of (Ga,Mn)As and the other alloys of (Ga,Mn)As presented here is that of the zinc-blende GaAs structure, which comprises two individual face centred cubic lattices (FCC), one of As and one of Ga, offset along the cell diagonal by one quarter of the lattice parameter. (Ga,Mn)As ideally differs from GaAs only by a dilute amount, typically 1-8%, of Mn atoms substituting directly for the Ga atoms(Mn_{Ga}). Figure 1.1 (a) shows the zinc-blende cubic structure of GaAs, and (b) shows a unit cell of (Ga,Mn)(As,P) (this differs from (Ga,Mn)As only by the substitution of P for As), where one Ga atom has been replaced by Mn_{Ga}, and one Mn is trapped interstitially (Mn_{int}).

The room temperature lattice parameter of GaAs is $a_0 = 5.654\,\text{Å}$. Mn substituting for Ga is found to increase the lattice size in a linear fashion, in accordance with Vegard's Law [18]. Since (Ga,Mn)As is usually grown pseudomorphically on top of GaAs this leads to a compressive strain being present in thin films. This strain tends to distort the (Ga,Mn)As unit cell as it seeks to lattice match with the GaAs substrate. The result is a tetragonal structure, matched to GaAs in the *ab* plane, and elongated along the *c* direction. The degree of distortion depends on the doping and defect density.

In Figure 1.1 (b), an example cell of (Ga,Mn)(As,P) is shown. In this example, as well as one Ga atom being replaced by Mn, an As atom is also replaced by P. In (Ga,Mn)(As,P) two competing factors determine the lattice parameter, and hence resultant strain. In contrast to Mn, P doping decreases the lattice constant, and so in (Ga,Mn)(As,P) it is possible to have either compressive or tensile strain in the film. Spectroscopic fingerprints of the tunable strain in this system are presented in Chapter 4.

The highly non-equilibrium conditions of (Ga,Mn)As growth means that as the doping is increased interstitial defects become increasingly favourable energetically. The most common defect is the Mn_{int}, whereby a Mn atom becomes trapped in the lattice but not on a lattice site. The interstitial Mn has a double

effect on the (Ga,Mn)As properties. It has been shown to bond antiferromagnetically to substitutional Mn [19], effectively removing the moment contribution of this Mn atom. Also, as the Mn interstitial is unbonded, it donates its two outer $4s$ valence electrons, which decreases the hole density. Another possible defect is the As-antisite defect, this occurs when an As atom sits on a Ga site.

The interstitial Mn can be effectively removed from (Ga,Mn)As films by annealing in air at temperatures $\sim 180-250°\mathrm{C}$ which is comparable to or lower than the growth temperature. Due to the weak bonding of Mn_{int}, the energy barriers to diffusion are low, so they are highly mobile at these temperatures. Diffusing Mn_{int} that reach the film surface are oxidised and effectively removed from the lattice, resulting in measured increases in conductivity and T_C [11].

Mn_{int} and As antisite defects both increase the lattice constant in (Ga,Mn)As, leading to a larger compressive strain. Since the incorporation of these defects is strongly dependent on the growth conditions, the obtained lattice constant for a given Mn concentration can vary significantly from sample to sample [20]. A detailed study of as-grown and annealed (Ga,Mn)As films prepared in Nottingham has yielded a lattice constant a that varies with the fractional concentrations of substitutional Mn (f_{sub}) and interstitial Mn (f_{int}) as $a = a_0 + (0.26 \pm 0.08)f_{sub} + (0.6 \pm 0.2)f_{int}$ [18].

1.4.2 Electronic and electrical properties

Undoped GaAs is a direct band-gap semiconductor with $E_G = 1.5\,\mathrm{eV}$. The electronic behaviour of Mn in this system depends strongly on the doping level. At low doping levels,$\sim$ 0.01% or less, Mn is an acceptor with binding energy $E_a = 110\,\mathrm{meV}$. This places it somewhere between shallow acceptors, such as C, Be, Mg, and Zn with $E_a \sim 30\,\mathrm{meV}$, and deep impurity levels, such as Fe, Co or As antisite defects [21]. With increased doping the Mn acceptor wavefunctions begin to overlap resulting in the formation of an impurity band. Figure 1.2 depicts this process diagrammatically. At concentrations above $\sim 1.5\%$ low temperature metallic conduction is observed. This is believed to be due to the merging of the Mn impurity band with the disorder-broadened host valence band. At this point the states at the Fermi level are no longer bound to the individual Mn atoms, but become delocalised across the system, leading to a metallic ground state. This model is disputed by some authors who speculate the continued existence of a

separated impurity band in the metallic regime [22, 23].

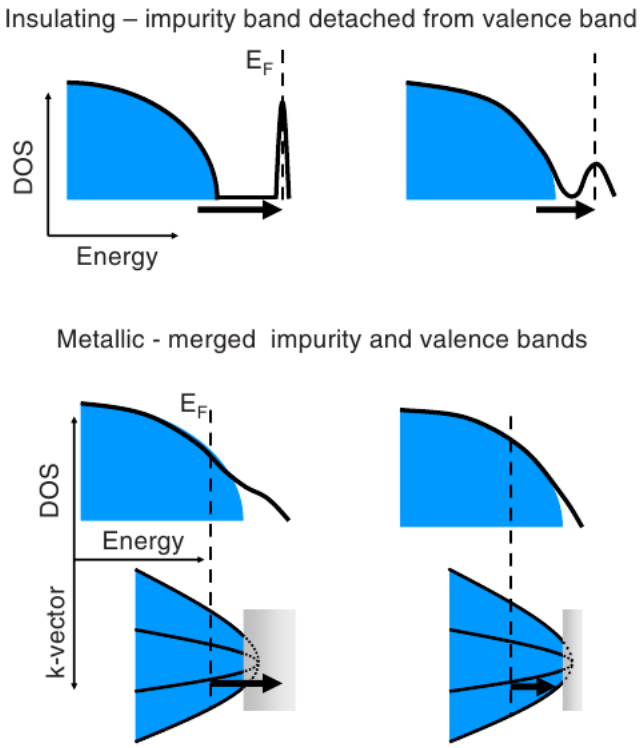

Figure 1.2 – Schematic illustration of the band structure in the insulating and metallic regimes of (Ga,Mn)As. In both case the doping increases from left to right. The isolated acceptor levels are shown initially broadening into separate impurity band, and then in the metallic case merging with the host valence band. The blue regions of the spectra represent itinerant states whereas the white and grey regions show localised states. The black arrows represent the redshift in the impurity band ionisation energy(top) and the inter-valence-band transitions (bottom). Reproduced from a paper by Jungwirth *et al* [21].

1.4.3 Magnetic properties and the Curie temperature

Ferromagnetic ordering (FM) in (Ga,Mn)As first occurs for Mn concentrations of $\sim$ 1%, just below the concentration at which metallic conduction at low temperature is first observed. Figure 1.3 shows the T_C for a series of annealed (Ga,Mn)As films versus magnetisation, which is proportional to the concentration of uncompensated substitutional Mn. The T_C increases approximately linearly with the substitutional Mn (Mn_{Ga}) concentration, but also depends on the concentration of interstitial Mn (Mn_{int}) and other compensating defects which suppress FM order. Large increases in T_C can be achieved by post-growth annealing as discussed in Section 1.4.1, due to the removal of Mn_{int}.

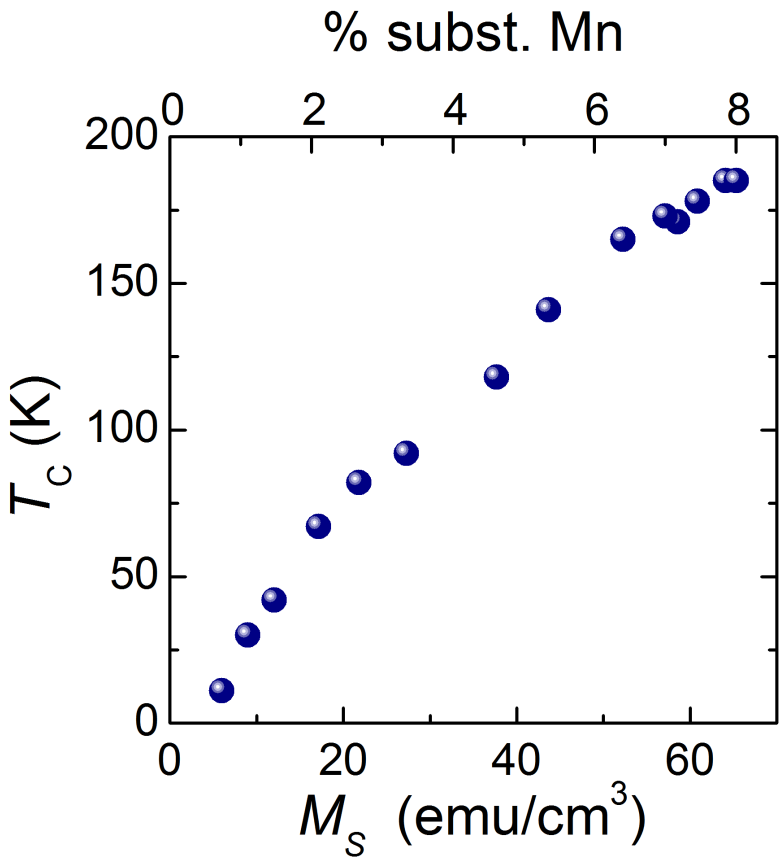

Figure 1.3 – Curie temperature versus magnetisation for set of annealed (Ga,Mn)As films with varying substitutional Mn concentration. Data taken from Jungwirth *et al* [24] and Wang *et al* [25].

Since substitutional Mn in (Ga,Mn)As has one less outer electron for bonding it provides a hole when occupying a Ga site. It is these holes, which couple antiferromagnetically to the Mn moments, that mediate the ferromagnetism. This ensures that the electronic and magnetic properties are inextricably linked. One of the simplest models of this indirect exchange interaction was proposed by Dietl et al [26], by applying the Zener model, originally conceived for transition metals, to the case of p-type zinc-blende DMS. In highly doped metallic (Ga,Mn)As the interconnected magnetic and electrical properties are well reproduced by such models, where the holes are considered to occupy a host-like valence band, which is split into sub-bands due to strain, exchange and spin orbit interactions [24, 27–29]. Whereas, in the more dilute insulating regime, models which have holes that reside in a narrow impurity band are more commonly used [23, 30]. The half filled Mn $3d$ shell provides a local magnetic moment of $\sim 5\,\mu_B$. The average separation

of Mn is of the order of nm, which means that direct interaction, which favours antiferromagnetic coupling, is weak (except in the case of interstitial Mn). The indirect exchange interaction sees the holes bonded antiferromagnetically to the Mn, and since the holes themselves possess a spin moment of $\sim 1\ \mu_B$, this reduces the average moment per Mn.

1.4.4 Spin-orbit coupling and magnetocrystalline anisotropy

At the heart of many of the useful and interesting phenomena displayed by (Ga,Mn)As is the relativistic effect of spin orbit coupling(SOC). The SOC is a coupling between the spin magnetic moment and orbital magnetic moment of an electron and its origin is perhaps most easily deduced from the rest frame of the electron. From the electrons rest frame the positively charged nucleus is an orbiting charge producing a magnetic field which exerts a torque on the electron's spin moment. Any attempt to reorientate the spin moment of the electron also exerts a torque on the orbital moment, and hence the two become coupled. This coupling is, to a large extent, the origin of the magnetocrystalline anisotropy observed in (Ga,Mn)As films. The total magnetic anisotropy is determined by a number of components, the most important of which are shape anisotropy and magnetocrystalline anisotropy.

Shape anisotropy is the result of energy minimisation of the stray magnetic field. Magnetic poles form at the domain boundaries, which are the surfaces in the case of a single domain ferromagnet. The minimum energy configuration is determined by lowest amount of stray field. For a thin film, for instance, this occurs when the magnetisation is in-plane, as this minimises the number of magnetic poles at the film surface. This effect is typically strong in ferromagnetic metals where the moment density is large, but for DMS like (Ga,Mn)As, where the moments are dilute, shape anisotropy is usually weak.

Magnetocrystalline anisotropy (MCA) is a direct result of the SOC [31], and is a dependence of the lowest energy magnetisation direction on the symmetry of the crystal lattice. In DMS such as (Ga,Mn)As, where shape anisotropy is weak, strain largely determines the nature of the magnetic anisotropy. In (Ga,Mn)As in the metallic regime, compressive strain results in a MCA favouring an in-plane magnetic easy axis, while tensile strain results in a perpendicular-to-plane easy axis. The dependence on strain is often found to be reversed in the insulating

regime. The p-d Zener model of Dietl *et al* [26] gives qualitatively good agreement with these experimental observations in the metallic regime as well as for highly Mn doped and compensated films. A possible explanation for the MCA observed in the low-doped insulating regime is given in Chapter 5.

Other significant components of the MCA in (Ga,Mn)As include a cubic anisotropy favouring magnetisation along the $\langle 1\,0\,0 \rangle$ crystalline axes (due to the cubic symmetry of the Mn lattice sites); and an in-plane uniaxial anisotropy which breaks the symmetry between the $[1\,\bar{1}\,0]$ and $[1\,1\,0]$ crystalline axes. The origin of the latter is not fully understood but is related to the anisotropy of the $(0\,0\,1)$ GaAs growth surface.

1.5 Magnetic coupling at interfaces

The coupling between magnetic layers or structures can take several forms, the simplest of which is magnetostatic coupling, where the coupling occurs through the stray magnetic fields interacting. This form of direct interaction can lead to both parallel and anti-parallel coupling. A smooth interface between the layers favours antiferromagnetic coupling through the interaction of the stray fields at the sample extremes. Roughening of the interface can cause ferromagnetic coupling, this effect is sometimes called *orange peel* or Néel coupling. In thin film heterostructures, where the interfaces can be atomically smooth, magnetostatic coupling is often difficult to separate from the quantum mechanical exchange interaction, which is frequently much stronger.

The simplest form of magnetic interface occurs at the surface of a bulk ferromagnet, where the uppermost layers often have different saturation magnetisation and magnetic anisotropy. The exchange interaction is normally weakened as the surface is approached as a result of lower number of nearest neighbours, and the magnetic anisotropy is often enhanced. One cause of this is that the orbital moment is no longer as strongly quenched [32], and there can also be a significant magnetostatic contribution if the bulk moment favours an out-of-plane direction. As one might reasonably expect, these effects become increasingly important in the case of thin film structures, where the interface areas are comparatively large.

Exchange coupling between magnetic layers is the basis of many technologi-

cally important phenomena such as GMR and exchange bias. Exchange coupling between an antiferromagnetic and ferromagnetic layer in direct contact was discovered in the 1950's by Meiklejohn *et al* [33]. Interlayer exchange coupling was later shown to persist through a non-magnetic spacer, and the sign of the coupling was shown to vary with the thickness of the spacer layer [34]. The interlayer exchange coupling energy, which determines the ground state configuration of coupled layers, was shown to be due to the spin polarisation of conduction carriers in metallic systems [35]. Jungwirth *et al* used a mean field theory approach to predict that such interlayer coupling was also possible in entirely semiconductor heterostructures [36], which was subsequently demonstrated by Chung *et al* using (Ga,Mn)As with Be doped GaAs spacers [37].

Exchange bias is a remarkable consequence of exchange coupling, usually between a ferromagnet and an antiferromagnet. It manifests as a shift from zero of the magnetic hysteresis loop of the ferromagnetic layer (or softer ferromagnetic layer in the case of two ferromagnets). This shift is caused by the exchange coupling to the antiferromagnetic layer (or ferromagnet layer with a greater coercive field) and results in a unidirectional exchange anisotropy. This shift can be so large that the entire hysteresis loop of the ferromagnetically softer layer can be shifted above or below zero field. Exchange bias has been demonstrated in (Ga,Mn)As layers capped with antiferromagnets including MnO [38] and IrMn [39].

1.6 Recent developments in (III,Mn,V) DMS

In the ongoing search for higher T_C materials alloying with other elements has long been used to alter the properties of DMS through mechanism such as altering the p-d exchange interaction. For (Ga,Mn)As, P doping has been the subject of several recent studies [40–45]. Theoretical work by Masek *et al* [46] predicted an enhanced T_C for (Ga,Mn)As when alloyed with P. They utilised the relationship between the band offsets and lattice parameters of GaAs, AlAs and GaP, whereby AlAs and GaP share almost identical band positions (see Figure 1.4), and GaAs and AlAs share very similar lattice parameters. This enabled them to disentangle the effects caused by the position of the Mn derived states from the valence band edge (which depends largely on the host band positions according to the internal reference rule [47]) and those caused by the overlap of the anion orbitals (which depends on the lattice parameters).In their report *ab initio* LDA+U calculations are used to show that the strength of the magnetic interactions between the hole and

Mn spins are more sensitive to the overlap of the anion orbitals meaning that the reductions in lattice parameter should lead to increased T_C via this mechanism. In addition, they predict that that the formation energy of Mn_i compensating defects is increased which should lead to extra increase in T_C. Elsewhere Xu *et al* predict little dependence of T_C on P doping [48]. However, as noted by Masek *et al* [46], this study focused on the impurity band double exchange mediation mechanism which has been shown to be less relevant in high quality MBE grown (Ga,Mn)As and therefore may not be applicable for MBE grown low P doped samples.
Experimental reports on MBE grown P doped (Ga,Mn)As report favourable micromagnetic properties [43,44] and a strong dependence of the magnetic anisotropy on the doping induced strain. Similar trends are seen in ion implanted (Ga,Mn)(As,P) samples studied by Stone *et al* [41]. Both Rushforth *et al* [43] and Stone *et al* [41] report a suppression of the T_C with increasing P doping, in contrast to the predictions of Masek *et al*. Despite the presence of a large number of reports considering the magnetic and transport properties of (Ga,Mn)(As,P) studies of the micromagnetic origin of these properties are so far lacking. Detailed XMCD measurements of MBE grown (Ga,Mn)(As,P) are presented in Chapter 4.

Another approach to circumventing the issue of low T_C is seen in studies by Maccherozzi *et al* [49] and Sperl *et al* [50]. In these studies a proximity polarisation effect is reported in a surface population of Mn atoms in (Ga,Mn)As which persists up to and above room temperature. The polarisation is induced by the proximity of a ferromagnetic Fe layer. Despite a very detailed analysis of the samples in both reports, the preparation of the samples and interpretation of the results raise some questions about what is happening at the interface. In both cases the Fe layer is deposited post-growth after Ar sputtering of the (Ga,Mn)As surface. The highly non-equilibrium growth conditions of (Ga,Mn)As combined with the sputtering could impact the quality and nature of the Fe/(Ga,Mn)As interfacial region. This is particularly relevant given that the estimated polarisation depth is of the order of a few monolayers. Despite these questions the possibility of a room temperature ferromagnetically ordered (Ga,Mn)As layer is an exciting prospect and could reveal information about the nature of the ordering in (Ga,Mn)As as well as offering the possibility of some interesting metal/DMS hybrid structures for spintronic application. In Chapter 3 these shortcomings are addressed by studying similar structures grown entirely in situ without breaking vacuum by MBE.

One of the most hotly contested topics in the area of (Ga,Mn)As and related alloys is the precise character of the mediating holes. The transport and magnetic

properties of (Ga,Mn)As vary over a large range with the level of Mn doping, such that two distinct ranges exist. For doping levels below approximately 2%, (Ga,Mn)As is insulating or semi-insulating. At doping levels higher than this it becomes quickly metallic in conductivity. One view is that in the metallic regime the magnetic and electrical properties can be well explained by the holes residing in the spin-split host valence band, and in the insulating regime the holes occupy a separate impurity band, with the ferromagnetism mediated by hopping within this band [51]. However, others have described both regimes using an impurity band model [22, 23], and yet others have refuted the magnetic nature of the valence band entirely [52]. The electronic structure of (Ga,Mn)As has been studied extensively using magnetic circular dichroism techniques, but many of these studies were at the optical or infra-red wavelengths where the interpretation is complex owing to the complex nature of the excited transitions. Freeman *et al* [53] used hard x-rays at the As K edge to study directly orbital polarisation of (Ga,Mn)As, and showed there to be a substantial As $4p$ polarisation. Since the mediating holes in (Ga,Mn)As are thought to posses an As $4p$ character and XMCD measurements at the K edge are significantly simpler to interpret, owing to the absence of orbital moment in the initial state and the increased screening of the core hole, XMCD measurements at the K edge have the potential to provide direct information about the precise character of the mediating holes. Chapter 5 builds upon previous work by Freeman *et al* [53] to shed light on the nature of the mediating carriers.

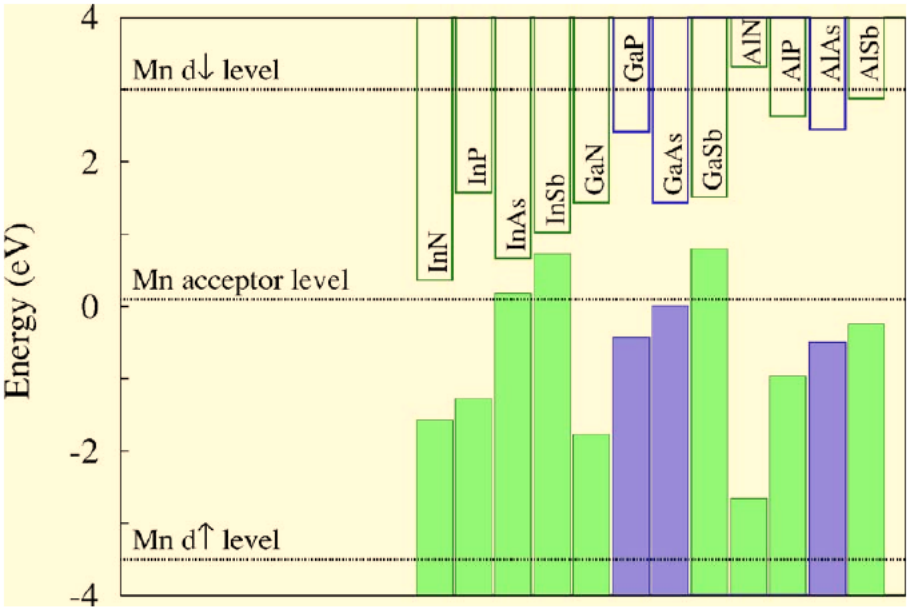

Figure 1.4 – Valence band and conduction band offsets for the family of III-V semiconductors. Mn derived energy levels are constant in this diagram according to the empirical internal reference rule [47]. Figure reproduced from Masek *et al* [46].

1.7 How this thesis is organised

This thesis study is organised into 6 Chapters including this Introduction:

In Chapter 2 the equipment and facilities used in this study are described, as well as their basic operation. The data processing techniques, the underlying physics behind them, and their application are also introduced.

In Chapter 3 Fe/(Ga,Mn)As heterostructures are examined using XMCD at the Fe and Mn $L_{3,2}$ absorption edges with two differing decay products to provide detailed layer and element specific information on the magnetism, and coupling of the layers. The different probing depths are analysed and used to interpret the results, which are also compared to previous bulk magnetometry measurements.

In Chapter 4 XMCD over the Mn $L_{3,2}$ absorption edge is used to analyse the total magnetic moment and strain in a set of (Ga,Mn)(As,P) samples with differing P doping. The strain response seen in the XMCD spectra is compared to the strain measured using high resolution XRD. and found to scale linearly. SQUID magnetometry is used to measure the evolution of the anisotropy from in-plane to perpendicular-to-plane with increasing P doping.

In Chapter 5 a series of (III,Mn)As samples are characterised using bulk magnetometry and transport. XMCD at the Mn and As K edge is then used to reveal information about the character of the states near the Fermi level which participate in the magnetic ordering. This information is related to the current models of ferromagnetism in (III,Mn)As compounds.

Chapter 6 provides a summary of the major results and their relevance, as well as suggesting ideas for future investigations where appropriate.

Chapter 2

Experimental techniques and data processing

2.1 Introduction

The bulk of the research presented in this study is obtained from x-ray absorption (XA) based techniques, in particular x-ray absorption spectroscopy (XAS) and x-ray magnetic circular dichroism (XMCD). These techniques require x-rays with specific and tunable properties, and hence were conducted at specialised facilities for the production of such x-rays: synchrotrons. Synchrotrons provide x-rays with high intensity, selectable polarisation, time structure and tunable wavelength. The high degree of polarisation of the beam allows for the exploration of weakly interacting and/or purely magnetic phenomena, such as the dilute magnetic Mn examined in this thesis.
The remaining characterisation was shared between x-ray diffractometry (XRD), resistance measurements using a cryostat system with variable magnetic field, and superconducting quantum interference device magnetometry (SQUID).

2.2 Synchrotron operation and beamlines

A synchrotron is an intense x-ray source in the form of a cyclic particle accelerator. They provide radiation with high intensity and spectral brilliance which is naturally collimated. The wavelength is tunable over a large range, and the radiation has an inherent time structure which can be exploited for time resolved experiments. It is comprised of straight sections joined by curved sections containing

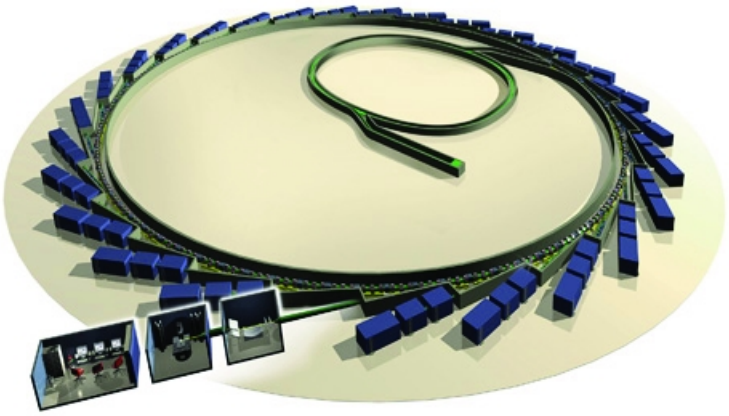

Figure 2.1 – Schematic diagram of Diamond Light Source (DLS) showing the LINAC and booster ring inside the main storage ring, and beamlines coming off this tangentially with an expanded view of a beamline at the forefront. Reproduced from *www.diamond.ac.uk*

variable strength magnets, called bending magnets, giving it the form of a round cornered polygon. The main beam or storage ring is initially fed by a smaller synchrotron, called the booster ring, and this in turn is fed by a linear accelerator(LINAC). The electrons are initiated in a high voltage power supply. Once in the storage ring the electrons are circulated through a thin beam pipe, evacuated to ultra high vacuum(UHV) pressures, using variable power bending magnets to sustain their orbit and radio frequency cavities to maintain their speed and bunch structure. A typical layout for a synchrotron, in this case Diamond Light Source (DLS), is shown schematically in Figure 2.1.

2.2.1 Producing synchrotron light

Photons are produced whenever the electrons accelerate, and at the relativistic speeds found at synchrotrons it is termed synchrotron radiation. Acceleration occurs necessarily in the bending magnet sections, where the Lorentz force is used to preserve the orbit, and also in insertion devices which deliberately perturb the electrons with the specific purpose of producing useful radiation. The relativistic effects of Lorentz contraction and the Doppler effect combine to shorten the wavelength of the emitted radiation in the lab frame of reference. The Lorentz contraction also has a pronounced effect on the angular spread of the emitted radiation.

The path of the electrons in a bending magnet is circular, caused by the Lorentz force, with the acceleration towards the centre of the orbit. The radiation emitted by an accelerating charge at non-relativistic speeds, such as electrons in radio antenna, has the familiar intensity shape of a dipole radiator, as shown in Fig-

ure 2.2(a) This is also true for relativistic electrons in their own frame of reference

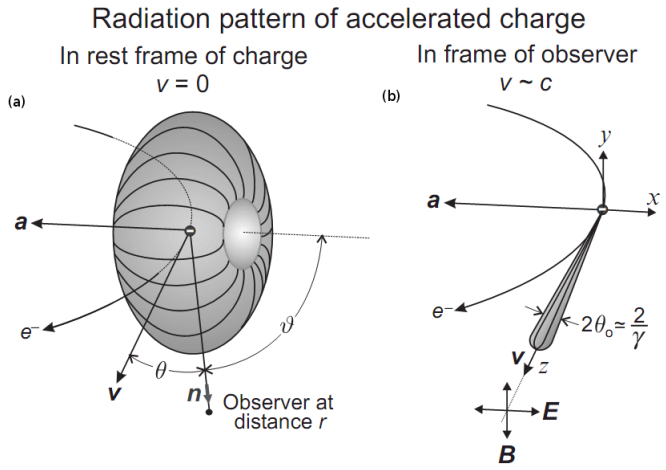

Figure 2.2 – Emitted radiation from electrons in there own reference frame and that of the observer. Reproduced from J. Stöhr's book on Magnetism [32]

, but from the lab frame of reference it is necessary to apply the Lorentz transformation to obtain the angle of emission. It is helpful to define the parameter

$$\gamma = \frac{1}{\sqrt{1 - \frac{u^2}{c^2}}}$$

i.e. the ratio between total energy of the electron and the rest mass energy. Photons emitted at large angles with respect to the direction of motion of the electrons in their frame of reference have a large parallel velocity in the lab frame of reference because of the invariance of c. This effect results in the radiation being bent forward into a narrow cone shape where the angular spread is given by $1/\gamma$, in the case of bending magnets, as shown in Figure 2.2(b). It is worth noting that the electron rest-mass is $\sim\ 0.5\,MeV$ while typical values of the electron energy while in the storage ring is of the order of $1 - 5\,GeV$, which leads to values of γ from 2000 to 10000, resulting in an angular spread of less than 1 mrad.

Insertion devices

A major source of x-rays at synchrotrons are insertion devices, called wigglers and undulators which are installed in straight sections of the storage ring. Schematic drawings of bending magnet sections and simple insertion devices are shown in Figure 2.3 and their angular spread and emitted spectrum is depicted in Figure 2.4. Both wigglers and undulators are comprised of similar dipole magnet arrays, but provide radiation with differing properties that are distinguished by

the dimensionless parameter:

$$K = \frac{eB\lambda_p}{2\pi\beta m_e c} \tag{2.1}$$

where $\beta = v/c$, m_e is the electron mass, B is the magnetic field strength and λ_p is its periodicity. K characterises the electron motion such that for $K \leq 1$ the electron displacement is small and the radiation emitted is coherent, and the device is called an undulator. Whereas for $K \gg 1$ the displacement becomes large, there is no longer coherence and the device is known as a wiggler. Wigglers produce

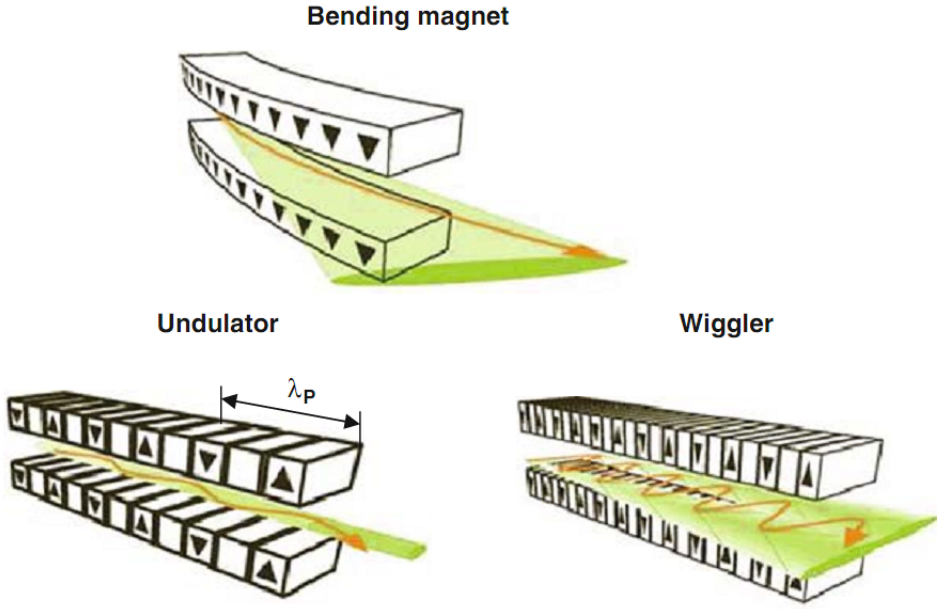

Figure 2.3 – Schematic representation of a bending magnet and the two types of insertion devices in their simplest form. Reproduced from the book *Applications of Synchrotron Radiation* [54]

a broad spectrum of emitted radiation with spectral shape similar to that of a bending magnet (Figure 2.4). Potentially the photon flux is higher than that of a bending magnet, and scales as $2N$, where N is the number of dipole magnets in the array. Typically they are used for higher energy applications as they are able to provide higher energy photons.

Undulators produce partially coherent radiation and as a consequence they produce very narrow band radiation(and harmonics). They provide high spectral brightness, and with more complex arrangements of dipole magnets, such as the APPLE II undulator depicted in Figure 2.5 they are able to provide variable polarisation. Intensity is proportional to N^2. The APPLE II undulator uses four

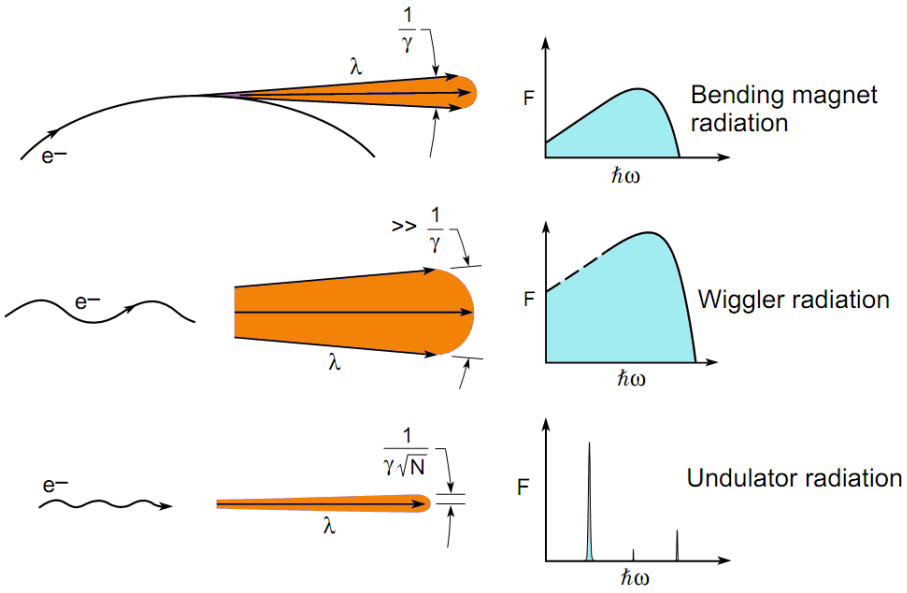

Figure 2.4 – The three types of insertion devices and the spectrum they produce, reproduced from a lecture series by D. Attwood.

individual arrays that can be moved separately allowing for the production of circularly polarised light by inducing a helical trajectory in the electron beam. Arbitrary polarisation can be achieved using undulators such as these. With the exception of beamline 6.3.1 at the Advanced Light Source, all the XAS and XMCD data in this study were taken using undulator beamlines.

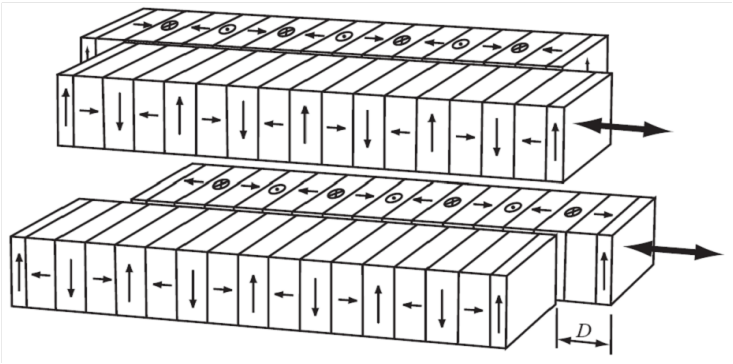

Figure 2.5 – Schematic diagram of the APPLE II undulator where four Halback arrays of permanent magnets are used to produce various polarisations of the x-ray beam.

2.2.2 Beamlines

Beamlines are used to transport the photons generated by bending magnets, wigglers or undulators to the experimental set-up or endstation. They comprise an evacuated pipe coming tangentially off the storage ring and conditioning optics.

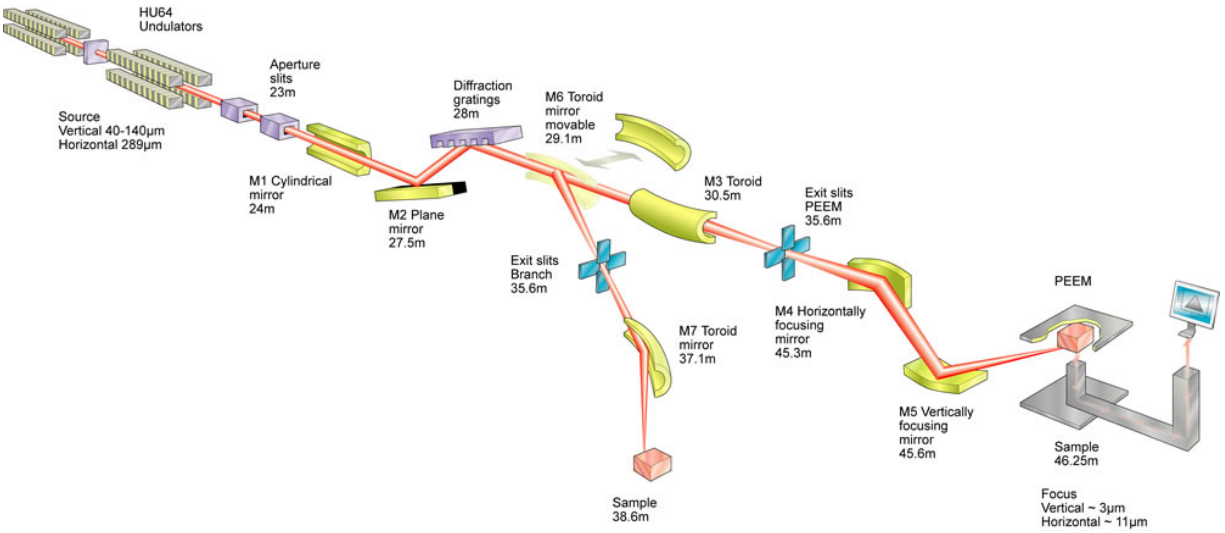

Figure 2.6 – A schematic of the I06 beamline at Diamond Light Source. Taken from their website at www.diamond.ac.uk

A major function of the beamline optics is to select the desired slice of the emitted spectrum for the experiment. This is done via a monochromator, the type of which depends mostly on energy range being used i.e. when the energy is such that the wavelength is comparable to inter-atomic distances then crystals are more convenient than man-made structures. For high energy applications such as measuring the K absorption edges a monochromator based on crystal diffraction is used whereas for soft x-ray studies a diffraction grating is used. For the crystal monochromator constructive interference only occurs when the Bragg condition is fulfilled:

$$2d \sin\theta = n\lambda$$

where n is the harmonic order, θ is the angle of incidence and λ is the wavelength. Since θ is wavelength dependent varying it acts as a monochromator. Typically a two-crystal set-up is used which relies on two simultaneous Bragg diffractions and helps to improve the spectral resolution. Diffraction gratings consist of equally spaced diffracting structures and function in the same way. The diffraction condition becomes:

$$d(\sin\theta_i + \sin\theta_d) = n\lambda$$

where θ_i and θ_d are the incident and diffracted beam angles respectively.

End-stations

The end-station is made up of the sample cryostat or chamber and instrumentation. The samples were typically mounted onto a long sample rod which is fitted into the cryostat. The sample rod contains a number of electrical contacts for the measurement of current, temperature and often the application of current for heating e.g. via a Kapton coil. Source meters are used for the measurement of the XA induced drain current. Additional instrumentation often included a photodiode for the measurement of fluorescent yield. For the soft x-ray measurements the cryostat was typically pumped down to UHV conditions which entails the presence of backing pumps, turbo pumps and ion pumps. The sample rod itself is mounted on a manipulator which can allow for rotation around the vertical and translation along all principal axis. Often the manipulator is automated.

Detection methods

For the measurement of XA several techniques can be used. The most reliable and easily interpreted method is that of total electron yield (TEY), where a nanoammeter is used to measure the drain current from the sample to replace the ejected photoelectrons. Fluorescent yield (FY) uses a photodiode to measure the emitted photons from recombination of the photoelectron and core hole. Two methods used less often are transmission and reflection.

At some stage up-beam from the sample it is standard practice to have some form of mesh present in the beam which measures the intensity of the incoming beam, usually called the I_0. Dividing by the I_0 allows for the correction of fluctuations in the beam intensity. For the measurement of drain current it is necessary to make sure that the sample layer is adequately grounded and sufficiently conducting to prevent the build up of charge, which interferes with the emitted secondary electrons. The choice of detection techniques is mainly dependent on the sample. For transmission detection it is necessary to have a a sample which is thin enough to allow a significant amount of x-rays through. For hard x-rays this can be achieved by etching away or thinning the substrate, however this presents technical challenges, and requires a sample layer thickness of the order of a micron which is not always possible. TEY measurements are limited to the near-surface region, owing to the short electron escape depth, typically a few nanometres. Fluorescence measurements have a greater probing depth, ranging from $\sim 100\,\mathrm{nm}$ to $\sim 10\mu\mathrm{m}$ depending on the x-ray energy and sample composition, but signal is a

less reliable indicator of absorption as it suffers from more secondary effects such as self absorption.

2.2.3 The Advanced Light Source(ALS), Berkeley

Beamline 4.0.2 at the ALS is supplied by an APPLE-II 5.0-cm period elliptical polarization undulator (EPU5) [55]. It is capable of supplying 98% circularly polarised light as well as linearly polarised. The wavelength is selectable in the range 100-2000 eV. The eight-pole magnet endstation was used, which is capable of applying a field of up to 0.9 T along any vector. The available detectors are either total electron yield or a fluorescent yield photodiode. Transmission is also possible but was not used. Typical vacuum pressure used was of the order of 10^{-9} Torr and the sample temperature was typically kept at $\sim 15\,K$

Beamline I06 at Diamond Light Source, Oxford

This beamline is also supplied by APPLE-II undulators. The wavelengths range depends slightly on the type of polarisation desired but in general $\sim 100\,eV$ to >1 keV are possible. The schematic for I06 is shown in 2.6, the branchline was used together with the superconducting magnet endstation. Fields of up to 5 T can be applied to the sample. The measurement techniques available are total electron yield and fluorescent yield.

Beamline ID12, The European Synchrotron Radiation Facility, Grenoble

This is a hard x-ray beamline serviced by three undulators which provide high flux throughout the large energy range possible ($\sim 2 - 20$ keV). The energy range used for our experiments was again supplied by an APPLE-II undulator. The magnet field is generated by a 7 T superconducting magnet. Both circularly polarised and linearly polarised light are possible.

2.3 Other experimental equipment used

2.3.1 X-ray diffraction

The characterisation regarding strain and relative elemental concentrations were performed using a Philips X'Pert Material Research Diffractometer (MRD). This system comprises a Cu K_α source, various beam conditioning devices, a sample holder in the form of an open Eulerian cradle and two detectors. The set-up used most frequently in this study is shown schematically in Figure 2.7. The x-ray source is a high voltage Cu K_α generator held at 40 kV and 55 mA. Immediately after the source a half degree slit is used to limit divergence. The beam is then incident on a parabolic x-ray mirror collimator which corrects for remaining divergence, and then passed through Soller slits which reduce axial divergence. A Bartels symmetric Ge(2 2 0) 4 crystal monochromator is used to obtain a beam with small wavelength spread (which also removes Cu $K_{\alpha 2}$) and a very small well defined divergence. The monochromator works by using the Bragg condition at each reflection (for the Cu $K_{\alpha 1}$ wavelength) for a specific input angle. X-rays with a slightly different wavelength maybe reflected by the first two crystals when incident at a slightly different angle, but because the second set of crystals are reversed they will no longer satisfy the Bragg condition and hence will not be reflected [56].

The sample is mounted on an open Eularian cradle which provides x, y and z movement along with three rotational degree of freedom as shown in Figure 2.8. This allows for alignment of any layer orientation, particularly important when dealing with very high resolution detectors such as the triple axis detector or when the sample layer is tilted with respect to the substrate. Two possible beam paths are available for selection after diffraction from the sample. The first is directly into an open detector which has relatively poor resolution due to the high angle of acceptance, which also leads to a higher background count from diffuse scattering. It is possible to limit both these problems by using slits immediately before the detector. The second is via a crystal analyser, which is a channel cut Ge crystal. The diffracted x-rays go through 3 (0 0 2) reflections before entering the detector. This provides very high resolution by restricting the acceptance angle to 12 arc seconds. There is also a consequent drop in intensity.

The open detector was used mainly for alignment before proceeding to the crystal analyser, but was also used where resolution was not imperative as the

higher throughput enables quicker measurements.For example it is useful for locating peaks when the exact coordinates are not known. The higher angle of acceptance allows for sampling of a greater region of k space, which make locating peaks easier. It is also very useful where the crystal exhibits mosaic spread or gradual change in lattice parameter (e.g. through relaxation) as the wider acceptance angle can be exploited to obtain a stronger signal. For samples of high crystal quality and for separation of peaks which are close in k space the higher resolution of the crystal analyser becomes vital.

The x-ray diffractometer was used for two separate purposes which required two different configurations. For characterisation of the lattice parameters and relative concentrations the configuration shown schematically in Figure 2.7 was used. The two most commonly used diffraction scans in this study were so called $2\theta\omega$ scans (sometimes simply called line scans) and $\omega 2\theta\omega$ reciprocal space maps (RSM). The $2\theta\omega$ scan comprises a continuous specular scan. Since the source position is fixed this is achieved by varying the detector position and the sample tilt along the beam direction (ω) so that the angle of the incoming and diffracted beam are identical with respect to the starting sample alignment (the angle between the detector and the source is called 2θ and the sample tilt along the beam direction is called ω, hence the name $2\theta\omega$ scan). Any Bragg diffractions found during these scans reveal information about the plane spacing for a given sample orientation. An example of a typical $2\theta\omega$ scan is shown in Figure 2.9. The information that can be extracted easily from this type of scan is the out-of-plane lattice parameters of the visible peaks, in this case the sample layer and substrate, either by using either Bragg's law directly or more accurately the Panalytical Epitaxy software. Panalytical Epitaxy can be used to fit the data by entering the composition and structure of each of the layers. By either manual or automated fitting the parameters can be fine tuned to reveal layer thickness and elemental concentration. Since the software uses Vegard's Law to determine the effect on the lattice parameter of doping, the concentrations revealed by fitting can be used in conjunction with Vegard's law to reveal the lattice parameters of layers in cases where Bragg's law cannot by applied directly (for instance where the sample layer is buried under the substrate layer).
$\omega 2\theta\omega$ RSM are built up from a series of $2\theta\omega$ scans each with a slightly different ω value. A symmetric RSM, such as the (0 0 4), provides information about tilt and mosaicity. Whereas asymmetric RSM's, such as the (4 4 4) shown in Figure 5.2, provide information on the strain and degree of relaxation. In this example both the sample layer peak and the substrate layer peak lie on a line of constant q_x in-

dicating that the layer and substrate in-plane lattice parameters match, meaning the layer is fully strained.

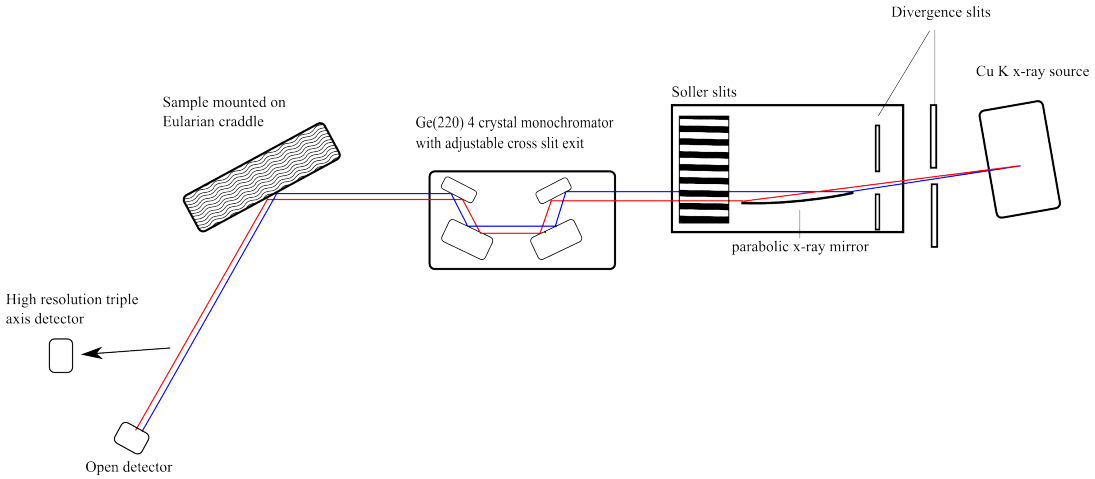

Figure 2.7 – Schematic diagram of the X'pert MRD in the configuration used for diffraction characterisation.

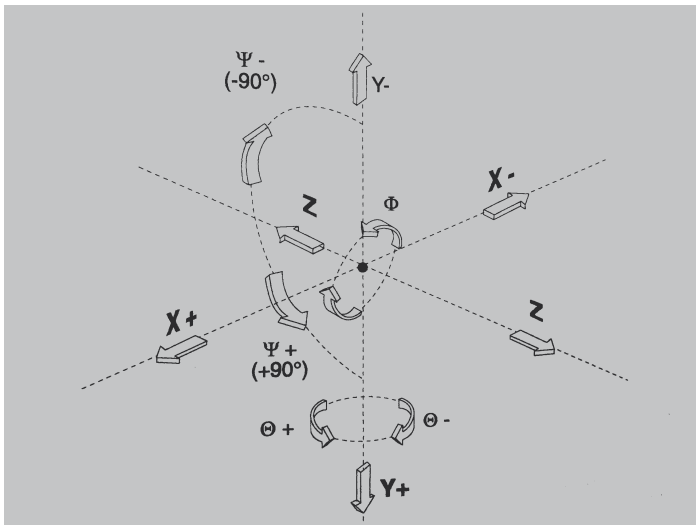

Figure 2.8 – The operation of the Eularian craddle where the incident beam is along the x direction.

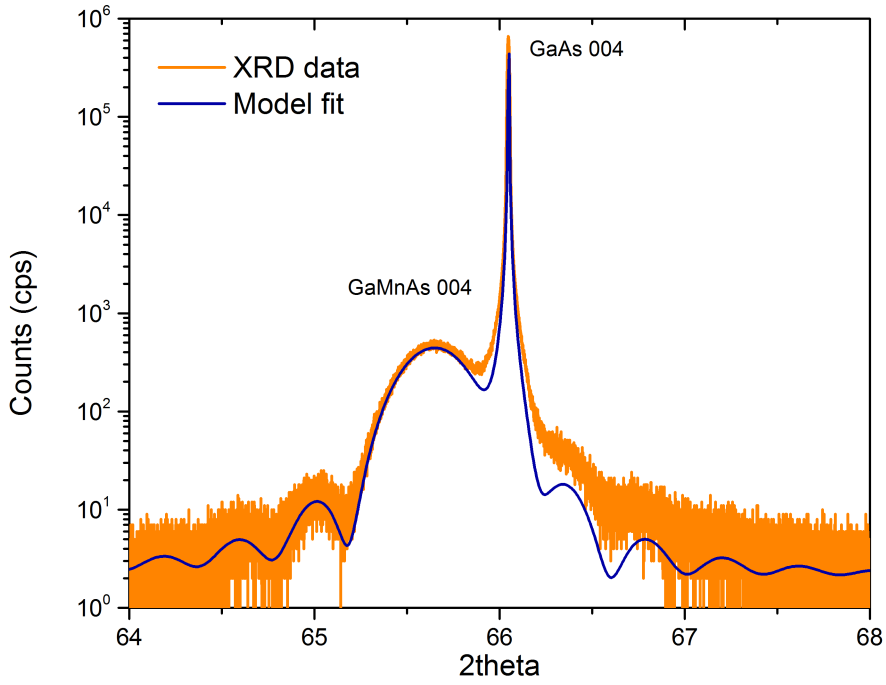

Figure 2.9 – Typical $2\theta\omega$ scan of a 25 nm (Ga,Mn)As layer grown on GaAs$(0\,0\,1)$. The scan is centred around the bright GaAs$(0\,0\,4)$, but the broad (Ga,Mn)As $(0\,0\,4)$ is clearly visible to the left of the substrate peak. A model created using Panalytical Epitaxy software is also shown.

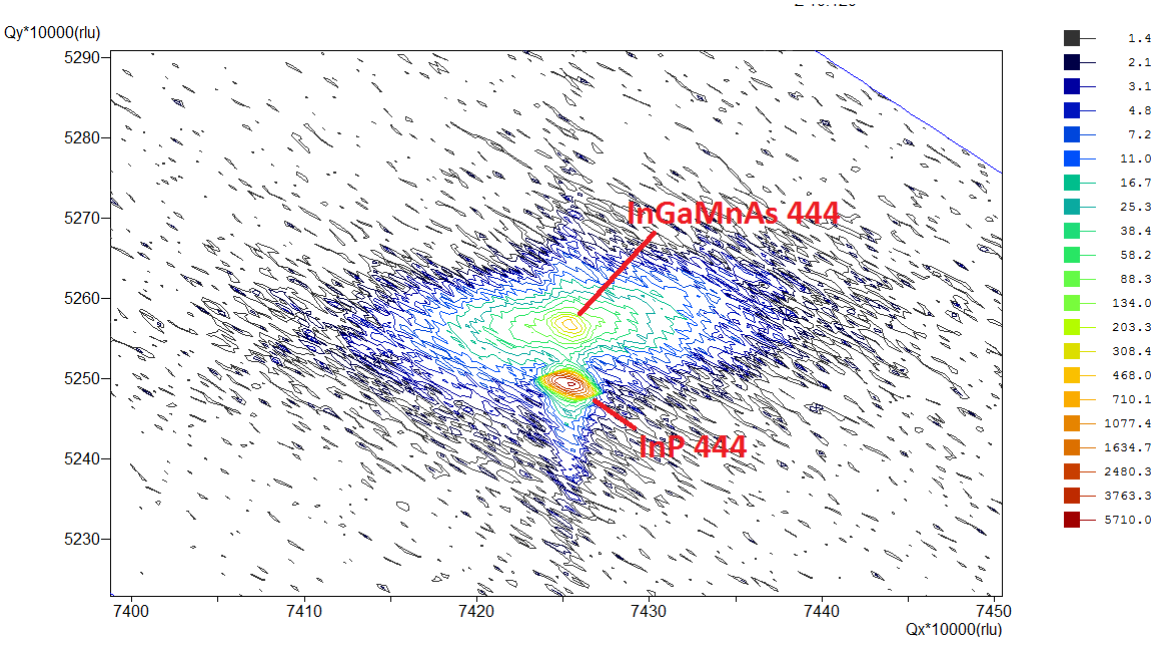

Figure 2.10 – Asymmetric RSM centred around the substrate 444 of an InGaMnAs layer grown on InP$(0\,0\,1)$. Both peaks have the same value of q_x indicating a fully strained layer.

2.3.2 SQUID magnetometer

Superconducting quantum interference devices (SQUIDs) make use of the wave coherence of Cooper pairs in a superconductor, and combine this with two Josephson

junctions to detect minute magnetic fields. The central element is a ring of superconducting material with a Josephson junction on each side which has two current paths that have long wavelengths, and nominally no phase difference between them at zero flux. Any magnetic field perpendicular to the plane of the ring can create a phase difference between the two paths. The flux through a superconducting loop is quantized in units of $\Phi = \frac{h}{2e}$. The Josephson junctions in the ring introduce the same phase change when the flux is integer multiples of Φ and opposite phase changes when the flux is half integer multiples of Φ, leading to constructive or destructive interference respectively. This causes the critical current density to vary periodically with respect to flux. It is the high sensitivity to changes in flux that allows for such precise measurement of very small magnetic moments. The sample is moved through a set of wound superconducting coils which are inductively coupled to the SQUID ring. The voltage modulation across the junction is used determine the magnetic moment of the sample. The SQUID system used for this study was a Quantum Design Magnetic Property Measurement System (MPMS). The SQUID was primarily used to determine the T_C, saturation magnetisation and magnetic anisotropy of the samples studied in this thesis. In order to determine the T_C the sample was cooled with an applied field, typically of the order of 1000 Oe(field cool), and then warmed with no applied field (remnance curve). The applied field during cooling encourages single domain behaviour and the remnance measurement allows for the determination of the Curie temperature more accurately (as the point at which Ferromagnetic behaviour ceases). If one relies entirely on measurement with a small applied field this has the affect of shifting the T_C to higher values. The magnetic anisotropy can be characterised by performing hysteresis loops along the various crystallographic direction.
The saturation magnetisation can also be determined by a suitably high field hysteresis loop. This is usually performed along the easy axis of the sample and involves the removal of the diamagnetic background which should be a linear offset from the final loop. To make this easier it is important to have wide enough scan so that the saturation point can be clearly determined. For a single domain sample the saturation moment can also be determined by examining the remnant magnetisation along several orthogonal axis and calculating the resultant magnetisation.

2.3.3 Transport measurements

Transport measurements were performed using a Helium cooled cryostat with adjustable magnetic field. The sample were either patterned into Hall bars and

attached to a header board with contacts wedge bonded using aluminium wire, or scribed into squares and measured in Van der Pauw symmetry with contacts made using silver paint. Four point measurements were taken using EG&G AC lock-in amplifiers.

2.4 X-ray absorption spectroscopy(XAS)

The majority of the data presented in this study is obtained from x-ray absorption spectroscopy(XAS) and in particular x-ray magnetic circular dichroism (XMCD). X-ray absorption is an intrinsically quantum mechanical process which relies on the photoelectric effect, in which an incident x-ray photon liberates an electron from a low energy bound state. The fundamental physical quantity that is probed, either directly or indirectly, is the x-ray absorption coefficient ($\mu(E)$). The x-ray absorption coefficient generally decreases as approximately $1/E^3$ except at specific energies where there are sudden sharp increases in the absorption. These are called absorption edges and correspond to the energies required to liberate low energy bound electrons to empty states just above the Fermi energy. These energies are unique to the absorbing element and make XAS an inherently element specific technique. In a single electron picture of the absorption event the absorption edge appears as a sudden peak, or step, in the absorption coefficient the size of which is primarily dictated by the occupancy of the core and valence states, and the energy dependence reflective of the density of empty states. However for most transitions this picture is complicated by other interactions such as the crystal field, multiplet effects and polarisation dependent absorption which are largely responsible for the detailed fine structure of XA spectra. The excited ions then decay by one of two methods: (i) Auger decay where an intermediate electron drops into the hole and the liberated energy results in the ejection of another electron, termed an Auger electron; (ii) Fluorescent decay, where the photoelectron generated by the absorption event recombines with the hole left behind re-emitting an x-ray photon. Generally XA spectra are divided into two regions: the near-edge region which comprises the spectrum immediately before and after the absorption edge(x-ray absorption near-edge structure(XANES)), and the extended x-ray absorption fine structure(EXAFS) which typically extends to approximately 1 keV after the absorption edge (see Figure 2.11). The XANES is determined by the density of states, electron correlation, or multiple scattering and largely provides information about the absorbing atom. The EXAFS is dominated by scattering events of the photoelectron and mainly reveals information about the local atomic surroundings of the absorbing atom.

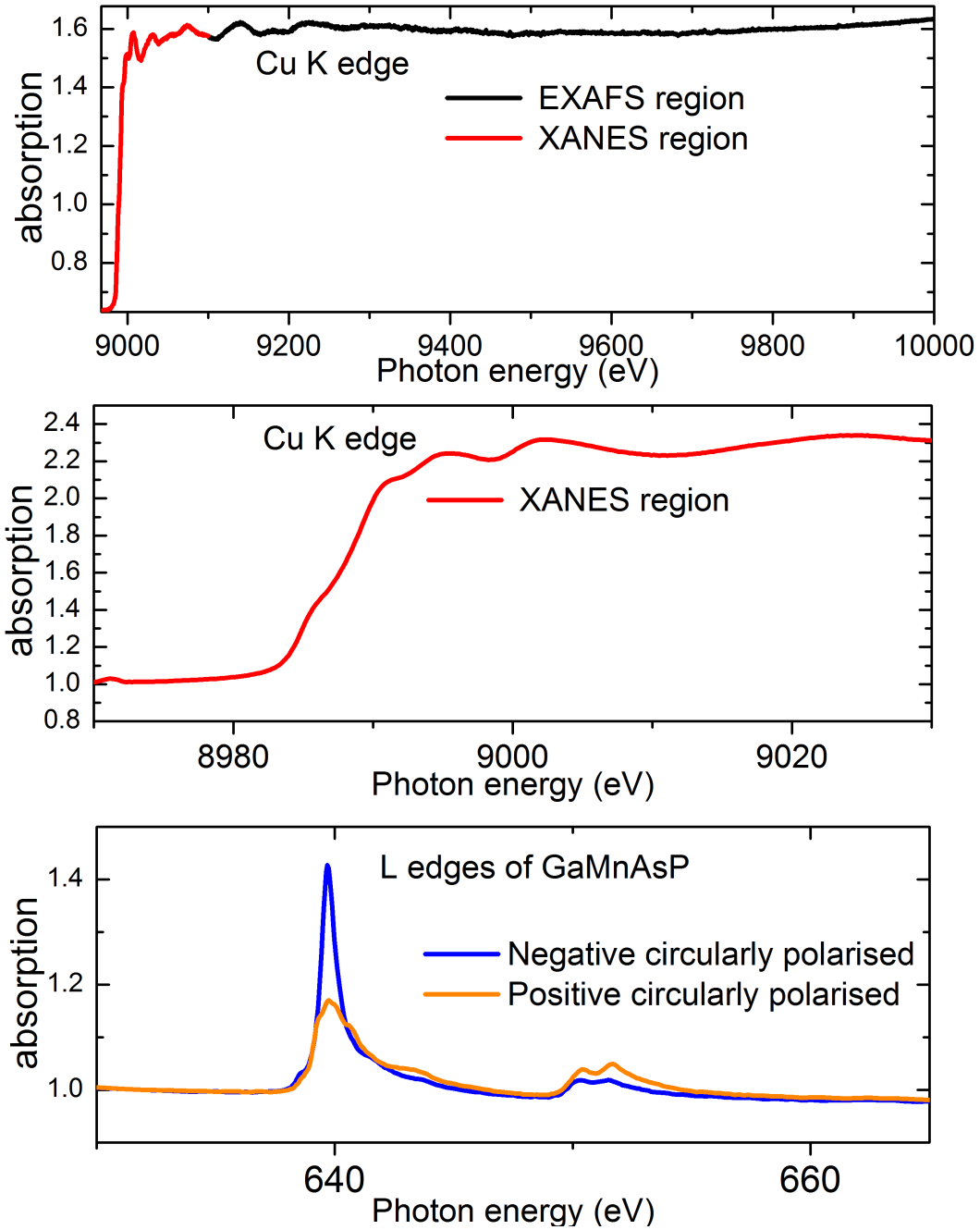

Figure 2.11 – (top panel) XA spectrum for the Cu K absorption edge with approximate XANES and EXAFS ranges indicated. (centre panel) The XANES region of the Cu K absorption edge. (bottom panel) The polarisation dependent Mn $L_{3,2}$ absorption edges for a (Ga,Mn)(As,P) sample.

2.4.1 X-ray magnetic circular dichroism(XMCD)

XMCD relies on the difference in XA spectra obtained using right and left-handed circularly polarised light. XMCD is a well established and powerful technique which utilises the dependence of attenuation coefficients on the relative orienta-

tions of the photon helicity and sample magnetization, in ferromagnetic materials, to reveal separate spin and orbital information about the absorbing atom. This combined with the inherent element specificity of XA absorption make XMCD a uniquely revealing probe of the micromagnetic properties of solids. The first theoretical prediction of XMCD was given by Erskine and Stern [57], who predicted XMCD in the $M_{2,3}$ edges of ferromagnetic Ni. However experimental evidence of XMCD was not forthcoming until Schütz et al [58] reported small but non-negligible XMCD at the Fe K edge using iron foil. Interest in the area expanded rapidly after Chen et al [59] demonstrated very large XMCD in the soft x-ray range at the L edges of Ni. XMCD matured more fully as an experimental tool following theoretical work by Thole et al [60] and Carra et al [61], who used a single ion model to derive a set of magneto-optical sum rules which relate the integrated intensities to the separate spin and orbital moments of the absorbing ions. This was applied to the Fe and Ni L edges by Chen et al [62], and compared favourably to other techniques and theory.

The physical origin of XMCD lies with the conservation of the angular momentum carried by the photon and with spin-orbit interaction. It is most easily understood as a two-step process, although this separation is artificial [58]. The first step involves the absorption of a circularly polarised photon and subsequent excitation of a core electron. The photon carries an angular momentum of $\pm\hbar$ in the direction of propagation, the sign of which is dependent on helicity. This momentum is necessarily transferred entirely to the photoelectron. If the core level is spin-orbit split the momentum may be transferred to both spin and orbital moment of the photoelectron via the Fano effect [63], otherwise it is transferred entirely to the orbital moment. In the second part of the process the XA spectra represents the empty density of states with allowed symmetry. This process is shown diagrammatically in Figure 2.12.

The allowed transitions of the absorbing electron are governed by selection rules which stem from symmetry considerations of the initial and final quantum states. In the dipole approximation for circularly polarised light only transitions where $\Delta l = \pm 1$ and $\Delta m = \pm 1$ and $\Delta m_s = 0$ are allowed, where s is the spin quantum number, l is the orbital angular momentum quantum number, and m is its projection along the polarisation axis. As such XMCD spectra reflect any difference in the occupation of allowed states from both an orbital and spin perspective (except when the core state is an s electron where only orbital differences are seen). In a simplified one-electron atomic model, where one spin-band is filled

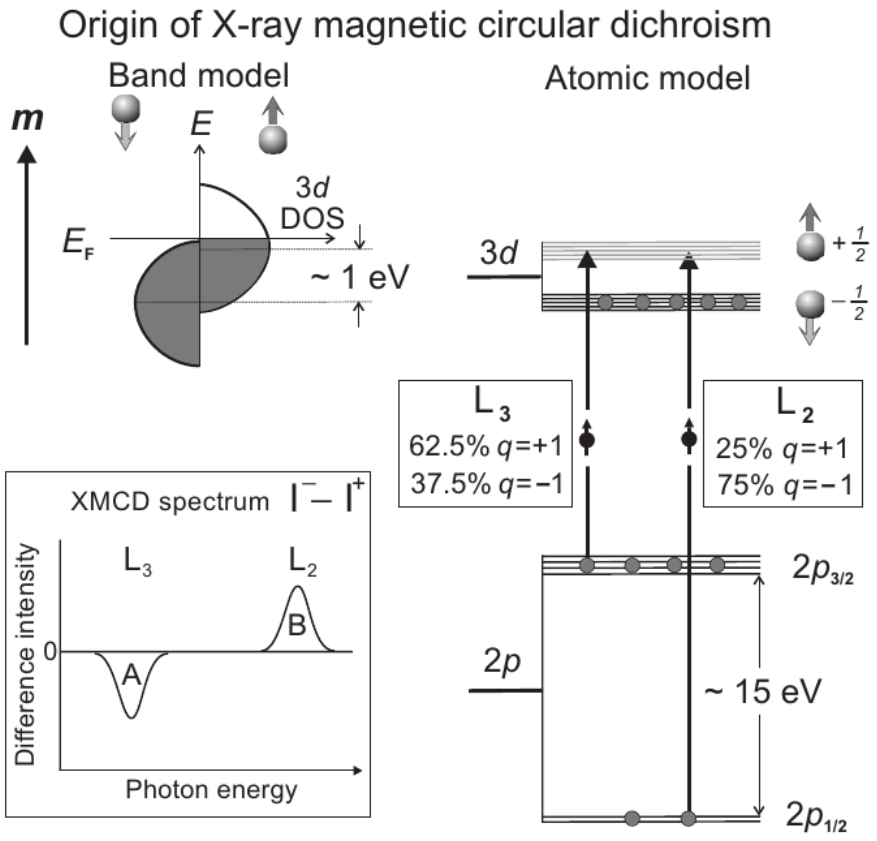

Figure 2.12 – A one-hole atomic and band model picture of L-edge x-ray absorption of circularly polarised photons, with angular momentum $q = \pm 1\hbar$. In the atomic model one spin channel is entirely filled, as is the case for Mn^{2+}. Adapted from the book *Magnetism* [32]

and the weak spin-orbit coupling in the d-band is ignored, then the origin of the XMCD effect can be seen by considering the angular part of the squared dipole transition matrix element from the $p_{3/2}$ and $p_{1/2}$ states to the empty d-band states. These intensities can be calculated by using the dipole transition operator on the spin-orbit and exchange split p core states to spin-up exchange split d valence orbitals , as calculated in Ref. [32]. These are listed in Figure 2.13, and can be used to obtain the XMCD effect.

This type of simplified one-electron model works moderately well for the K edges of transition metals, where the core hole in the $1s$ level is well screened from the valence states. This means that the absorption spectra closely follow the empty density of states with allowed symmetry. This also provides reasonable agreement with the XMCD intensities when integrated over energy. However, it fails to describe the fine structure in the TM L edge absorption spectra. In the case of localised $3d$ states other effects become significant including: multiplet and charge transfer effects. Such effects require atomic multiplet theory, such as that employed in the CTM4XAS software [64] in order to accurately reproduce the

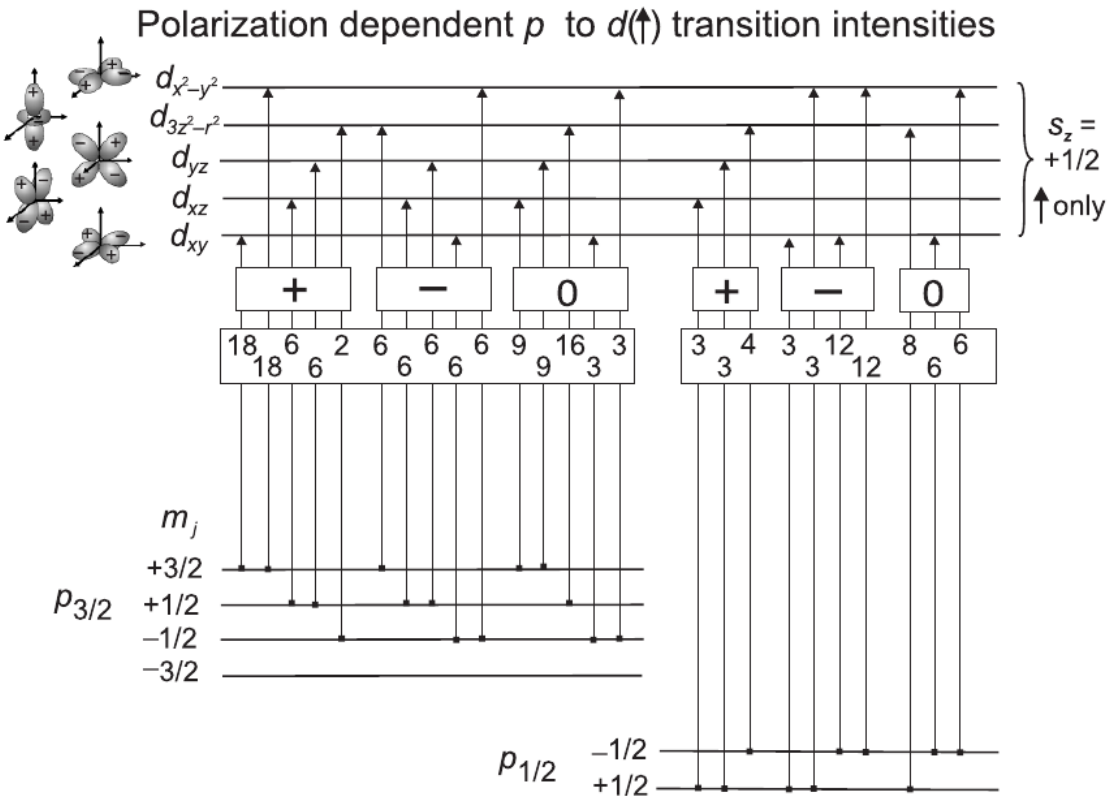

Figure 2.13 – Transition probabilities calculated using the dipole transition operator on the one-electron model from spin-orbit and exchange split p core states to spin-up exchange split d valence orbitals. The listed intensities are proportional to the transition probabilities. Adapted from the book *Magnetism* [32].

absorption spectra and XMCD (see Figure 2.14.

In crystalline solids the formation of bonds modifies the density of states in the valence band. This modification in turn affects the absorption structure over the absorption edge as compared to an atomic model and can lead to a dependence of the shape of the XA and XMCD spectra on the direction of the x-ray polarisation with respect to the crystal axes [65]. The effect can often be well simulated by considering a crystal field with appropriate symmetry.

2.4.2 The magneto-optical sum rules

The XMCD sum rules can be used to separately determine the orbital [60] and spin [61] components of the magnetic moment of the absorbing atom. Their applicability has been demonstrated in many subsequent studies, for example [62,66,67].

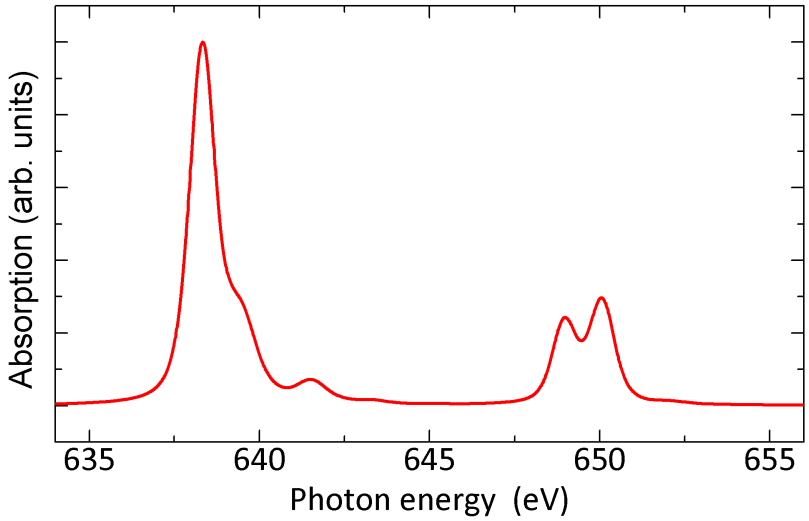

Figure 2.14 – An atomic multiplet model of Mn^{2+} XAS, produced using the CTM4XAS software [64]

The orbital component

Thole et al [60] showed that the orbital moment $\langle L_z \rangle$ can be calculated from the quantity ρ:

$$\begin{aligned} \rho &\equiv \frac{\int_{J_+ + J_-} (I_+ - I_-)\, dw}{\int_{J_+ + J_-} (I_+ + I_- + I_0)\, dw} \\ &= \frac{1}{2} \frac{c(c+1) - l(l+1) - 2}{l(l+1)(4l + 2 - n)} \langle L_z \rangle \end{aligned} \tag{2.2}$$

Where l and c are the valence and core orbital quantum numbers respectively, I_+ and I_- are the integrated intensities for positive and negative circularly polarised light respectively and I_0 is for linearly light. n is the occupation number of the valence shell. Defining the integrals the same way as Chen et al [62]:

$$p = \int_{j_+} (I_+ - I_-) \tag{2.3}$$

$$q = \int_{j_+ + j_-} (I_+ - I_-) \tag{2.4}$$

$$r = \int_{j_+ + j_-} (I_+ + I_-) \tag{2.5}$$

assuming:

$$I_0 = \frac{(I_+ + I_-)}{2}$$

and substituting into Equation 2.2 gives:

$$\rho = \frac{2}{3}\frac{q}{r} \tag{2.6}$$

The spin component

The spin component of the magnetic moment was derived by Carra et al [61] and shown to be related to the quantity δ:

$$\delta \equiv \frac{\int_{j_+}(\mu_+ - \mu_-)\,dw - [(c+1)/c]\int_{j_-}(\mu_+ - \mu_-)\,dw}{\int_{j_+ + j_-}(\mu_+ + \mu_- + \mu_0)} \tag{2.7}$$

$$= \frac{l(l+1) - 2 - c(c+1)}{3c(4l+2-n}\langle S_z\rangle + \frac{l(l+1)[l(l+1)+2c(c+1)+4] - 3(c-1)^2(c+2)^2}{6lc(l+1)(4l+2-n)}\langle T_z\rangle \tag{2.8}$$

The sum rules for the transition metal L edges

For the $2p \rightarrow 3d$ transitions of the $L_{3,2}$ edges where $c = 1$ and $l = 2$ the magneto-optical sum rules for spin and orbital moment, derived by Thole [60] and Carra [61], can be written as [62]:

$$m_{orb} = -\frac{4\int_{L_3+L_2}(\mu_+ - \mu_-)\,dw}{3\int_{L_3+L_2}(\mu_+ + \mu_-)\,dw}(10 - n_{3d}) \tag{2.9}$$

$$m_{spin} = -\frac{6\int_{L_3}(\mu_+ - \mu_-)\,dw - 4\int_{L_3+L_2}(\mu_+ - \mu_-)\,dw}{\int_{L_3+L_2}(\mu_+ + \mu_-)\,dw} \times (10 - n_{3d})\left(1 + \frac{7\langle T_z\rangle}{2\langle S_z\rangle}\right)^{-1} \tag{2.10}$$

In which the linearly polarised term has been replaced by the equivalent $(\mu_+ + \mu_-)/2$, and m_{orb} and m_{spin} denote the orbital and spin magnetic moments respectively in units of μ_B/atom. n_{3d} is the occupancy of the $3d$ states. The

magnetic dipole operator $\langle T_z \rangle$ is a measure of the anisotropy in spin distribution. For cubic structures it is close to zero and can be neglected for the cubic and near cubic structures examined in this thesis.

2.4.3 Application of the sum rules to the Mn L edges

The basic application of the sum rules used in this thesis to the Mn L edges follows the steps illustrated in Figure 2.15 and is much the same procedure as used originally by Chen et al [62]. Initially the spectra for μ_+ and μ_- were normalised to 1 at the pre-edge region. The sum of μ_+ and μ_- was then taken and a background subtracted from it. The removal of the background was done as simply as possible using a linear subtraction where effective and in other cases a polynomial function fitted to the relatively featureless areas above and below the $L_{3,2}$ edges, so as to leave any details which are obscured by the edges themselves as unchanged as possible. The edge steps were removed using simple step functions positioned directly under the centre of the absorption edges. The height of the step functions used was 2/3 and 1/3 of the final background height for the L_3 and L_2 edges respectively (based on the degeneracy of the initial $2p$ levels). The integrated area is not sensitive to the form of the step function, so a simple square step was used. For low concentration of absorbing atoms, such as Mn in (Ga,Mn)As where the typical concentrations examined are $< 10\%$, the removal of the background and edge steps can be a source of considerable error, and thus needs to be carefully implemented. The background and step functions applied to typical Mn spectra are shown in Figure 2.15 (a) and (d) respectively. The XMCD was calculated as $\mu_+ - \mu_-$. It is sometimes necessary to subtract a small linear slope from the XMCD which is due to some small polarisation dependent variation in signal along the spectra.

For application of the sum rules to the Mn L edges further steps need to be taken. The separate determination of the spin and orbital moment requires the separate integration of the L_3 and L_2 edges which in principal is easily accomplished as they appear to be well separated, but in practice the Coulomb interaction between the $2p$ and $3d$ states leads to mixing of the $j = 3/2$ and $j = 1/2$ manifolds. A correction factor of 1.47 was derived by Edmonds et al [67] by comparing calculated spectra with their ground-state magnetic moments. This is applied to the calculated values of spin moment for the Mn L edges throughout this study.

Neglecting the magnetic dipole term and using the definitions:

$$p = \int_{L_3} (\mu_+ - \mu_-)\, dw$$
$$q = \int_{L_3+L_2} (\mu_+ - \mu_-)\, dw$$
$$r = \int_{L_3+L_2} (\mu_+ + \mu_-)\, dw$$

Equation 2.9 and Equation 2.10 can be rewritten as:

$$m_{orb} = \frac{-4q(10 - n_{3d})}{3r}$$
$$m_{spin} = \frac{-(6p - 4q)(10 - n_{3d})}{r}$$

Then if we call P the fractional polarisation of the photons and define $C_1 = n_{3d} \times P$ and $C_2 = n_{3d} \times P \times 1.47$:

$$m_{orb} = \frac{-4q}{3r} \times C_1 \tag{2.11}$$
$$m_{spin} = \frac{-(6p - 4q)}{r} \times C_2 \tag{2.12}$$

An additional quantity that can a useful indicator is given by the ratio of of the orbital to the spin moment. This quantity is particularly useful when experimental factors make the removal of the background difficult since it relies only on the difference of the spectra. This ratio is given by:

$$\frac{m_{orb}}{m_{spin}} = \frac{\left(\frac{-4q(10-n_{3d})}{3r}\right)}{\left(\frac{-(6p-4q)(10-n_{3d})}{r}\right)} = \frac{2q}{9p - 6q} \tag{2.13}$$

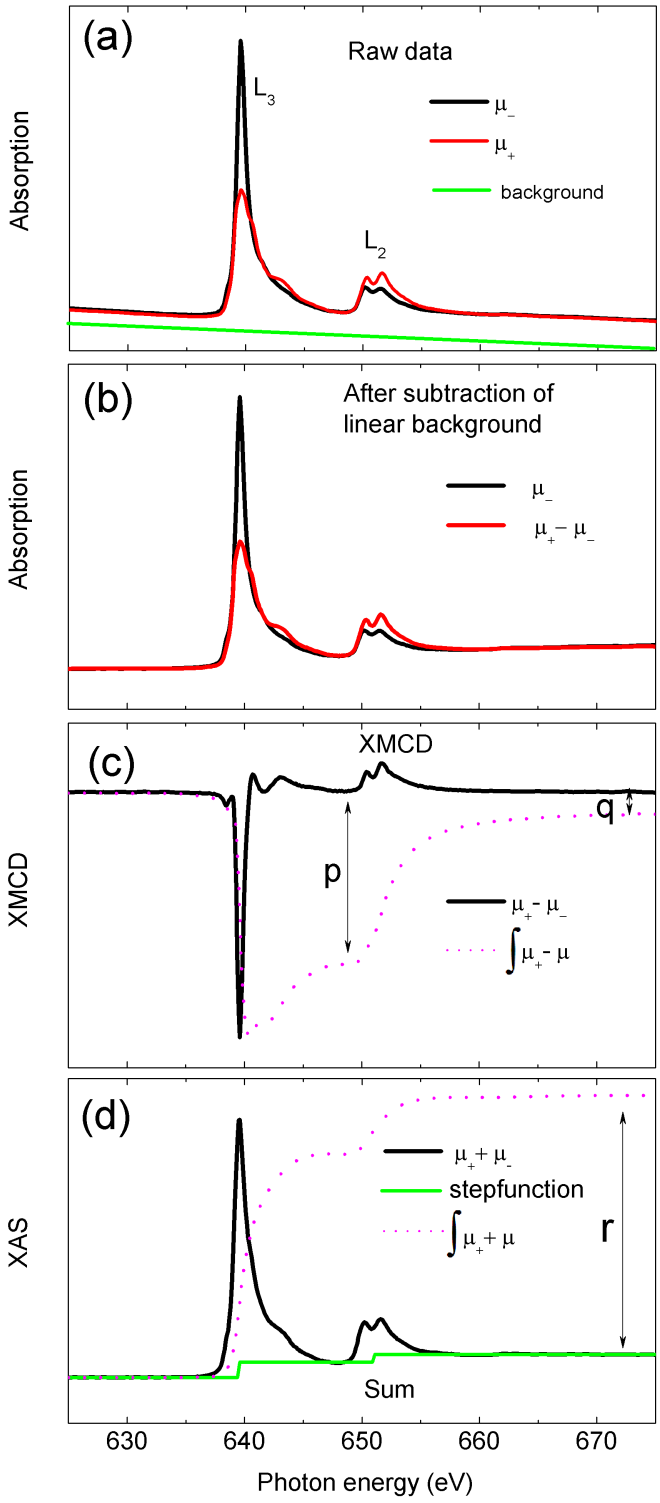

Figure 2.15 – The application of the Sum Rules to the Mn $L_{3,2}$ edges. (a) shows the raw XAS for the two opposite circular polarisation signs along with an estimated background. (b) shows the same two scan with background subtracted. (c) XMCD generated by the difference of the two scans. (d) removal of a step function the heights of which are based on the degeneracy of the initial $2p$ levels.

Chapter 3

Fe/(Ga,Mn)As bilayers

Introduction

Despite being of wide spread interest from the point of view of fundamental physics research, (Ga,Mn)As and other DMS have not yet fulfilled there potential commercially [2]. The mainstream applicability of (Ga,Mn)As is limited by its relatively low Curie temperature (T_C), which at time of writing, stands at a maximum of ~185 K for bulk material [25], and considerably less for heterostructures. Efforts to increase the T_C have met with diminishing returns, owing to the highly non-equilibrium growth conditions needed to incorporate high concentrations of Mn substitutionally.

A recent study of an hybrid metal/semiconductor system, namely a Fe/(Ga,Mn)As bilayer system, reported a proximity polarisation effect in the near surface region of the (Ga,Mn)As which coupled antiferromagnetically to the Fe, and persisted above room temperature [49]. This could potentially offer a way of side stepping the limiting T_C of current DMS layers. However, in the aforementioned study the Fe layers were deposited post growth.This involved the exposure to air of the underlying (Ga,Mn)As layer, which was then sputtered to remove oxides before the Fe layer was finally deposited. This process, combined with the highly non-equilibrium nature of the material, may have led to any number of surface irregularities and could have affected the subsequent interpretation of results. In addition, no information was given on the magnetic behaviour away from the coupled near-surface interface layer.
In order to clarify and extend this previous work, Fe/(Ga,Mn)As heterostructures were grown and capped entirely in situ, then examined using x-ray magnetic cir-

cular dichroism(XMCD) to probe, in an element specific way, the nature of the apparent induced magnetism and coupling in this system.

3.1 Sample preparation

Since part of the aim of this experiment was to examine an ultrathin polarised layer, the previous study by Maccherozzi et al [49] gave a room temperature polarised thickness of the order of nanometres, it was known that the quality of the interfaces would be of critical importance. In order to obtain optimal interface qualities the entire heterostructures were grown in situ without breaking vacuum, including a capping layer of Al to prevent oxidation on exposure to air.

The (Ga,Mn)As layers were deposited at 260 °C using previously established growth methods [25, 68] with nominal Mn concentration of x=3 or 6 %. Following the (Ga,Mn)As layer growth, the temperature was lowered to 0 °C and a small amount of Ga was deposited, the amount was calculated to reinstate stoichiometric surface conditions (standard (Ga,Mn)As growth leaves an As rich surface which protects surface quality). Fe was then deposited at 0 °C, and finally the heterostructures were capped with 2 nm of Al. RHEED measurements during growth confirm that 2D growth occurred for all layers. In order to rule out certain spurious effects, three separate control samples were grown along with the primary heterostructure. The sample structures that were grown are depicted diagrammatically in Figure 3.1. The primary heterostructure is depicted in Figure 3.1 (a), and the control samples are shown in (b), (c) and (d). The detailed layer structure of the studied Fe/(Ga,Mn)As samples are given in Table 3.1.

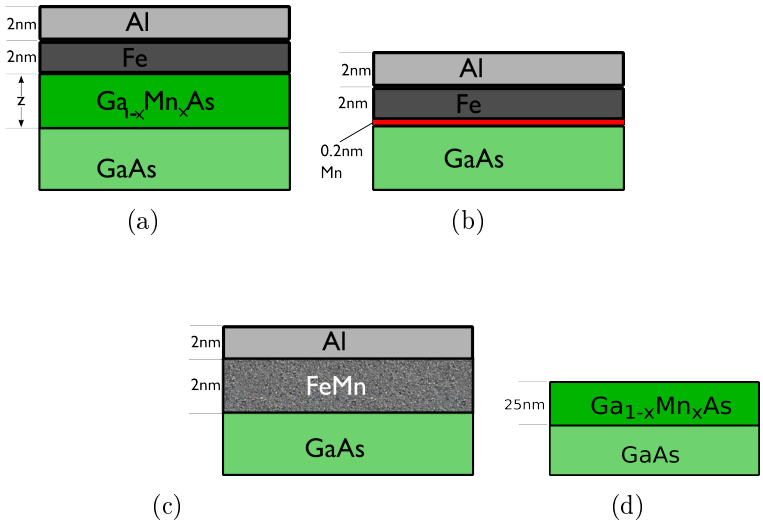

Figure 3.1 – (a) shows the structure of the main samples, with z representing the different thickness examined (2, 10, 20 and 50nm) , (b) has a small layer of Mn deposited at the GaAs/Fe interface, (c) has a Fe,Mn alloy and (d) has no Fe layer

sample	layer structure	nominal value of x (%)
Mn509	2 nm Al/2 nm Fe/20 nm $(Ga_{(1-x)}Mn_x)As$	3
Mn539	2 nm Al/2 nm Fe/10 nm $(Ga_{(1-x)}Mn_x)As$	3
Mn511	2 nm Al/2 nm Fe/2 nm $(Ga_{(1-x)}Mn_x)As$	3
Mn510	2 nm Al/20 nm $(Ga_{(1-x)}Mn_x)As$	3
Mn574	1.6 nm Al/1.4 nm Fe/20 nm $(Ga_{(1-x)}Mn_x)As$	3
Mn524	2 nm Al/2 nm Fe	na
Mn512	2 nm Al/2 nm $Fe_{1-x}Mn_x$ (Fe,Mn alloy)	3
Mn513	2 nm Al/2 nm Fe/0.1ML Mn (Fe/Mn bilayer)	na

Table 3.1 – list of studied samples

3.1.1 Calibration of the growth rate for monocrystalline Fe

The growth rates for (Ga,Mn)As are well established for the MBE system used, and are highly repeatable, however the Fe growth had not previously been carried out on this system. Wastlbaur et al conducted an extensive study of Fe layers grown on GaAs(001) which provided the starting point [69]. Test samples of Fe were grown on GaAs(001) prior to growth of the samples used in this study. In order to accurately calibrate the Fe growth rate an estimated 5nm of Fe was grown on top of a GaAs substrate, and then capped with a further 20nm of polycrystalline GaAs. X-ray reflectivity was performed on these calibration samples using a PANalytical X'Pert Materials Research Diffractometer, using a Cu K alpha source (1.5418Å) . The diffractometer was employed in grazing incidence alignment, scanning from 0.1° to 3° in 2θ. Although not optimal for reflectivity, the machine was used in the same configuration as per a normal $2\theta\omega$ line scan with the addition of a beam knife and a 1/4° slit immediately before the detector to improve resolution. This provided a good compromise between resolution and speed, and allowed for quick feedback during the growth of this series of samples.

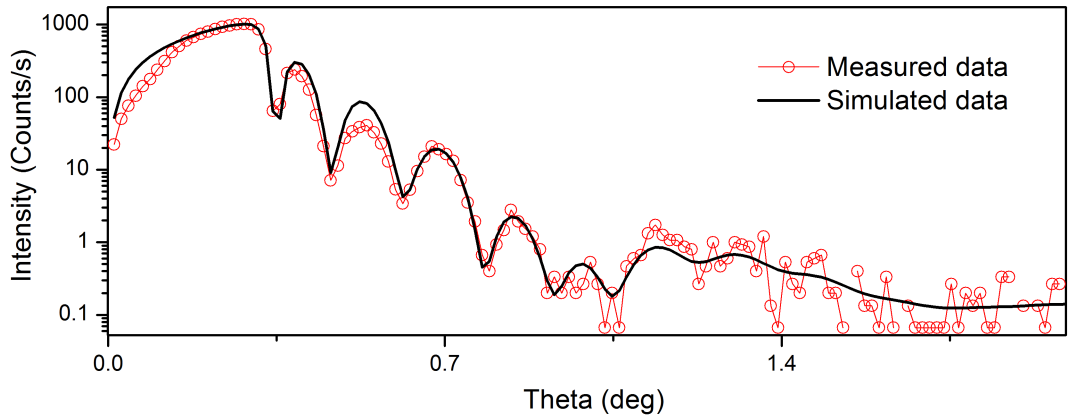

Figure 3.2 – reflectivity data for Fe growth calibration sample(red line) and a model fitting using values shown in Table 3.2(black line)

The resulting data, which is shown in Figure 3.2, were fitted using a standard reflectivity fitting software package (Panalytical X'pert reflectivity). The data provide rich structure which is well reproduced by fitting with a simple model, and gives good confidence in the results. The parameters extracted from the fit show good calibration of growth thickness and sub nanometre roughness at the GaAs/Fe interface, as shown in Table 3.2.

layer	thickness (nm)	roughness (nm)
GaAs substrate	na	0.1±0.1
Fe	5.1±0.3	0.5±0.2
GaAs	20.9±0.4	1.2±0.2

Table 3.2 – Fitting values for the XRR model

3.1.2 Bulk magnetometry

Previously performed SQUID measurements on Fe and (Ga,Mn)As layers grown separately, but under the same growth condition, reveal the expected individual anisotropies of the different layers [70]. The Fe layer possesses uniaxial anisotropy along the [1 1 0] in agreement with previous studies [69]. For the (Ga,Mn)As layer there is competition between uniaxial and cubic anisotropy which has been widely reported. The cubic anisotropy dominates at low temperatures with easy axes along the in-plane $\langle 1\,0\,0 \rangle$ directions. Uniaxial anisotropy dominates close to T_C with easy axis along the $[1\,\bar{1}\,0]$. The anisotropies for the various layers are depicted schematically in Figure 3.3.

Figure 3.4 (a) shows the low temperature hysteresis loop of a Fe/(Ga,Mn)As bilayer. The loop can be seen to undergo a two-step magnetisation reversal. Upon comparison to the control sample without Fe (Mn510)(shown in blue), the smaller loop can be attributed to the (Ga,Mn)As layer alone. The minor loop is clearly offset from zero by an exchange bias field.

Figure 3.4 (b) shows magnetisation versus temperature measurements for a Fe/(Ga,Mn)As film and the Al/(Ga,Mn)As control sample. There is a clear difference between the remnant cooling, and a field cool with 500 Oe applied for Fe/(Ga,Mn)As samples. This manifests itself close to the T_C of the (Ga,Mn)As layer and matches very closely, in both magnitude and shape, to the (Ga,Mn)As control sample, albeit inverted. This strongly implies that not only is the (Ga,Mn)As layer homogeneously magnetised but also that it is aligned antiparallel to the Fe layer at remnance.

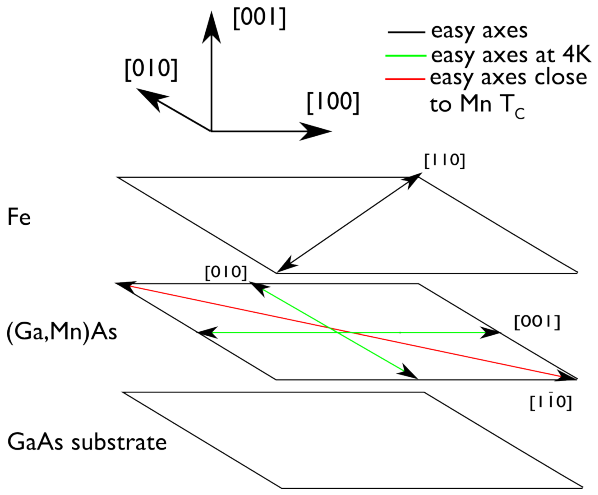

Figure 3.3 – The anisotropies of the separate layers as revealed by SQUID magnetometry of control samples Mn510 and Mn524 (see Table 3.1)

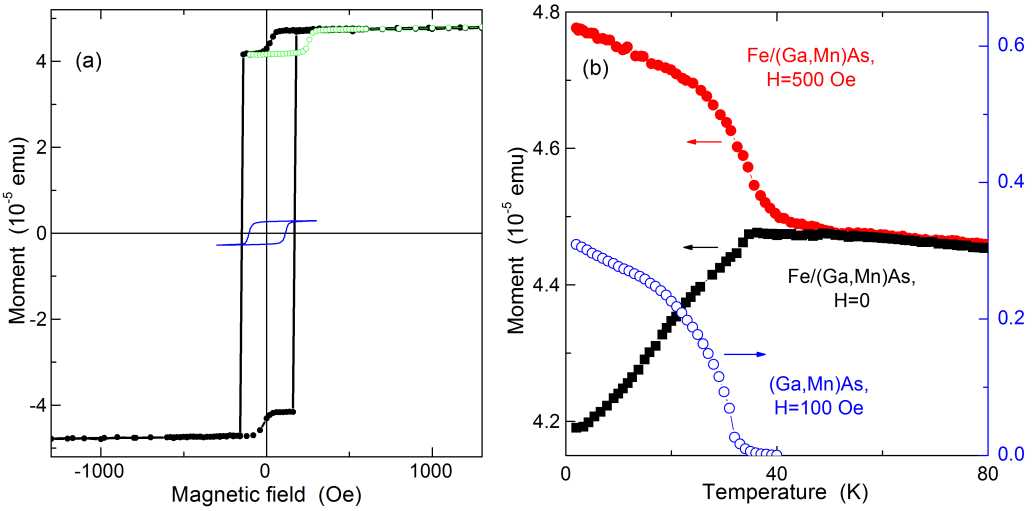

Figure 3.4 – (a) Hysteresis loop for Fe/(Ga,Mn)As (Mn509) (black circles), part of minor loop (green circles) and (Ga,Mn)As control sample (blue line). The measurements were taken at 2 K with the field applied along the $[1\,1\,0]$ direction in both cases. (b) Fe/(Ga,Mn)As zero field cool (black squares), field cool with 500 Oe applied along the $[1\,1\,0]$(red circles), and (Ga,Mn)As control sample (blue circles).

3.2 XMCD measurements

Antiferromagnetic coupling was observed in the SQUID measurement for the entire (Ga,Mn)As layer at low temperature, and was also reported for a thin interfacial layer, in a previous study at room temperature [49]. In order to explore the nature of the coupling in our layers more precisely, XMCD at the Mn and Fe $L_{2,3}$

edge was used to provide element specific information. The element specificity of XMCD inherently allowed for the separation of the magnetic signals of the Fe and (Ga,Mn)As layers. This also allowed the generation of element specific hysteresis curves, by measuring the size of the XMCD signal at a specific energy as a function of field.

The measurements were carried out at beamlines 4.0.2 and 6.3.1 of the Advanced Light Source(ALS) and I06 at Diamond Light Source (DLS). The XMCD from measurements at the ALS were obtained by flipping the field direction at each energy point. The resulting data file, containing two interleaved XA spectra, is here referred to as one scan. Scans were taken in pairs, one with each polarisation sense. At the DLS the field switching (using a field superconducting magnet) was not fast enough to be performed at each energy step. For the DLS data two XA scans were taken consecutively, one with each polarisation sense, followed by a change in field direction and repeat of the two scans. Provided that the applied field is greater than the exchange bias and coercive field, this results again in two degenerate pairs. Owing to the symmetrical degeneracy, averaging between the two pairs is found to substantially remove systematic errors relating to equipment set-up, and was used wherever possible.

By using two different decay products as a measurement of the XA spectra it is possible to obtain XMCD over two differing probing depths. The two decay products used were total electron yield (TEY) and fluorescent yield (FY). In order to make confident conclusions regarding the results of these two probing techniques, it is necessary to know precisely which parts of the heterostructure are contributing and to what degree. The probing depth for FY depends entirely on the attenuation length of the x-rays in (Ga,Mn)As. The escape depth for total electron yield over the L edges of transition metals is typically quoted as being several nanometres. Since this value is critical to the analysis it was checked for our particular heterostructures, and this is discussed in the subsequent sections.

3.2.1 Attenuation length in (Ga,Mn)As

The attenuation length of x-ray photons over the relevant energy range is an important factor in the subsequent determination of the electron escape depth. This is because the calculation of the electron escape depth implicitly assumes uniform intensity over the 20 nm used in the integral (see Section 3.2.2). If a significant amount of attenuation occurs over this length then the result is invalid.

The website of The Centre for X-ray Optics [71] was used to obtain the attenuation length per unit density of the constituent elements. Using the unit cell for GaAs

with a lattice parameter of 5.65 Å and a value of 3 % for the Mn concentration on Ga sites, combined with the attenuation length data, this was used to obtain the absorption cross section for each element. The three contributions were then added to give a final attenuation length, at the Mn $L_{3,2}$ absorption edges, for (Ga,Mn)As of 561 nm. This results in a 3.5% decrease in intensity over the first 20nm for normal incidence and a 7% decrease for the 30° grazing incident measurements, and so does not significantly affect the calculation of the electron escape depth.

3.2.2 Escape depth of electrons from Al/Fe/GaMnAs heterostructures

The escape depth of electrons over the $L_{3,2}$ edges of $3d$ metals is typically quoted as being of the order of nanometres [72]. This value reveals how much of the sample is contributing significantly to the signal for measurements taken in total electron yield mode. Since the samples under study are heterostructures, it is obviously desirable to know this as accurately as possible, and so this was checked using the same samples and experimental set-up. This was done by comparing the XA spectra for two of the Fe/(Ga,Mn)As samples with differing (Ga,Mn)As layer thickness (2 nm and 20 nm of (Ga,Mn)As) to each other. Assuming uniform illumination throughout the layer, the measured electron yield signal, I, from a given layer depth, z, is given by the relation:

$$I = I_0 \, exp^{(\frac{-z}{\lambda})} \tag{3.1}$$

where λ is the electron escape depth and I_0 is the TEY signal generated by the top-most layer of the (Ga,Mn)As. The contribution to the measured signal is given by integrating between zero and z, so for the two samples:

$$S_2 = \int_0^2 I_0 \, exp^{(\frac{-z}{\lambda})} \, dz = \left[-I_0 \, \lambda \, exp^{(\frac{-z}{\lambda})} \right]_0^2 \tag{3.2}$$

$$S_{20} = \int_0^{20} I_0 \, exp^{(\frac{-z}{\lambda})} \, dz = \left[-I_0 \, \lambda \, exp^{(\frac{-z}{\lambda})} \right]_0^{20} \tag{3.3}$$

defining k as the ratio of these two equations:

$$k = \frac{S_2}{S_{20}} = \frac{e^{\frac{-2}{\lambda}} - 1}{e^{\frac{-20}{\lambda}} - 1} \tag{3.4}$$

for λ of the order of a few nanometres $e^{\frac{-20}{\lambda}} << 1$ and so can be safely discounted, which gives:

$$k = \frac{e^{\frac{-2}{\lambda}-1}}{-1} \tag{3.5}$$

rearranging gives:

$$\lambda = \frac{-2}{ln(1-k)} \tag{3.6}$$

k can be found from the ratio of the Mn $L_{3,2}$ XAS peak intensity for the 20 nm film and the 2 nm film. Using an average of several XAS curves for Mn511 (2 nm) and Mn509 (20 nm), k is found to be 0.50 (see Figure 3.5). Using this value in Equation 3.6 gives an escape depth, $\lambda = 2.9\,nm$, which is in reasonable agreement with other studies of metallic systems.

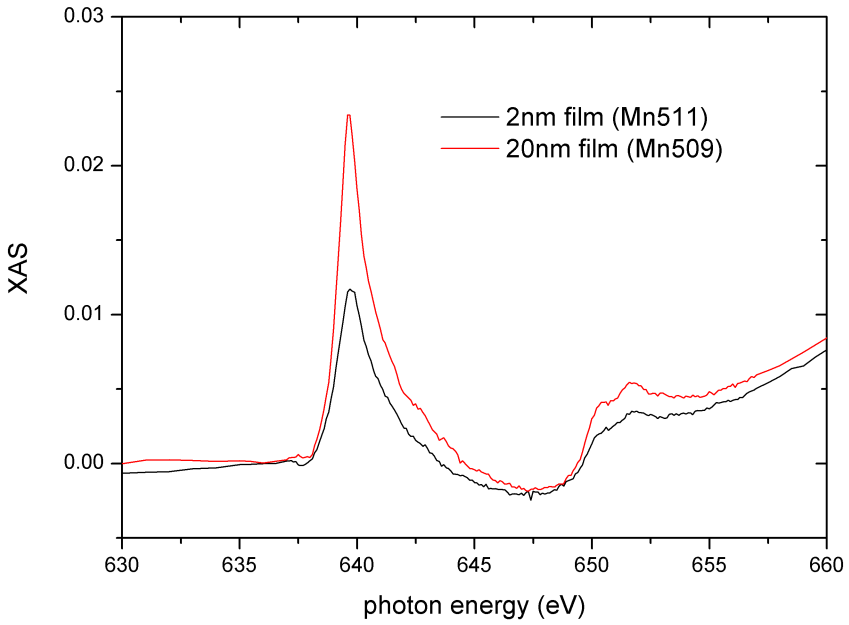

Figure 3.5 – Average XA spectra for Fe/(Ga,Mn)As samples with 2 nm (black) and 20 nm (red) (Ga,Mn)As layers used to calculated the electron escape depth.

This shows conveniently, that whereas the FY signal can be used as a measure of the entire layer, the TEY signal will be dominated by the surface region. This

provides a good basis for not only element specific determination of magnetic behaviour, but also layer specific.

3.2.3 XMCD at the Fe $L_{3,2}$ edge

XMCD measurements were taken at the Fe $L_{3,2}$ absorption edge to provide information on the magnetic and chemical properties of the Fe layer. Since the measurements were performed some months after the growth of the samples, it was important to establish whether the capping layer had protected the samples from further oxidation. Measurements were performed at room temperature at the ALS and at approximately 2 K at DLS. The XMCD data presented in this section was taken from a sample with 20 nm (Ga,Mn)As and structure as shown in Figure 3.1(a). The sample was aligned at a grazing angle of $\theta = 30°$ to the incident beam, where θ refers to the angle between the surface and the beam, not the surface normal. Since the field was applied along the beam direction, either parallel or anti-parallel, it was thought prudent to calculate to what extent this would pull the Fe moments out of plane. This is discussed in the next section.

Deviation of Fe magnetic moments from in-plane

A simple Stoner-Wohlfarth model was applied to this scenario to estimate the size of this effect, and determine what, if any, corrections need applying to the calculated magnetic moments. The problem was reduced to a simple uniaxial model, depicted in Figure 3.6, where the energy of the system is given by:

$$E = K\,V\,sin^2(\phi - \theta) - \mu_0\,M_s\,V\,H\,cos(\phi) \tag{3.7}$$

Where E is the energy of the system, K is the anisotropy constant, V is the sample volume, M_s is the saturation moment, and H is the magnetic field. Dividing through by V and M_s, and defining $\epsilon = \frac{E}{V\,M_s}$ gives:

$$\epsilon = \frac{K}{M_s}\,sin^2(\phi - \theta) - \mu_0\,H\,cos(\phi) \tag{3.8}$$

θφ

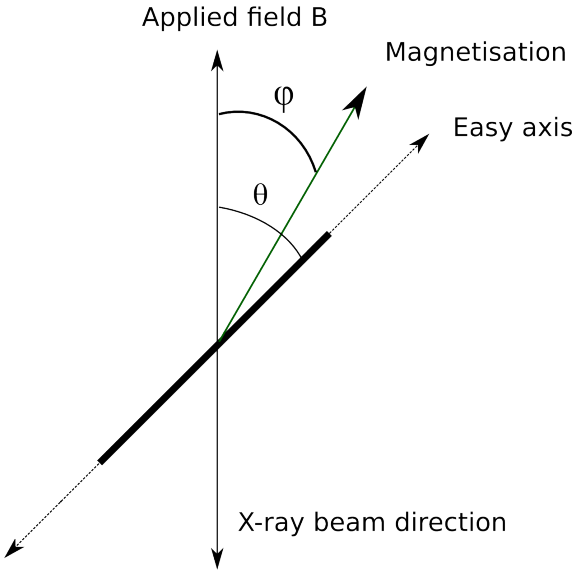

Figure 3.6 – The angles ψ and θ defined for use in a Stoner-Wohlfarth model of the Fe magnetisation under the influence of an applied field

Where $\mu_0 H$ is simply the applied field, B, and $\frac{K}{M_s}$ is the anisotropy field, B_K, which leads to:

$$\epsilon = B_K \, sin^2(\phi - \theta) - B \, cos(\phi) \tag{3.9}$$

Differentiating and equating to zero yields the stationary points, and taking only those where the second differential is positive gives the energy minima of the system. Solving for ϕ leads to two minima, but since the applied field is above the coercive field only one solution is valid. The anisotropy field is estimated to lie between 1 T and 3 T from hysteretic measurements along the hard axis, so using the value of θ=30° and a range of anisotropy fields from 1 T to 3 T leads to values of ϕ from 27.3° to 28.6° respectively, which corresponds to a deviation from in-plane of 2.7° and 1.4° respectively, with an applied field of 0.5 T. This is shown graphically as an energy landscape plotted against anisotropy field in Figure 3.7. Even the largest value of ϕ predicted will have a negligible affect on the results, and so the magnetisation is assumed to lie in-plane and the moment values shown have been corrected for a 30° angle.

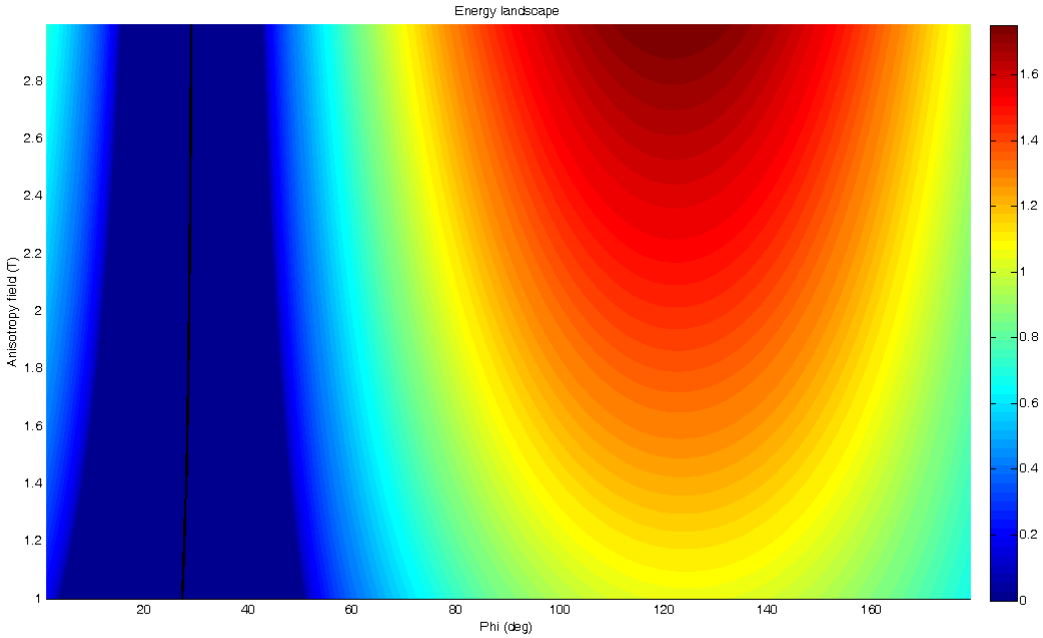

Figure 3.7 – Energy landscape for the Stoner-Wohlfarth model as a function of anisotropy field and angle ϕ.

XAS lineshape and Hysteretic behaviour

In Figure3.8 the XMCD hysteresis confirms the continued single domain behaviour of the Fe layer (after a period of months in atmospheric conditions). The XA spectra shown in Figure 3.9 have a very smooth metallic shape, characteristic of pure Fe, as in [73]. If significant oxidation had occurred extra features would appear, due to oxidised states, which visibly affect the XAS [74–76]. This is further supported by XMCD sum rules calculations which yield total moment per Fe atom close to that obtained by Chen et al for single crystal Fe layers [62](see Table 3.3).

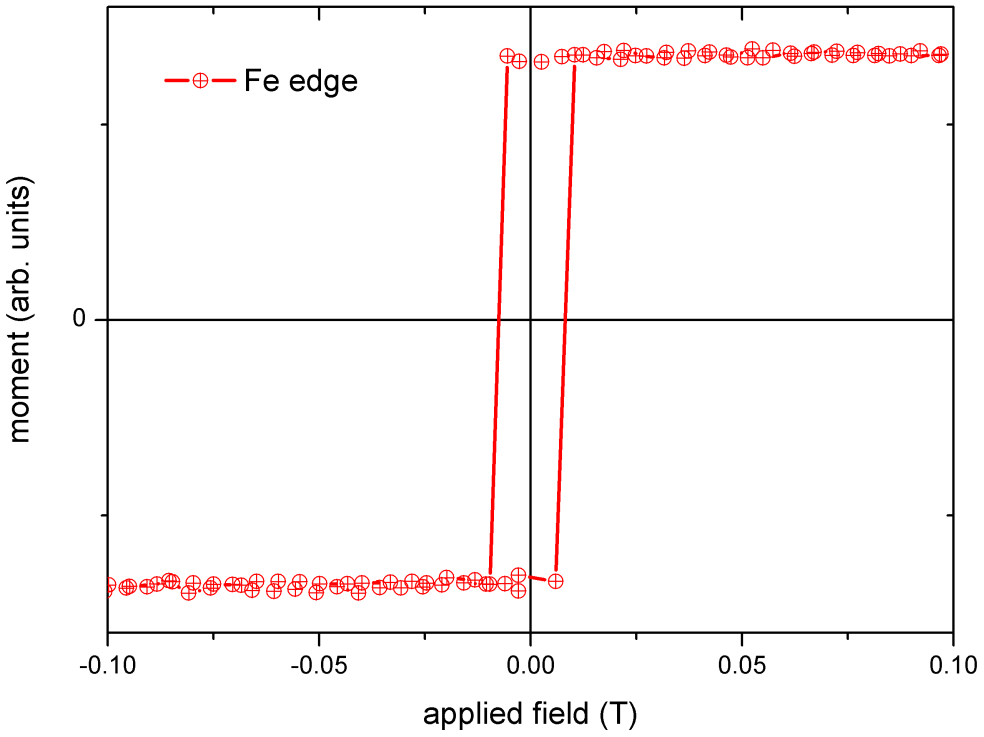

Figure 3.8 – Hysteresis loop produced by measuring asymmetry at the Fe L_3 absorption edge during a field sweep.

Sample	m_{orb}/m_{spin}	m_{orb}	m_{spin}
Fe/(Ga,Mn)As layers	0.037	0.060 ± 0.007	1.63 ± 0.03
XMCD of Fe by Chen et al [62]	0.043	0.085	1.98

Table 3.3 – Fe magnetic moments measured by XMCD

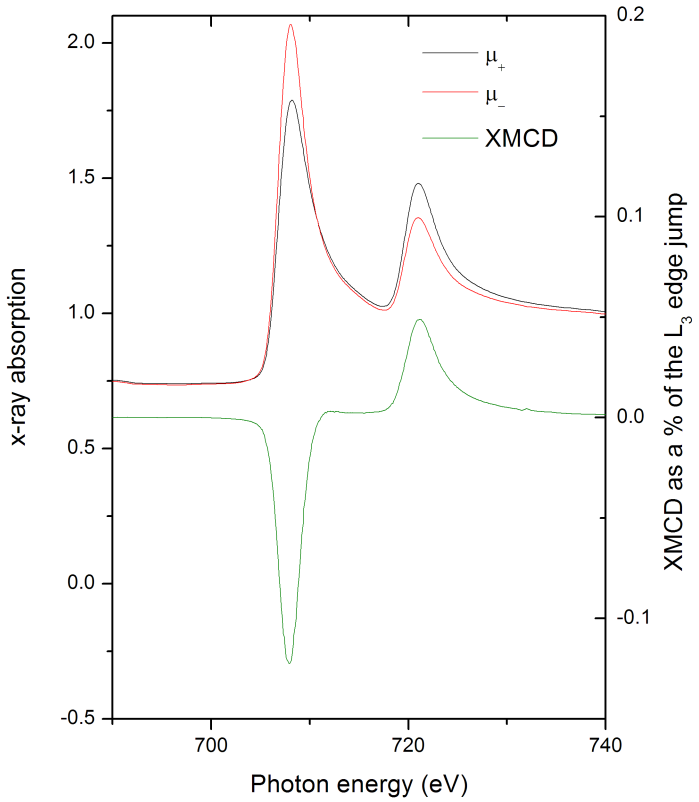

Figure 3.9 – X-ray absorption and XMCD curves for the Fe $L_{3,2}$ edge of Mn509 at room temperature at beamline 6.3.1 of the ALS with 0.5 T applied field.

3.2.4 XMCD at the Mn $L_{2,3}$ edge

Room temperature XMCD line shape

The spectra discussed in this section were all taken on beamline 4.0.2 of the ALS using TEY detection. It is worth noting that this means the resulting spectra are heavily influenced by the top few nanometres of the absorbing layer. Figure 3.10 shows the Mn $L_{3,2}$ XAS, with both negative and positive circular polarisation at room temperature, for the Fe/(Ga,Mn)As sample Mn574. The XMCD is small but clearly visible. Figure 3.11 depicts the normalised Mn $L_{3,2}$ XMCD line shapes for the Fe/(Ga,Mn)As samples at room temperature as well as the Mn/Fe control sample, a low temperature (Ga,Mn)As layer and metallic MnAs. The Mn/Fe sample has the layer structure depicted in 3.1(b). The Fe/(Ga,Mn)As curve is the average of many XMCD spectra from a range of samples measured at room temperature, all with the basic structure shown in Figure 3.1(a). Each one of the samples averaged had identical lineshape and the average was only taken to improve signal to noise ratio. This can be seen in the published work by Oleynik *et al* [77] where only the first sample was used.

The Fe/(Ga,Mn)As XMCD curve has a relatively sharp L_3 dichroism peak indicating a largely localised magnetic moment. The shape is essentially that of Mn^{2+} localised configuration (see Figure 4.5, Chapter 4). The Mn does not appear to be in a metallic environment, which can be seen from comparison to the more metallic MnAs which has a much broader L_3 dichroic peak. This can also be compared to the FeMn alloy in Figure 3.12, which is also far broader and has a different branching ratio of the L_3 to L_2 peaks. There is slight broadening on the low energy side of the L_3 for the Fe/(Ga,Mn)As samples as compared to the LT (Ga,Mn)As, which could be due to different screening caused by the proximity of the Fe layer. It is also worth noting that there is a slight shift to lower energy of $\approx 0.1\,\mathrm{eV}$, which is also reported by Maccherozzi et al [49]

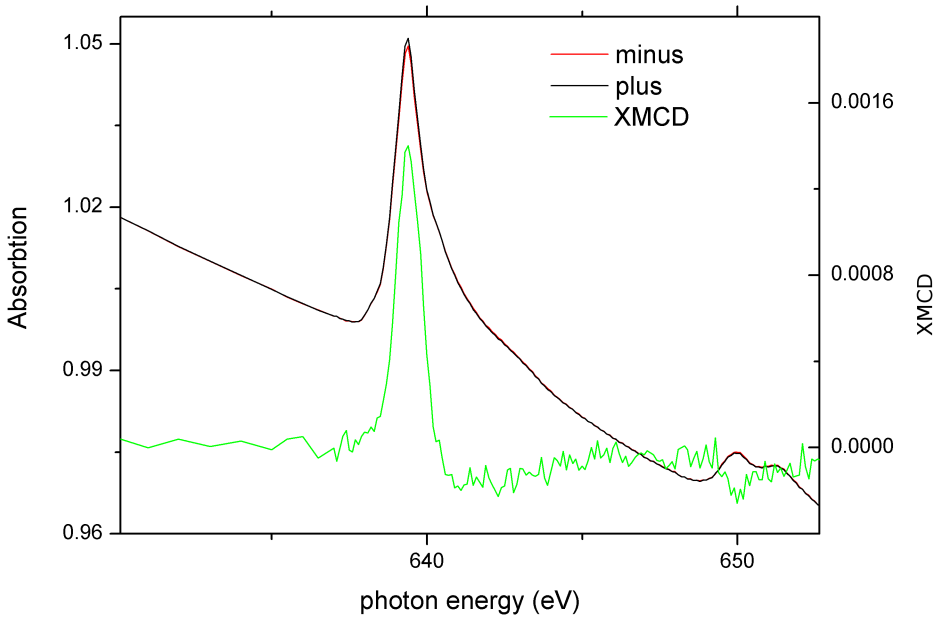

Figure 3.10 – XAS curves for positive and negative circular polarisation, together with resultant XMCD at the Mn $L_{3,2}$ absorption edge for the Fe/(Ga,Mn)As sample Mn574 at room temperature.

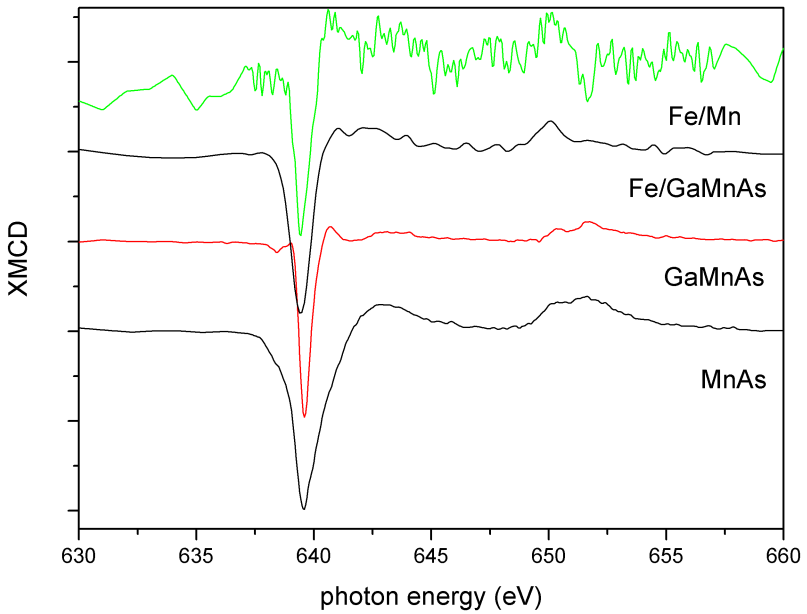

Figure 3.11 – Comparison of room temperature XMCD lineshapes of the main Fe/(Ga,Mn)As samples and control samples against well characterised (Ga,Mn)As and metallic MnAs at $\sim 15\,K$ (MnAs data reproduced from Edmonds *et al* [78]). For the Fe/Mn bilayer and Fe/(Ga,Mn)As samples the sign of the XMCD has been changed to aid comparison.

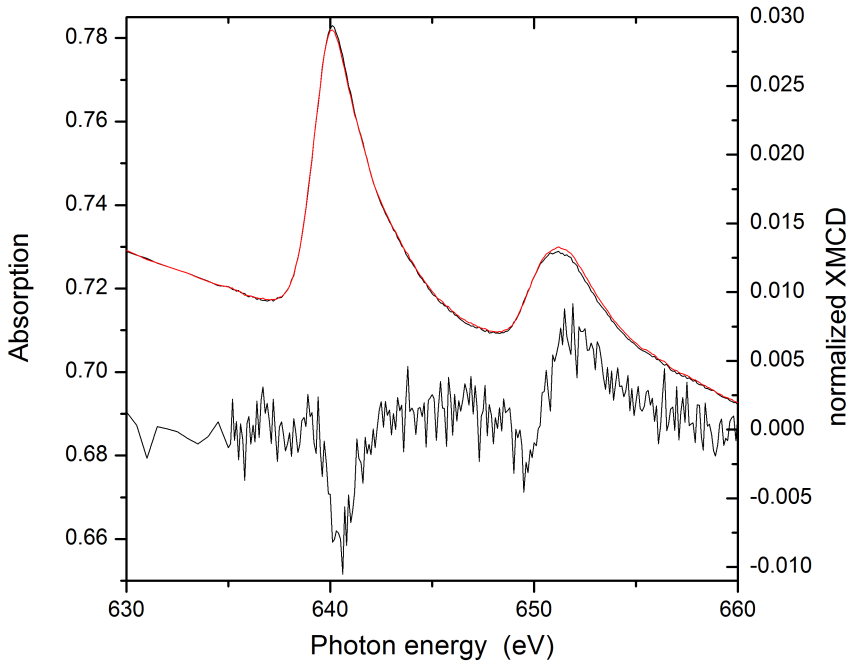

Figure 3.12 – Polarised XAS and XMCD of the FeMn control sample

Low temperature hysteretic behaviour

The results discussed in this section were taken at I06 of the DLS. The temperature was approximately 2 K and the samples were aligned at a grazing incidence of 30° to the beam. The resulting signal was measured by TEY and FY simultaneously, and thus the TEY and FY graphs depicted in Figure 3.13 represent different probing depths of the sample.

The XMCD for the Fe edge displays square hysteretic behaviour, shown in Figure 3.8 (a), as expected for monocrystalline Fe with strong uniaxial anisotropy [69]. The behaviour of the Mn is more complicated owing to the coupling between the layers. There are clear differences observed between the bulk layer (FY) and the interfacial region (TEY). Features general to both curves are the anti-parallel alignment of the Mn moment at remnance and a magnetization reversal which is opposite in sign to the Fe layer. As the field increases the net Mn moment rotates from antiparallel alignment into parallel alignment with the Fe. For the TEY curve it is clear there is some degree of frustration as the moment never fully recovers its remnant magnitude.

For the FY curve the magnitude of the moment at remnance is matched by the moment at saturation. The majority of the signal in this case originates from the bulk layer, which strongly implies that the bulk (Ga,Mn)As layer is behaving as a single domain ferromagnet at remnance with antiparallel alignment to the Fe moment. At higher fields it is rotated into alignment with the field.

For the TEY XMCD it is apparent that the moment at remnance is approximately twice the size of the value at saturation, even at field strengths of 20 kOe (maximum field applied). This shows that the Mn moments near the surface have a lower net value at high field than low field. The strongly coupled interfacial layer is ascribed to the proximity polarisation of the Mn ions near to the Fe layer. This was previously reported by Maccherozzi et al [49] by XMCD and ab initio modelling. Further evidence of this is seen by XMCD above T_C where a small but non-negligible Mn moment remains (see Figure 3.10). This is antiferromagnetically coupled to the Fe layer even at high magnetic field.

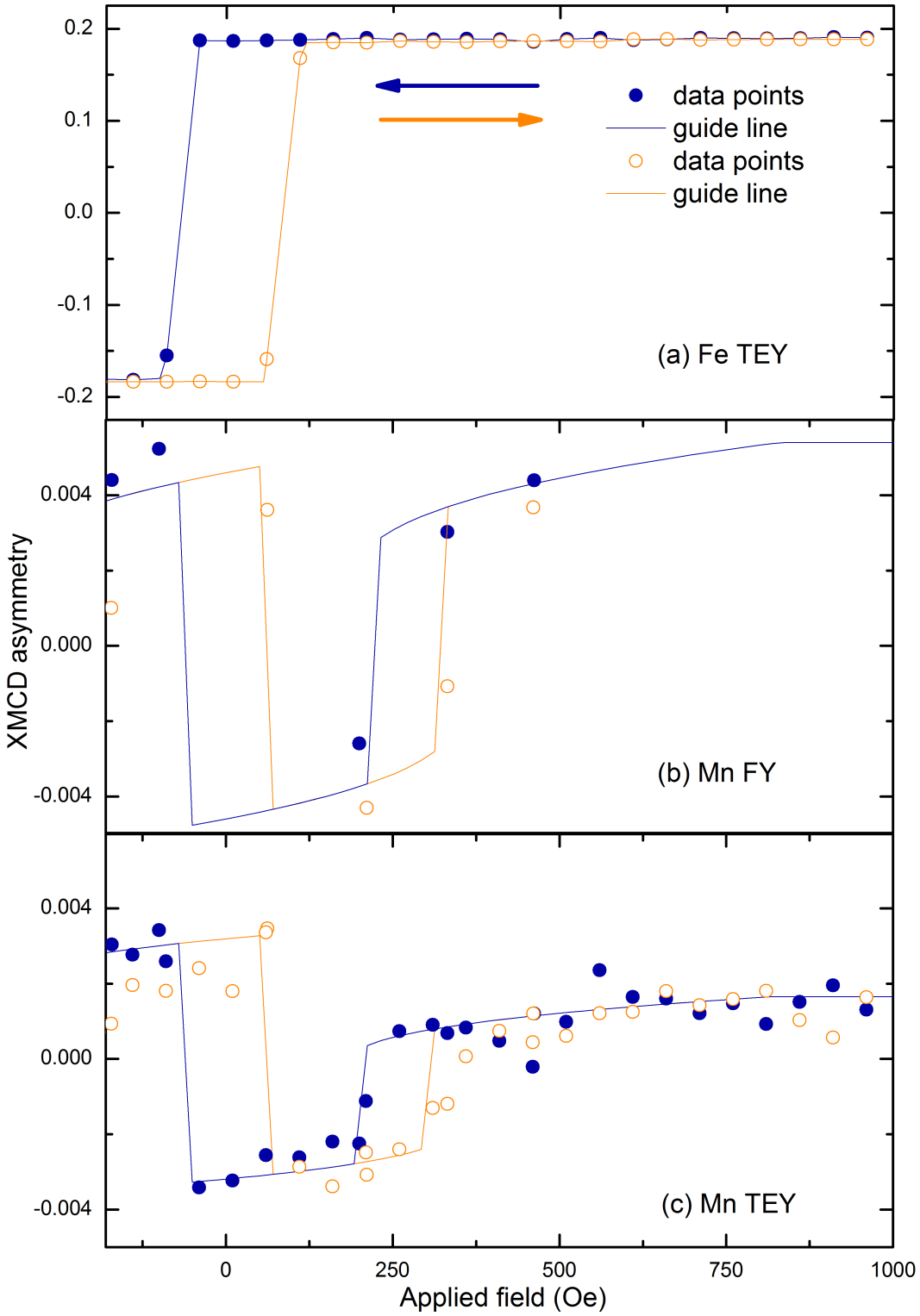

Figure 3.13 – XMCD hysteresis loops for Mn539 measured using FY and TEY. The open circles represent data points calculated using the asymmetry of an entire XAS pair. The lines are guides to the eye based on magnetic modelling by J. Haigh [70].

Sum rules analysis

Applying XMCD sum rules to the TEY data and using similar data from well characterised (Ga,Mn)As layers it is possible to obtain the projected 3d magnetic

moments. This yields values of -1.1 μ_B and 0.5 μ_B, at remnance and 1000 Oe respectively. The difference between these two values, of 0.6 μ_B, is ascribed to the strongly antiferromagnetically coupled interfacial layer. At remnance both the interfacial layer and the bulk (Ga,Mn)As are aligned and so both contribute positively to the XMCD signal. At saturation the bulk (Ga,Mn)As has been rotated into alignment with the external magnetic field whereas the interfacial layer remains antiferromagnetically aligned to the Fe, and thus the XMCD is now the difference between the two contributions (depicted diagrammatically in Figure 3.14).

Thickness of the strongly coupled layer

Assuming that the Mn is uniformly distributed throughout the (Ga,Mn)As layer, and that all the Mn ions have identical total moment, then it is possible to calculate the thickness of the strongly coupled layer using either the XMCD asymmetry values or, as is used here, the sum rules calculated values of moment per atom, for the two scenarios shown in Figure 3.14. This is possible because the measured signal or sum rules moment is an amalgamation of the contributions of all of the probed Mn atoms, and this contribution dies off exponentially with depth.

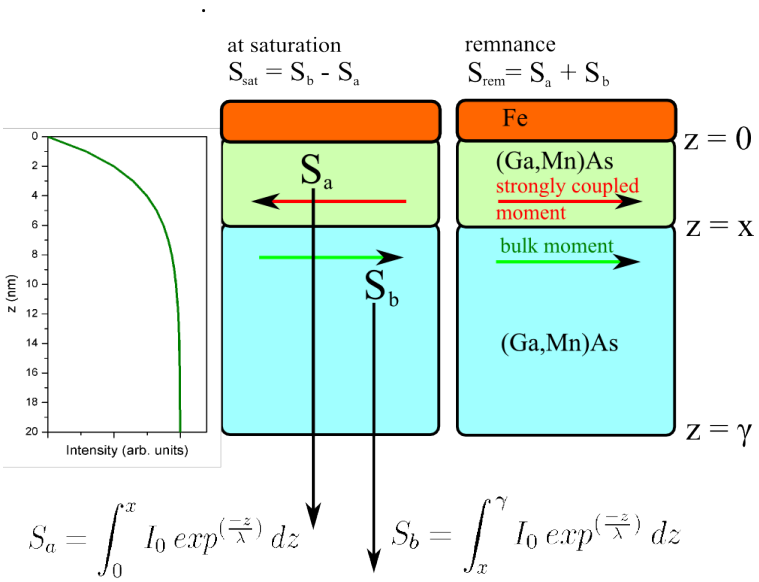

Figure 3.14 – Model of interface between the strongly coupled and bulk (Ga,Mn)As layer in Fe/(Ga,Mn)As samples, which was used to calculate the thickness of the strongly coupled layer. S_a and S_b are the contributions to the sum rules calculated moment per atom of the interface layer and bulk layer respectively, and S_{sat} and S_{rem} are the sum of S_a and S_b with a saturating magnetic field applied and at remnance respectively. In this case I_0 corresponds to the unattenuated signal at the surface of the (Ga,Mn)As layer.

$$-S_{rem} = S_a + S_b = 1.1\mu_B$$
$$S_{sat} = S_b - S_a = 0.5\mu_B$$

which gives:

$$S_a = 0.3\mu_B$$
$$S_b = 0.8\mu_B$$

now let:

$$U = \frac{S_a}{S_b} = \frac{0.3}{0.8} \tag{3.10}$$

where:

$$\begin{aligned} S_a = \int_0^x I(z)\,dz = \int_0^x I_0\, exp^{(\frac{-z}{\lambda})}\,dz \\ = \left[-\lambda\, I_0\, exp^{(\frac{-z}{\lambda})}\right]_0^x \\ S_a = \lambda\, I_0(1 - exp^{(\frac{-x}{\lambda})}) \end{aligned} \tag{3.11}$$

$$\begin{aligned} S_b = \int_x^\gamma I(z)\,dz = \int_x^\gamma I_0\, exp^{(\frac{-z}{\lambda})}\,dz \\ = \left[-\lambda\, I_0\, exp^{(\frac{-z}{\lambda})}\right]_x^\gamma \\ S_b = \lambda\, I_0(exp^{(\frac{-x}{\lambda})} - exp^{(\frac{-\gamma}{\lambda})}) \end{aligned} \tag{3.12}$$

substituting Equation 3.11 and 3.12 into Equation 3.10 and rearranging for x yields:

$$x = -\lambda \, ln \left(\frac{1 + U \, exp^{\frac{-\gamma}{\lambda}}}{1 + U} \right) \tag{3.13}$$

in the case of layers thicker than 10 nm $exp^{\frac{-\gamma}{\lambda}} \ll 1$ which leads to:

$$\begin{aligned} x &= -\lambda \, ln \left(\frac{1}{1 + U} \right) \\ &= -\lambda \left(ln(1) - ln(1 + U) \right) \\ &= \lambda \, ln(1 + U) \end{aligned} \tag{3.14}$$

Using the value of 2.9 calculated for the electron escape depth, together with a value for U of 0.375 calculated from the sum rules determined total moment for Mn539 (10nm (Ga,Mn)As layer) in Equation 3.13 gives a thickness value for the strongly coupled layer of $x = 0.9\,nm$

3.2.5 Conclusions and discussion

XMCD combined with prior SQUID measurements show a detailed picture of the coupling between the metallic Fe film and the semiconducting (Ga,Mn)As layer. Comparison between FY and TEY XMCD asymmetry hysteresis loops show that the (Ga,Mn)As layer is magnetised homogeneously at low field, and aligns itself antiparallel to the Fe. This can be seen directly from the opposite sign of the fluorescent Mn XMCD to that of the Fe XMCD at remnance. This is also supported by the previously performed SQUID magnetometry, where the difference between field cool and zero field cool is comparable to twice the size of moment for the control (Ga,Mn)As sample alone, as shown in Figure 3.4. A clear exchange bias is observed, which affects the entire (Ga,Mn)As layer.

XMCD clearly reveals the presence of a strongly coupled interfacial layer. The thickness of this interfacial layer is estimated to be $\sim 0.9\,nm$, assuming uniform distribution of Mn and the same moment per ion as in the bulk. This is approximately a factor of 3 smaller than the thickness reported by Ref. [49]. This may be due to the different sample preparation methods used. The thickness reported here is comparable in size to the depletion depth for a (Ga,Mn)As layer with carrier

density of $\sim 10^{20}\, cm^{-3}$, which may explain the relatively weak coupling between the interface layer and the bulk (Ga,Mn)As layer.

From sum rules analysis the size of the moment attributable to the interface layer is $0.3\,\mu_B$. The XMCD line shape reveals that the electronic character of this interface layer is largely localised, similar in shape to a d^5 configuration, like Mn in bulk (Ga,Mn)As (see Figure 4.5). This is in contrast to a more metallic environment such as Mn_xFe_{1-x} [49] or MnAs [78]. The strongly coupled interfacial layer persists above room temperature as a small but not negligible effect, however the signal to noise ratio does not permit a meaningful calculation of the size of the room temperature magnetic moment.

Chapter 4

XMCD study of Phosphorus doping in (Ga,Mn)(As,P)

In dilute magnetic semiconductors, such as (Ga,Mn)As, strain largely determines the direction of the magnetic easy axis, in contrast to materials with higher magnetization where shape anisotropy is important. The alteration of the anisotropy by induced strain has been demonstrated using piezoelectric gating [79], growth on strain-relaxed (In,Ga)As buffer layers [80] and by alloying with P [43, 45]. Of the above methods, growing on relaxed (In,Ga)As buffer layers [81] impacts upon the crystal quality, introducing dislocations and pinning sites which affect properties such as T_C and domain wall motion. In contrast, alloying with P produces material with good micromagnetic properties and fewer defects, and by varying the alloy concentration a wide range of strains and hence a variety of magnetocrystalline anisotropy conditions can be achieved. Such materials, with the possibility of perpendicular-to-plane anisotropy, are useful as their magnetisation can be sensitively detected using magneto-optical Kerr microscopy or the anomalous Hall effect [81]. Furthermore a recent theoretical paper by Masek *et al* suggested that co-doping with phosphorus could offer a substantial enhancement in the T_C of (Ga,Mn)As films [46], although other studies predict a rapid drop in T_C with increasing P doping [41].

(Ga,Mn)(As,P) films have already been the subject of much recent investigation into their bulk electrical and magnetic properties [40–45]. In this chapter x-ray magnetic circular dichroism (XMCD) at the Mn $L_{3,2}$ absorption edges is employed to explore the micromagnetic and electronic properties of a series of seven samples of the quaternary magnetic semiconductor $(Ga_{(1-x)}Mn_x)(As_{(1-y)}P_y)$ with

nominal values of $x = 0.06$ and y ranging between 0 and 0.3. This is augmented by XRD and SQUID magnetometry measurements.

4.1 Samples growth

The samples were grown by molecular beam epitaxy (MBE) on a [001] GaAs substrate. The samples were grown with a nominal Mn flux of 6%, and nominal phosphorus concentrations of 0, 3, 6, 9 ,10 ,20 and 30% P (see Table 4.1). These concentrations were estimated from the ion fluxes measured during film growth. As will be shown in Section 4.2 this does not correspond exactly to the incorporated P. For the 10, 20 and 30% P samples a 50 nm buffer layer of low temperature Ga(As,P) was deposited at the relevant P concentration, immediately followed by the 25 nm (Ga,Mn)(As,P) sample layer. For the 3, 6 and 9% P samples the buffer layer was omitted. The Mn containing layers and the buffer layers were both grown at 230 °C. Further growth details are published elsewhere [43,44]. The samples used for the XMCD measurements were subsequently annealed at 190 °C for 48 hours. This is an established method for increasing carrier density, and consequently T_C, by the outdiffusion of compensating interstitial Mn [11].

The typical effect of annealing on the lattice parameter is shown in Figure 4.1. The shift to higher angle of the (Ga,Mn)(As,P) (0 0 4) peak with annealing corresponds to a decrease in vertical lattice parameter. This is due to the removal of interstitial Mn. Since the horizontal lattice constants are matched to the substrate a tensile strain is exerted in-plane which leads to a contraction in the vertical (0 0 1) lattice parameter, as happens for all non-auxetic materials.

For the XMCD measurements, results for annealed samples only are shown. The as-grown samples, particularly for the higher doping concentration, had very low values of T_C and magnetic moment per Mn ion, making the experiment impractical. Table 4.1 lists the samples used along with Curie temperatures for both as-grown and annealed samples, as determined by previously performed SQUID measurements.

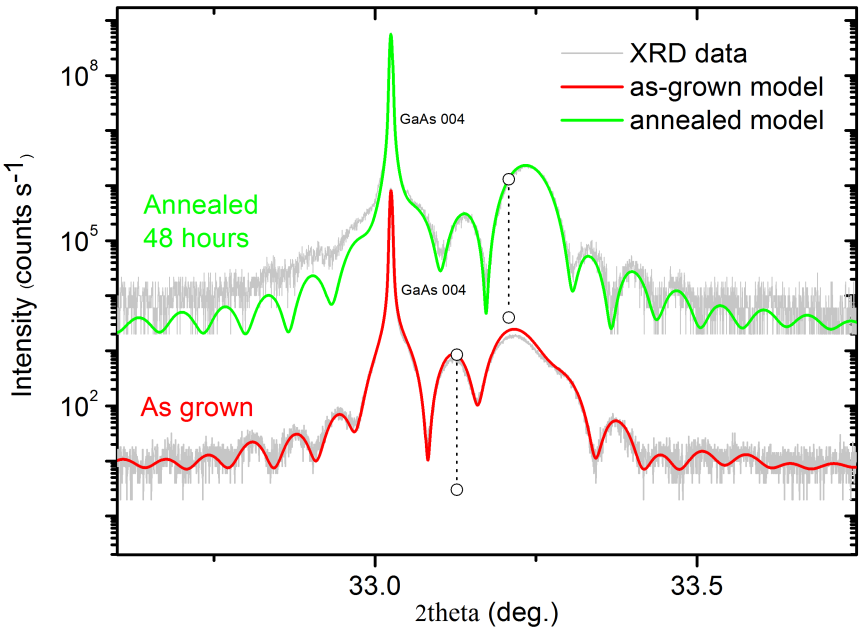

Figure 4.1 – XRD $2\theta\omega$ scans for Mn403 as-grown and annealed. The position of the (Ga,Mn)(As,P) layer peak is marked in both cases by the dotted lines, and shows a shift to smaller vertical lattice parameter with annealing, consistent with the out-diffusion of interstitial Mn

4.2 Determining the strain and Phosphorus concentration

In order to explore the strain present and determine the layer lattice parameters, the samples were examined in a high resolution x-ray diffractometer (XRD). A series of $2\theta\omega$ scans were taken centred around the GaAs (004) diffraction peak using a PANalytical X'Pert Materials Research Diffractometer. Previously performed asymmetric reciprocal space maps (RSM) show the layer to be fully strained and

Sample	nominal P content (%)	T_C for AG (K)	T_C for (μ_B) ann. (K)
Mn499	0	66	137
Mn492	3	61	124
Mn491	6	52	121
Mn498	9	47	108
Mn403	10	32	107
Mn404	20	18	78
Mn405	30	15	75

Table 4.1 – Sample details for 'as-grown' (AG) and annealed (ann) samples

symmetric space maps show there to be sufficiently little tilt so that the $2\theta\omega$ scans approximate q scans, such that regular $2\theta\omega$ line scans around the intense GaAs 004 reflection are sufficient for determining the lattice parameters. These line scans are sensitive to the vertical lattice parameter $(0\,0\,l)$ and enable the determination of this parameter for the separate layers from fitting. The scans were fitted using Philips X'pert Smoothfit software. The fitting procedure uses Vegard's law and the previously determined lattice parameters of the four possible compounds (in Zinc Blende form). During the fitting it is necessary to fix some of the parameters. This is particularly true in this case, because the effects of Mn and P incorporation into GaAs lattice are antagonistic: Mn increases the lattice parameter and P decreases it. This results in an adequate fit not being uniquely defined. Therefore, starting with the as-grown samples, the Mn content was determined and fixed by fitting the control sample, and assuming that in the remaining samples the P incorporation had little effect on that of the Mn. This seems a reasonable assumption since Mn and P are not competing for the same lattice sites. This is corroborated by a comparison of total moment determined using the XMCD sum rules against SQUID measurements of the magnetisation, which give the same values, within error, for the low P concentration samples (Mn 499, Mn491, Mn492)(see Section 4.3). Since the sum rules analysis gives the average magnetic moment per Mn ion and the SQUID measurement gives the total magnetisation, this indicates that the same percentage of Mn has been incorporated into the lattice independent of the P concentration. For the annealed samples the P concentrations, as determined from the as-grown samples, were fixed and the Mn concentration allowed to vary. This assumption was based on the fact that interstitial Mn is known to be mobile at these temperature, whereas there is no reason to assume that P will be, added to which the increasing tensile strain, seen in both the XRD and indirectly via the change in anisotropy, upon annealing is consistent with the outdiffusion of Mn alone.

The model fitting returns the concentration of both P and Mn in the sample, along with the layer thickness. The concentrations are calculated based on the aforementioned use of Vegard's law combined with the predetermined compound lattice parameters. Hence, it is then possible to extract the relaxed lattice parameters using Vegard's law:

Vegard's law for $Ga_{1-x}Mn_xAs$ takes the form:

$$a_{rel} = a_1 x + (1 - x)a_2 \tag{4.1}$$

where a_{rel} represents the relaxed lattice parameter of the ternary compound ((Ga,Mn)As), and a_1 and a_2 are the lattice parameters of the two compounds

Sample	nominal P content (%)	model P (±0.05) content(%)	strain for AG (K)	strain for ann. (K)	total magnetic moment at 2 K(μ_B)
Mn499	0	0	-0.63	-0.38	4.05
Mn492	3	5.5	-0.25	0.01	4.07
Mn491	6	5.9	-0.22	0.06	4.49
Mn498	9	9.2	0.00	0.30	3.94
Mn403	10	12.43	0.28	0.51	3.81
Mn404	20	27.62	1.32	1.54	2.69
Mn405	30	31.5	1.58	1.81	2.62

Table 4.2 – Sample details showing nominal P content and P content derived from modelling of the XRD data. The strain, calculated using Vegard's law and Poission's ratio, is also shown.

given by the extremes of x, in this case GaAs and MnAs.

Vegard's law for $Ga_{1-x}Mn_xAs_{1-y}P_y$ takes the form:

$$a_{rel} = xya_1 + (1-x)ya_2 + x(1-y)a_3 + (1-x)(1-y)a_4 \tag{4.2}$$

where a_1, a_2, a_3 and a_4 are the lattice parameters of MnP, GaP, MnAs and GaAs respectively.

Once the relaxed lattice parameter is found Poisson's ratio can be used to calculate the strained lattice constant using:

$$a_\perp = \frac{1+\nu}{1-\nu}(a_{rel} - a_0) \tag{4.3}$$

where $a_\perp$ is the strained vertical lattice parameter, ν is Poisson's ratio (for $GaAs = 0.311$), a_{rel} is the relaxed lattice constant calculated from Vegard's law, and a_0 is the substrate lattice constant. It has been assumed that the doping concentrations are sufficiently low such that the GaAs value of Poisson's ratio can be used for both (Ga,Mn)As and (Ga,Mn)(As,P). These values were then used to calculate the strain for each sample, as defined by $strain = \frac{(a_\perp - a_0)}{a_0} \times 100$. The values of strain are shown in Table 4.2.

The XRD experimental data along with model fitting and estimated peak position is shown for the as-grown samples in Figure 4.2, and for the annealed samples in Figure 4.3. The estimated peak positions were found using Bragg's law with the strained lattice parameter calculated from Equation 4.3, as such it does not account for small changes which can be produced by thin film effects, but gives a good approximation of the sample peak position.

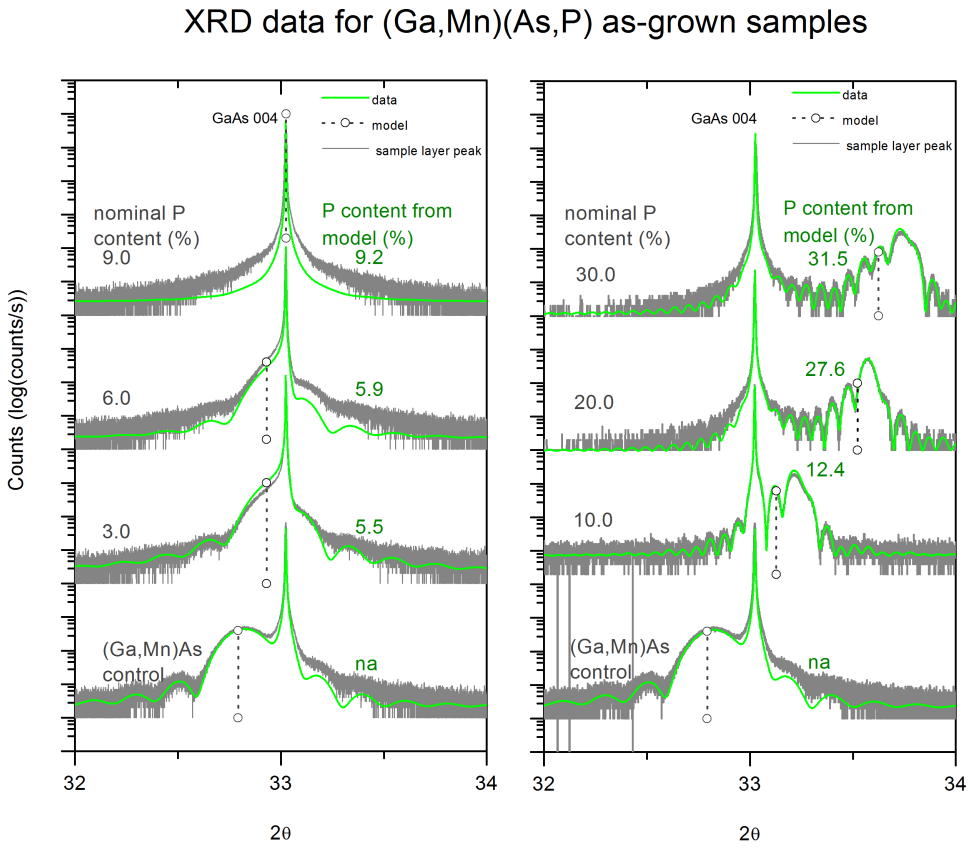

Figure 4.2 – $2\theta\omega$ scans around the GaAs 004 peak for all samples in their as-grown condition

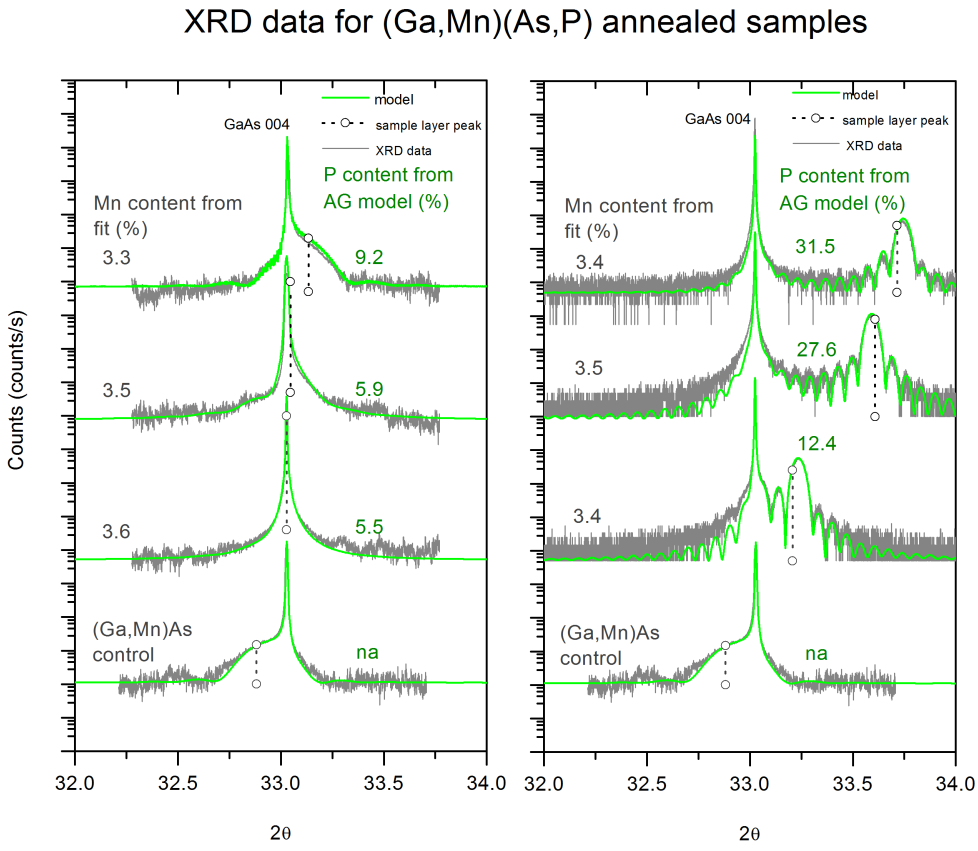

Figure 4.3 – $2\theta\omega$ scans around the GaAs 004 peak for all samples after 48 hours annealing at 180 °C

4.3 XMCD results

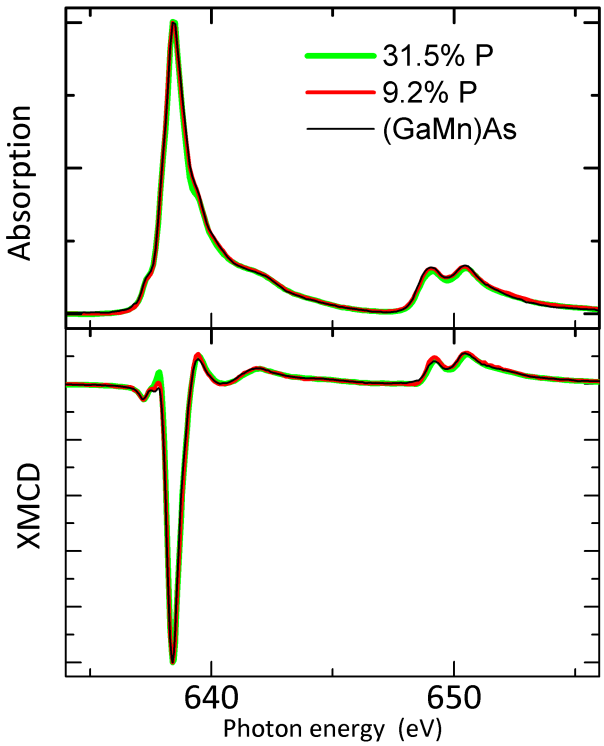

Figure 4.4 – Representative normalised XAS and XMCD spectra for (Ga,Mn)As and (Ga,Mn)(As,P) films, taken at normal incidence.

The magnetic properties of the samples were examined using XMCD on beamline 4.0.2 of the Advanced Light Source, Berkeley. This beamline is equipped with an octupole magnet capable of generating a magnetic field vector in any direction, of up to ∼0.8 T. Immediately prior to mounting, the samples were etched using concentrated HCl to remove surface oxides [82]. During the measurements the samples were kept at a constant temperature of 15 K. The XA spectra were taken using total electron yield mode. The XMCD was generated by flipping the field at each point between parallel to beam and antiparallel. The scan was then repeated with opposite helicity and the two averaged to remove spurious equipment-related artifacts. The measurements for all samples were taken in two distinct geometries. The first was with both beam and field lying along the surface normal and the second was with beam and field making an angle of 30° to the sample surface.

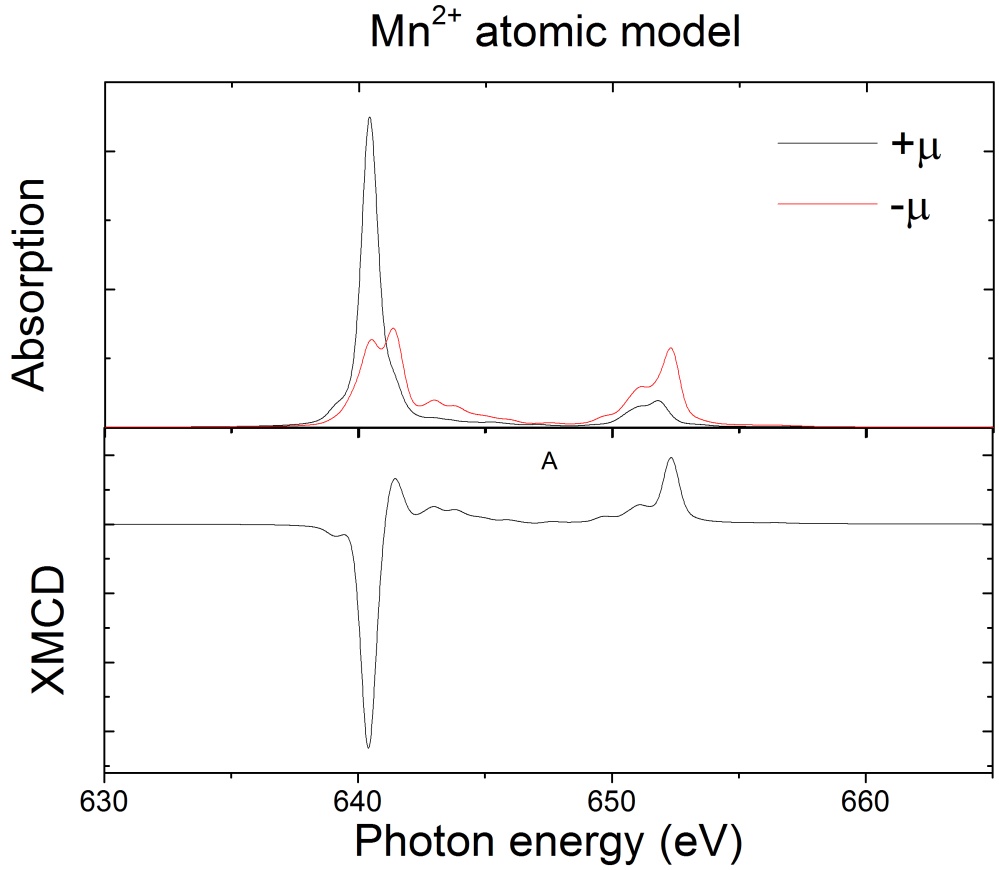

Figure 4.5 – model Mn d^5 spectra created using the multiplet software CTM4XAS [64]. The top panel shows the polarisation dependent XAS, and the bottom panel shows the XMCD.

Only results for the annealed samples are discussed here. The as-grown samples have T_C's not much greater than the measurement temperature, which resulted in low signal to noise ratios.

Figure 4.4 show representative XAS and XMCD plots. The plots have been scaled to unity at the L_3 absorption edge to better enable comparisons of shape. The spectra for all samples are nearly identical to those observed previously for both (Ga,Mn)As [67, 82] and (Ga,Mn)P [83], indicating a d^5-like hybridized electronic configuration in tetrahedral crystal field symmetry. To support this Figure 4.5 shows a simulated XA spectra for a Mn^{2+} ion in a tetrahedral crystal field of 0.5 eV, and reproduces well the main features. The simulation was produced using the atomic multiplet theory software CTM4XAS [64].

Figure 4.6 shows all of the XMCD traces scaled to unity at the L_3, and the insets display the two regions labelled as "b" and "c". These features display cubic

symmetry with relation to angle of incidence as shown by Edmonds *et al* [84].

Figure 4.7 shows the prepeak region, labelled "a" in Figure 4.6, in more detail for all of the samples. Edmonds *et al* have shown this feature to be a sensitive indicator of strain, with rotation from grazing to normal incidence producing a decrease for compressively strained materials and an increase for those under tensile strain [84, 85]. A clear dependence on strain is seen on the size of this feature for

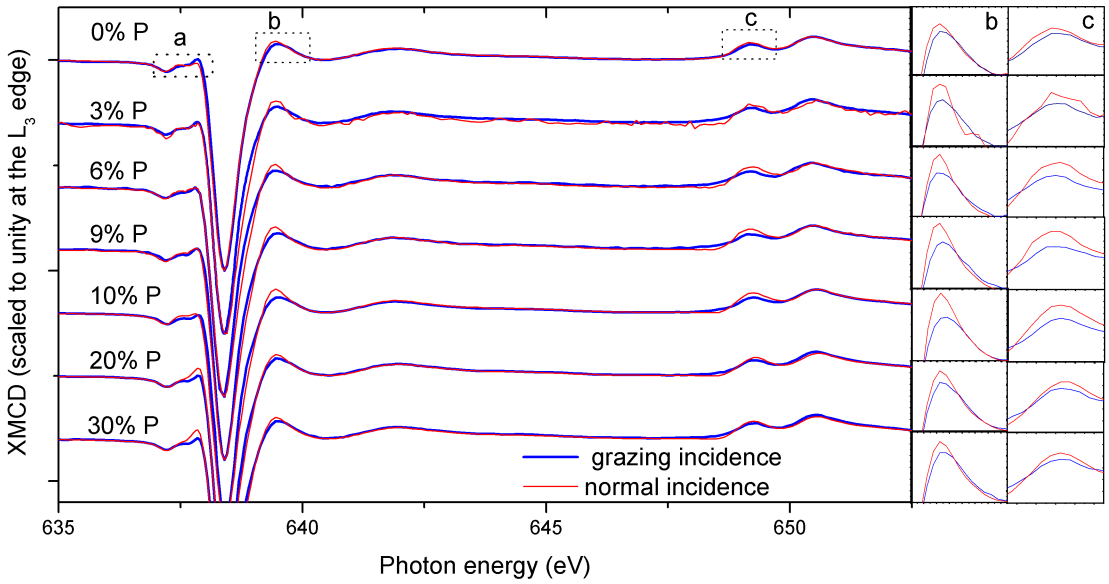

Figure 4.6 – Comparison of XMCD line shape for all of the annealed samples. The XMCD spectra have been normalised to unity at the L_3 edge. The red line shows measurements taken at right angles to the plane and the blue line is measurements taken at 30° grazing incidence. The features labelled "b" and "c" are highlighted in the right insets, and the features labelled "a" are highlighted in Figure 4.7

the perpendicular spectra, whereas the grazing incidence spectra remain relatively unaffected. For axial symmetry with parallel beam and magnetic field vectors the angular dependence of XMCD can be written as $I_{XMCD} = I_0 + \frac{1}{2}I_2(3cos^2\theta - 1)$, where I_0 is the isotropic part and I_2 is the anisotropic component [86]. Since the term containing I_2 vanishes at $\theta = 54.7°$ it will be small at $\theta = 60°$ (or 30° from the surface since θ is measured from the surface normal). This is consistent with the present results and accounts for the lack of variation with strain of the grazing incidence XMCD at the prepeak. Furthermore the prepeak height depends on the carrier density i.e. the density of states at the Fermi level. The lack of variation in the prepeak XMCD in grazing geometry suggests that the local density of states

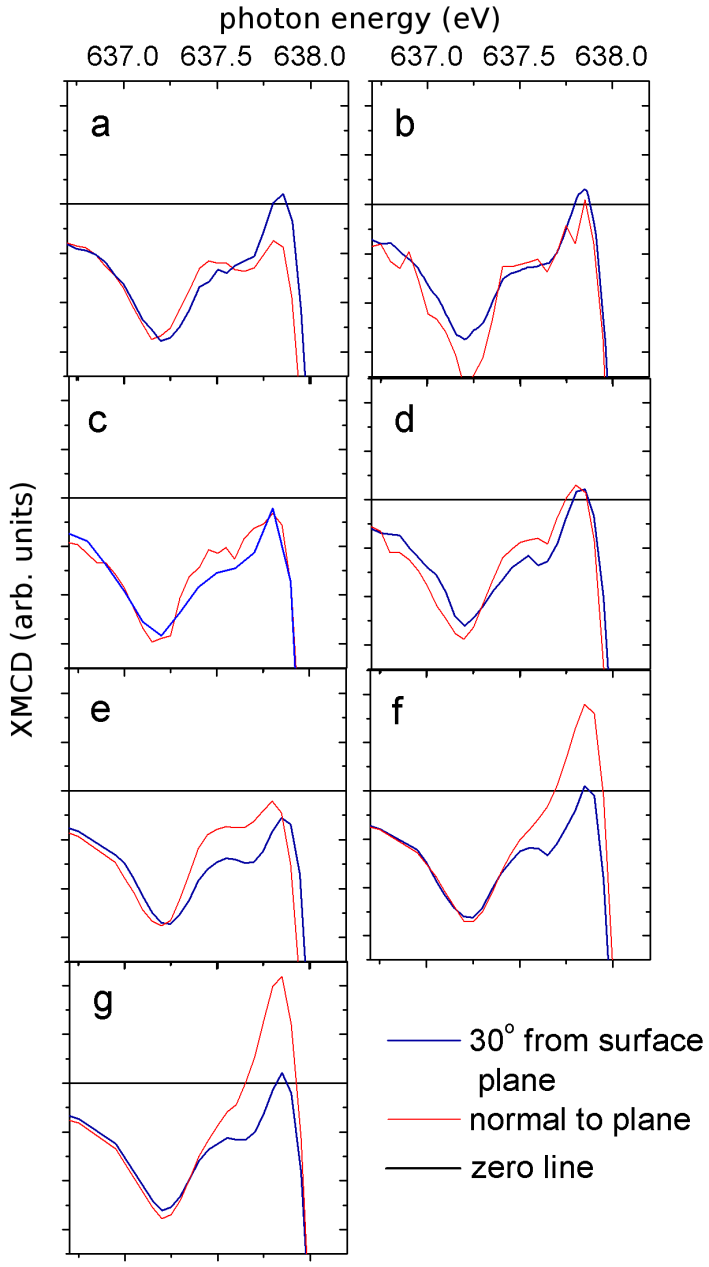

Figure 4.7 – Expanded view of the XMCD prepeak region from Figure 4.6 with panels a-g going in order of increasing P content (nominally 0, 3, 6, 9, 10, 20 and 30%)

around the Mn 3d does not vary significantly for all samples studied. The difference between grazing and normal incidence of the XMCD intensity at the prepeak is plotted against strain in Figure 4.8. A clearly linear trend is observed which demonstrates this uniaxial feature reported by Edmonds *et al* [84] is not only a sensitive indicator of strain but also a sensitive measure of the strain present in this system.

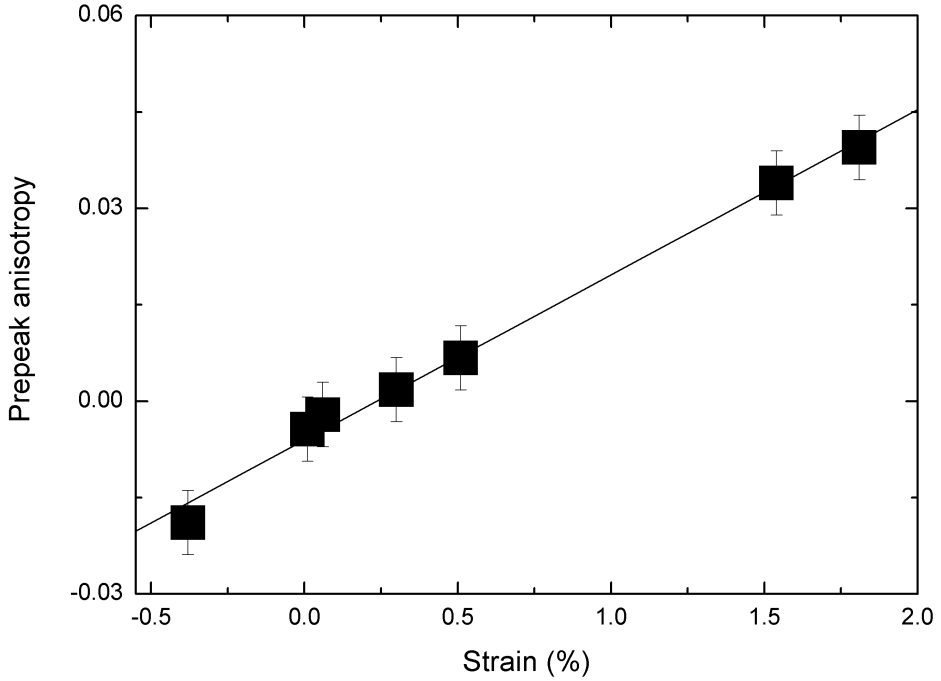

Figure 4.8 – XMCD prepeak anisotropy, defined as the difference in XMCD intensity between normal incidence and 30° incidence, versus strain in the studied samples.

Another clear result of the P doping is seen in Figure 4.9. These hysteresis loops were generated by plotting the asymmetry of the XMCD peak against the applied field, and therefore give a measure of the projection of the magnetisation along the field direction (the field is applied parallel to the x-ray beam direction). A clear decrease with increasing P doping of the strength of the in-plane anisotropy is seen. (Ga,Mn)As has its hard axis out of plane and easy axis in-plane owing to the compressive strain. By 9% nominal P content the easy axis is out of plane, and with further P doping the in-plane direction becomes increasingly hard.

In order to extract quantitative information from the XMCD data sum rules analysis was applied, using the same techniques employed by Chen *et al* [62], to ascertain the average magnetic moment per absorbing atom. A $3d$ electron count of 5.1 was used along with a correction factor of 1.47 for the spin magnet moment, which is used to compensate for the mixing of the $2p_{3/2}$ and $2p_{1/2}$ levels. This number was determined by the application of the sum rules to a model Mn d^5 system with a well defined ground state using atomic multiplet theory [67](as described in Section 2.4.3). For each sample in each orientation a hysteresis loop was first performed to determine the strength of the magnetic anisotropy. The strength of the applied magnetic field was then chosen so as to fully saturate the

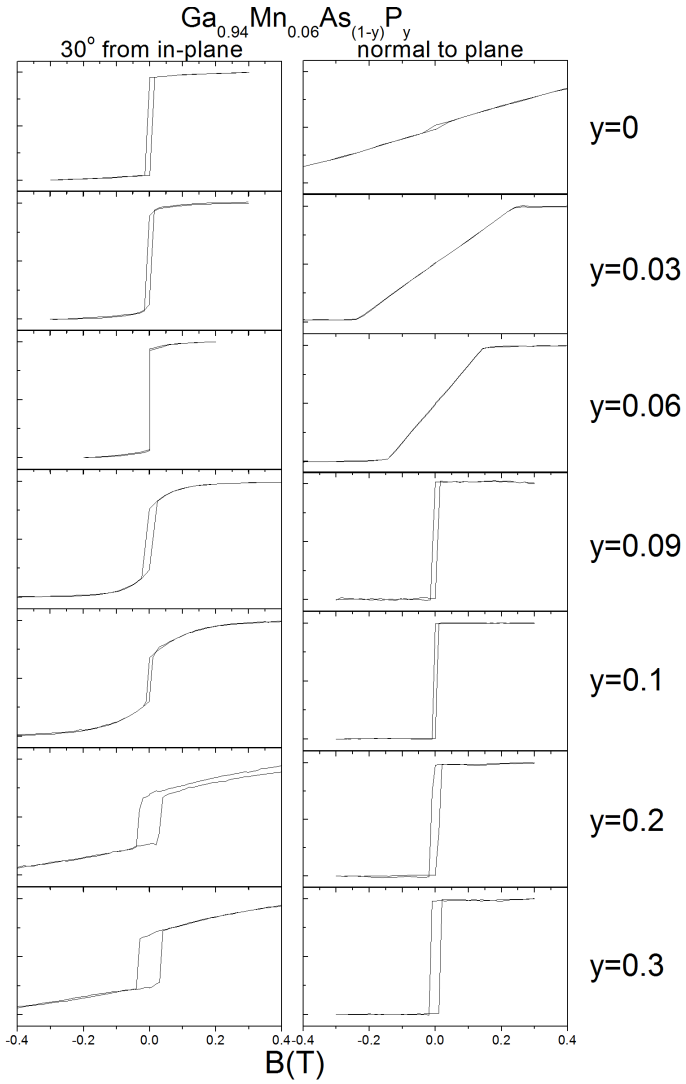

Figure 4.9 – XMCD hysteresis loops for all annealed samples generated using the Mn L_3 absorption edge at 15 K

magnetisation along the field direction. The magnetic moment values measured by XMCD were then adjusted using SQUID magnetization results to obtain the 2 K value of the moment. This was done by multiplying the sum rules result by the factor $M(2\,K)/M(15\,K)$, where M(T) is the magnetization as a function of temperature as measured by SQUID magnetometry. The sum rules calculated moments along with strain are displayed in Table 4.2. Figure 4.10 shows the total magnetic moment per Mn ion for each of the annealed samples against nominal P content. At low concentrations the incorporated P has no effect within error, but at concentrations of $\sim 10\%$ or above there is a marked decrease in the total moment. Since the lineshape of the XMCD does not change appreciably between samples, it is inferred here that the local magnetic moment of the Mn ions is also unchanged. This leads to the conclusion that less of the Mn must be participating in the ferromagnetic order for the samples with higher P doping. A similar trend

is seen in T_C, which is also shown in Figure 4.10.

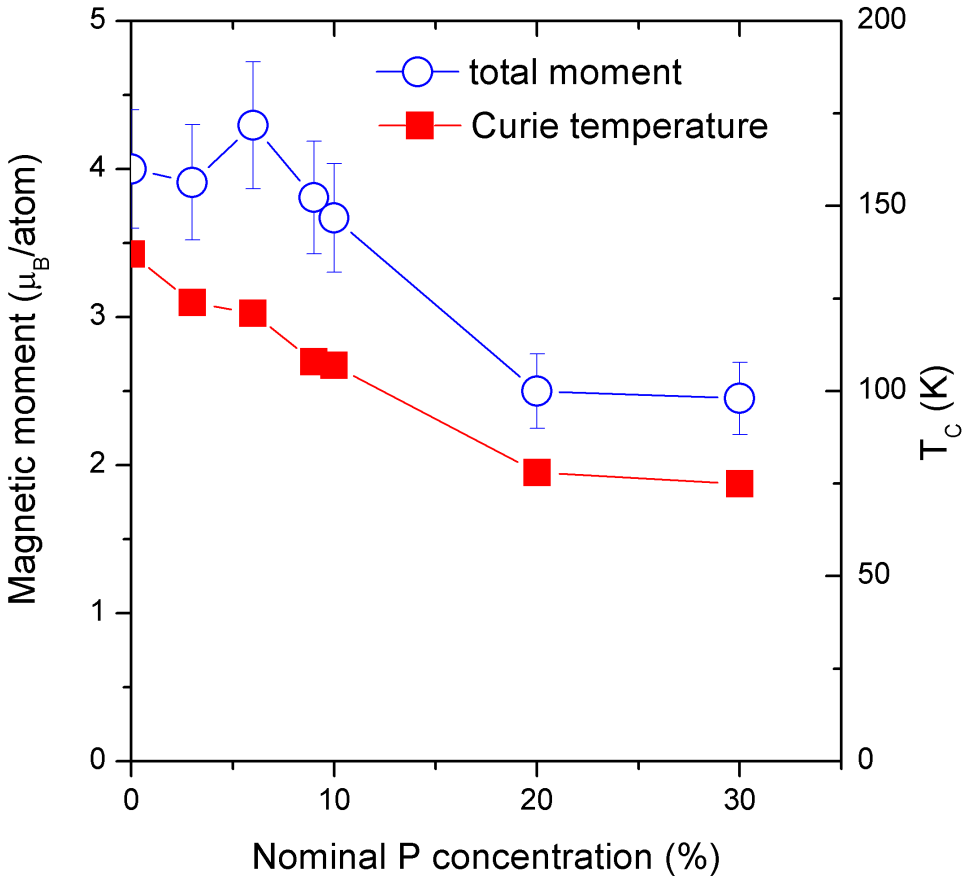

Figure 4.10 – Total moment and Curie temperature dependence on phosphorus concentration. Curie temperature was determined using the SQUID in remnance along each samples easiest axis. Total moment was determined from XMCD.

4.4 Conclusions and discussion

The introduction of P into (Ga,Mn)As did not lead to improvements in T_C as predicted by Masek *et al* [46], but neither did it produce the rapid drop seen by Stone *et al* [41]. It is interesting to note that a qualitatively similar trend was observed by Rushforth *et al* in $Al_yGa_{1-y}Mn_xAs$, indicating that the same processes are likely to be responsible in both cases [43] (see Figure 4.11). Rushforth *et al* cite several mechanisms which are responsible for the observed effects. An increased tendency for interstitial Mn, which have been shown to act as double donors as well as as reducing magnetic participation by bonding antiferromagnet-

ically to substitutional Mn, leads to reduced carrier density and moment [87–89]. Another possibility is that the wide bandgap of GaP leads to less mobile carriers and subsequently weaker exchange coupling between Mn ions, which could result in partial disordering of the moment distribution as seen in other wide bandgap materials [90, 91]. The similarity of all the XMCD lineshapes precludes the possibility of significantly more localised Mn 3d states, but XMCD at the $L_{3,2}$ edge does not directly probe the states with 4p character, so increased localisation of these carriers is a possibility. A similar process was suggested by K edge XMCD measurements of (Ga,Mn)As films with low Mn doping [92](This is discussed in Chapter 5).

Despite the drop in T_C and magnetisation the (Ga,Mn)(As,P) samples have high crystalline quality over a wide range of doping. The magnetic anisotropy is shown to vary from strongly in-plane to perpendicular-to-plane within the range of P doping studied, which means that (Ga,Mn)(As,P) provides a high crystal quality DMS, with relatively high T_C and tunable anisotropy.

The XMCD prepeak uniaxial feature is shown to be a highly sensitive indicator of strain in this system (this has already been demonstrated for (Ga,Mn)As [84]), which scales linearly with the change in strain given by high resolution XRD. This demonstrates the utility of XMCD as a highly sensitive simultaneous probe of micromagnetic and strain properties of magnetic thin films.

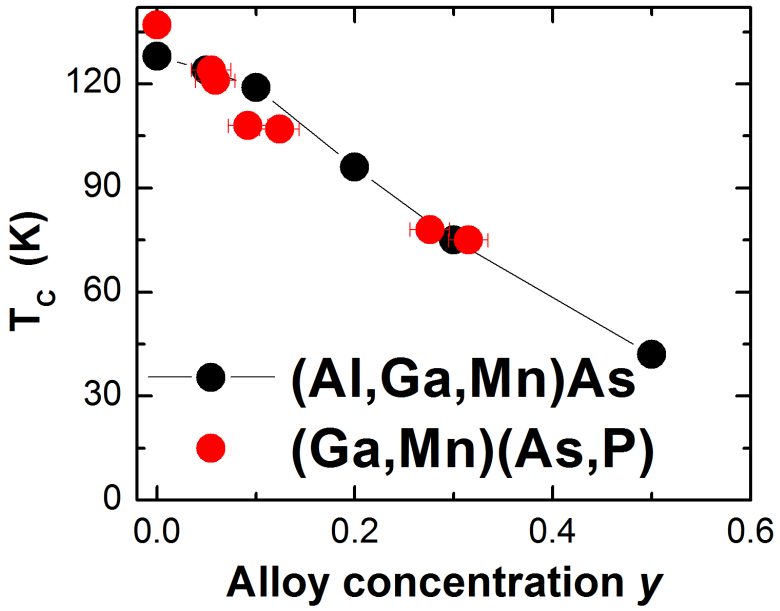

Figure 4.11 – (a) Curie temperature versus doping fraction for a set of $Al_yGa_{1-y-x}Mn_xAs$ samples and the $Ga_{1-x}Mn_xAs_{1-y}P_y$ samples studied herein. (Al,Ga,Mn)As data reproduced from a paper by Rushforth *et al* [43].

Chapter 5

Orbital polarisation studies of (III,Mn)As semiconductors using K-edge x-ray magnetic circular dichroism

The precise character of the holes which mediate the ferromagnetism in (III,Mn)As semiconductors is a matter of continuing debate. Depending on the level of doping, these materials can be semi-insulating or metallic in conductivity, with the metal-insulator transition usually occurring around $\sim 2\%$ Mn doping. In the metallic regime the electrical and magnetic properties can be reproduced reasonably well by models which have the holes occupying the spin-split valence band. In the insulating regime the magnetism and conduction are more often described by models which utilize hopping in a narrow impurity band, detached from the host valence band. However, other studies have described both regimes using an impurity band model [22,23] and some even refute the magnetic nature of the (Ga,Mn)As valence band altogether [52].

Techniques based on magnetic circular dichroism have been extensively used to study the electronic structure of these materials. Many of these studies have been conducted at the optical or infrared wavelengths, where transitions between the valence, impurity and conduction bands are excited. The interpretation of these results are difficult, owing to the complex nature of the inter- and intra-band transitions. This means that the results are often ambiguous, and agreement with both impurity and valence band models have been reported.

In this chapter XMCD at the As and Mn K-edge is used to directly probe the unoccupied valence states in the vicinity of the Fermi energy. Unlike the L absorption edges, the K edge can be more simply interpreted in terms of the one-particle density of states accessible from the $1s$ level [93]. This is because the core $1s$ state and valence $4p$ states are well screened from each other, which precludes more complex interactions, such as *multiplet effects*.

5.1 Sample preparation and characterisation

The (Ga,Mn)As and (In,Ga,Mn)(As) samples used in the study were grown using molecular beam epitaxy (MBE) with the layer structure shown in Table 5.1. The percentage values are based on Mn/Ga flux ratios, and are expected to overestimate the actual amount of Mn incorporated substitutionally, because some Mn will be incorporated in interstitial positions, or to a lesser extent on random sites. For those sample which were annealed, the procedure was to anneal in air at 190°C for several hours. This is an established procedure for removing interstitial Mn via out diffusion. Since the attenuation depth of x-rays around the As K edge is several microns, in order to prevent the substrate from dominating the absorption signal, the (Ga,Mn)As films grown on GaAs substrate were attached face-down onto an $Al_2O_3(0001)$ wafer using photoresist, and the GaAs substrate was removed by etching away a 100-200 nm thick AlAs buffer layer using concentrated hydrofluoric acid. Characterisation was done using SQUID magnetometry, x-ray diffraction and electrical transport measurements.

Sample	Composition	x(%)	y(%)	Annealed	T_C (K)	M_S (emu/cm^2)
Mn586	1500 nm GaMnAs GaAs substrate	1	0	no	11	5
Mn566a	200 nm GaMnAs 200 nm AlAs GaAs substrate	5	0	yes	101	37
Mn182	1000 nm GaMnAs 100 nm AlAs GaAs substrate	2	0	no	30	9
Mn183	1000 nm GaMnAs 100 nm AlAs GaAs substrate	5	0	no	50	26
Mn454	200 nm InGaMnAs 50 nm InGaAs InP substrate	8	40 40	yes	62	29
Mn455	140 nm InGaMnAs 50 nm InGaAs InP substrate	8	60 60	yes	68	35

Table 5.1 – Sample details for $(In_y, Ga_{1-y}, Mn_x)As$ and $Ga_{1-x}Mn_xAs$ samples studied

5.1.1 XRD characterisation

X-ray diffraction(XRD) line scans were performed on the layers to ascertain their crystal structures using a PANalytical x'Pert materials research diffractometer. $2\theta\omega$ scans were taken around the bright GaAs 004 and InP 004 reflections. Figure 5.1 shows a selection of line scans for some of the samples, along with models created using PANalytical X'pert smoothfit software and the layer structures shown in Table 5.1. For the (Ga,Mn)As samples the clearly visible layer peak is evidence of the presence of a single crystal layer. The position of the layer peaks at lower angles than the substrate shows that the layer lattice parameters are larger, and is indicative of compressive strain. The (In,Ga,Mn)(As) sample shows broader merged sample and buffer layer. Modelling of this line scan reveals that both sample and buffer layer are weaker, and broader than expected. This is most likely evidence of gradual relaxation. For layers of this thickness it often the case that the layer is not fully strained and simply relaxes through dislocations or other defects if strain is present. Further evidence of this is seen in Figure 5.2 which shows an asymmetric RSM for sample Mn454. The relative positions of the peaks indicates a fully relaxed sample layer, as the peaks lie close to the diagonal line in q space meaning they do not share the same in-plane lattice parameters. If the sample was fully strained then the peaks would lie along a line of constant q_x (i.e. they would posses the same in-plane lattice parameters).

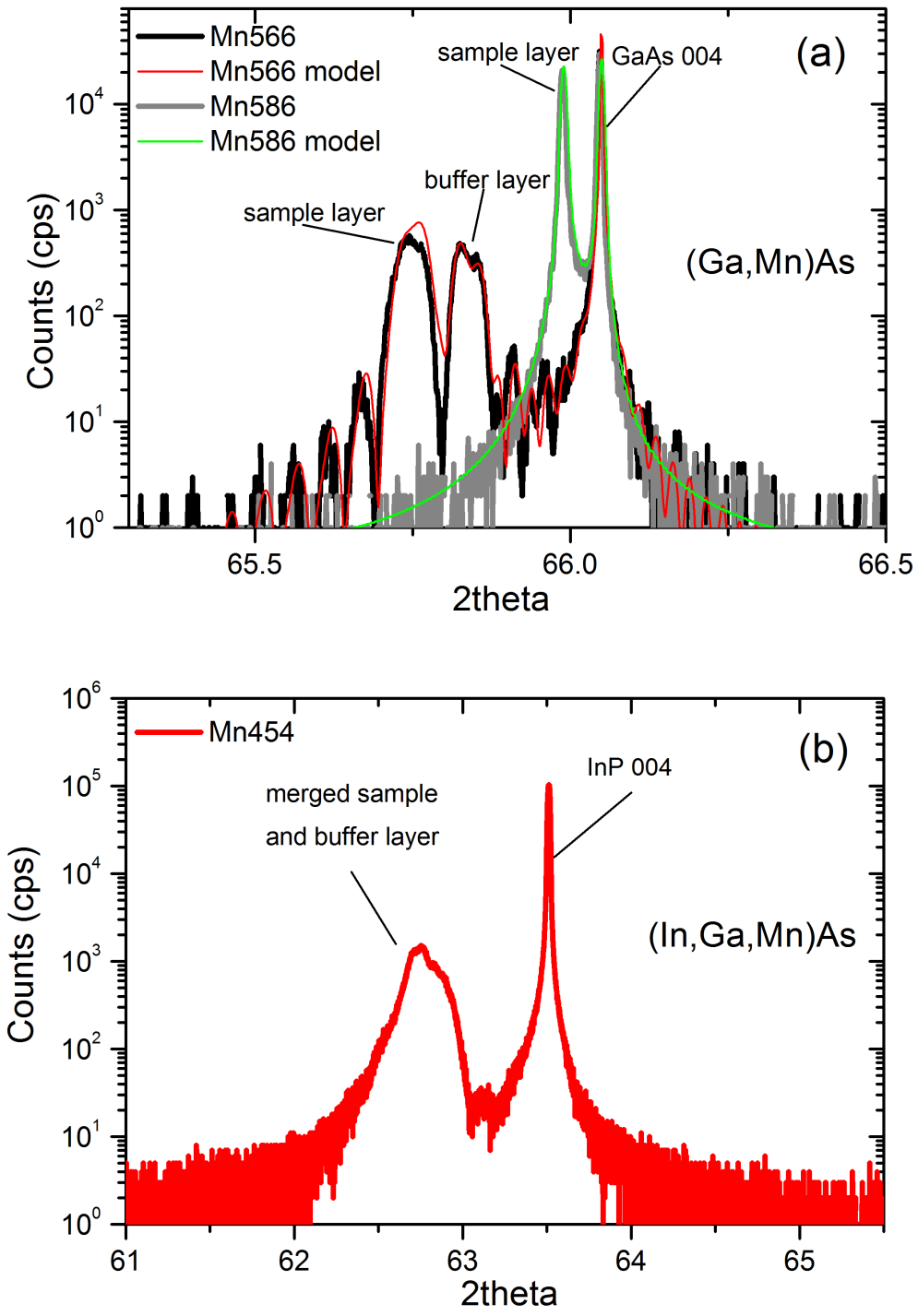

Figure 5.1 – (a) $2\theta\omega$ line scans for the (Ga,Mn)As samples Mn566 and Mn586, centred around the GaAs $(0\,0\,4)$ with accompanying model data. (b) line scans for the (In,Ga,Mn)(As) sample Mn455 which displays a high degree of relaxation and is harder to model.

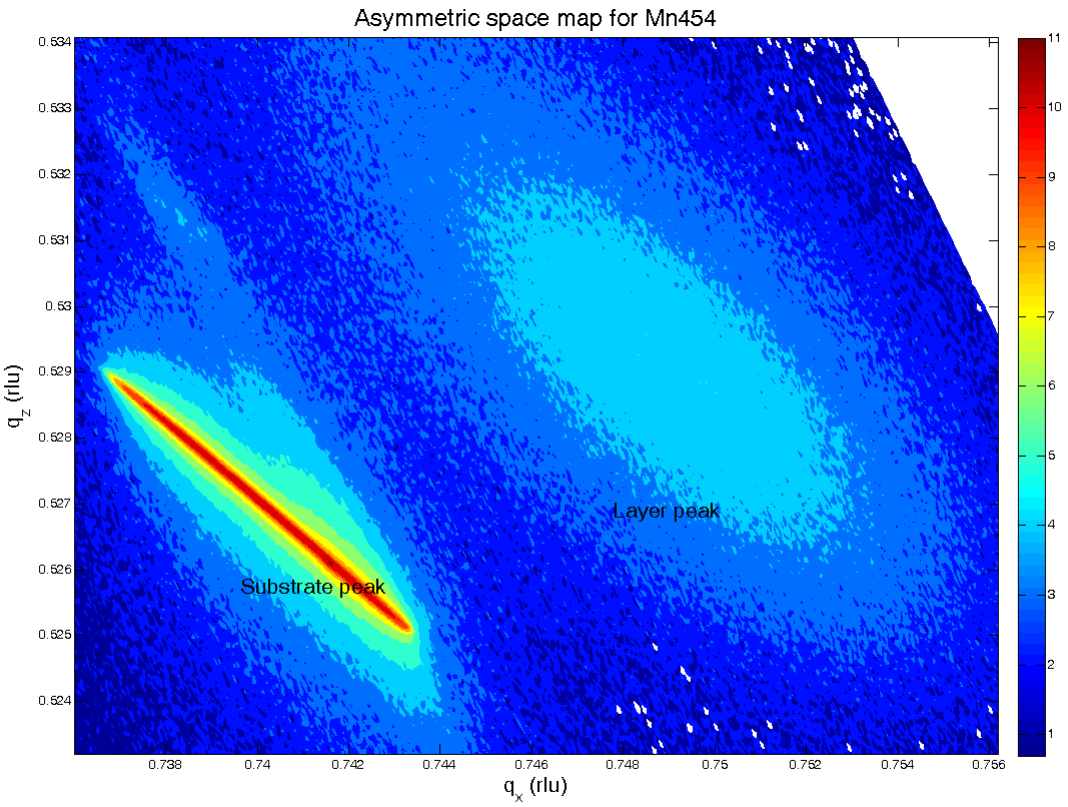

Figure 5.2 – Reciprocal space map for Mn454, centred around the InP 444 reflection. The colour bar represents $\log_{10}$ of the counts per second.

5.1.2 Resistivity measurements

Figure 5.3 shows the resistivity versus temperature curves for all samples used. In agreement with previous studies [94] the films are insulating in behaviour for the low doped (Mn182, Mn586) and highly compensated samples and metallic in the more highly doped and annealed samples (Mn454, Mn455 and Mn566a). This metal insulator transition occurs somewhere between the 1% and 2% doped samples. A clear correlation is seen between the conductivity and the T_C of the samples, with the more conductive samples having higher T_C and total moment. The T_C coincides approximately to a shoulder on the ρ vs T curves, and can be seen more clearly by looking at the $d\rho/dT$ curves shown in Figure 5.4 [95].

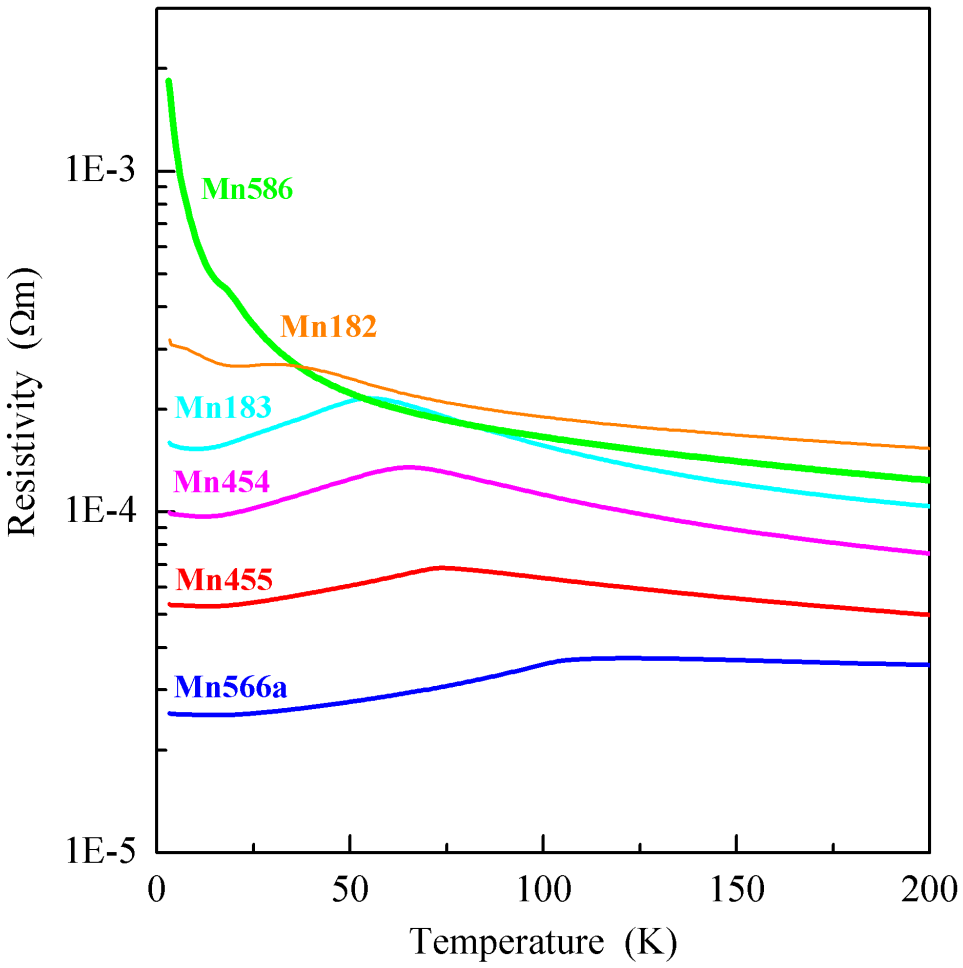

Figure 5.3 – Resistivity versus temperature curves for the samples listed in Table 5.1

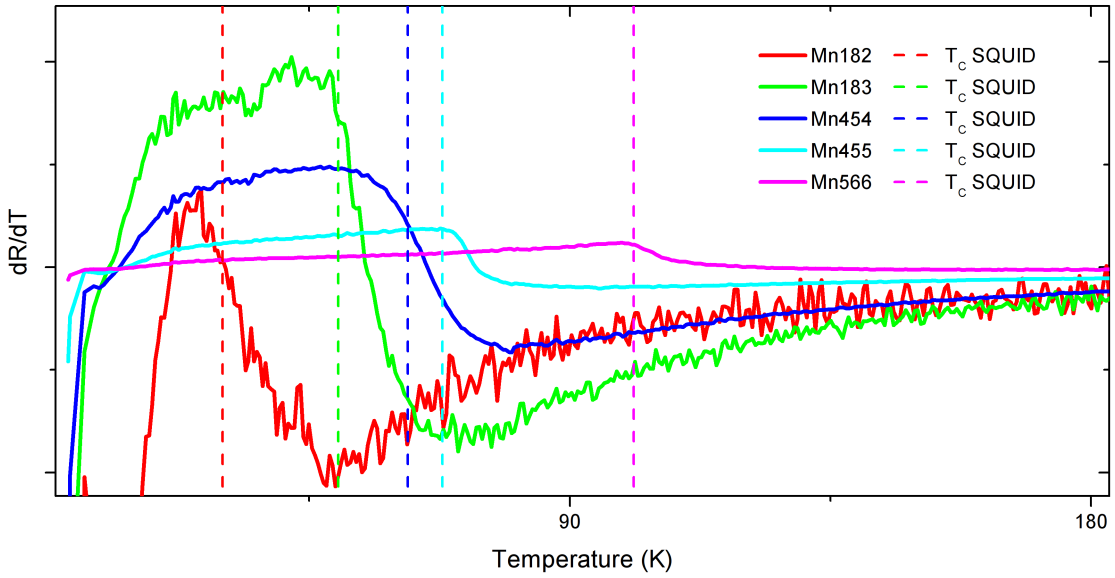

Figure 5.4 – The first derivative of the resistivity versus temperature curves for the samples listed in Table 5.1, with the vertical dashed line showing the SQUID determined value of T_C for the relevant sample.

5.1.3 Magnetic anisotropy data

Figure 5.5 shows the ratio of remanence to saturation magnetization for some of the studied samples, as a function of temperature and magnetic field. For the lowest concentration sample Mn586, square hysteresis loops and remanence to saturation ratio close to 1 are observed along the growth direction [001], showing that the magnetization lies perpendicular to the plane for this sample. In contrast, for the highly doped and annealed sample Mn566a, the easy axis lies in the plane of the film. The 2% doped sample Mn182 shows a crossover between the two regimes, with a large out-of-plane remanence at low temperatures and an in-plane magnetic easy axis at temperatures close to T_C. Similar crossover behaviour of the magnetic anisotropy in (Ga,Mn)As has been reported previously by Sawicki *et al* [96].

As well as initial use of SQUID magnetometry to characterise the T_C and magnetic anisotropy of the samples post-growth, magnetometry was also used to check that samples were not significantly changed by the preparation for the K edge XMCD. The preparation, as discussed in Section 5.1, involved the removal of the substrate by etching. This left a fragile and distorted free-standing layer. SQUID measurements were performed on the etched films to ensure that this procedure did not significantly affect the magnetic properties of the films. Magnetometry

measurements for Mn182 and Mn183, before and after etching, are shown in Figure 5.6. This shows that the layer remains relatively unaffected by the etching process.

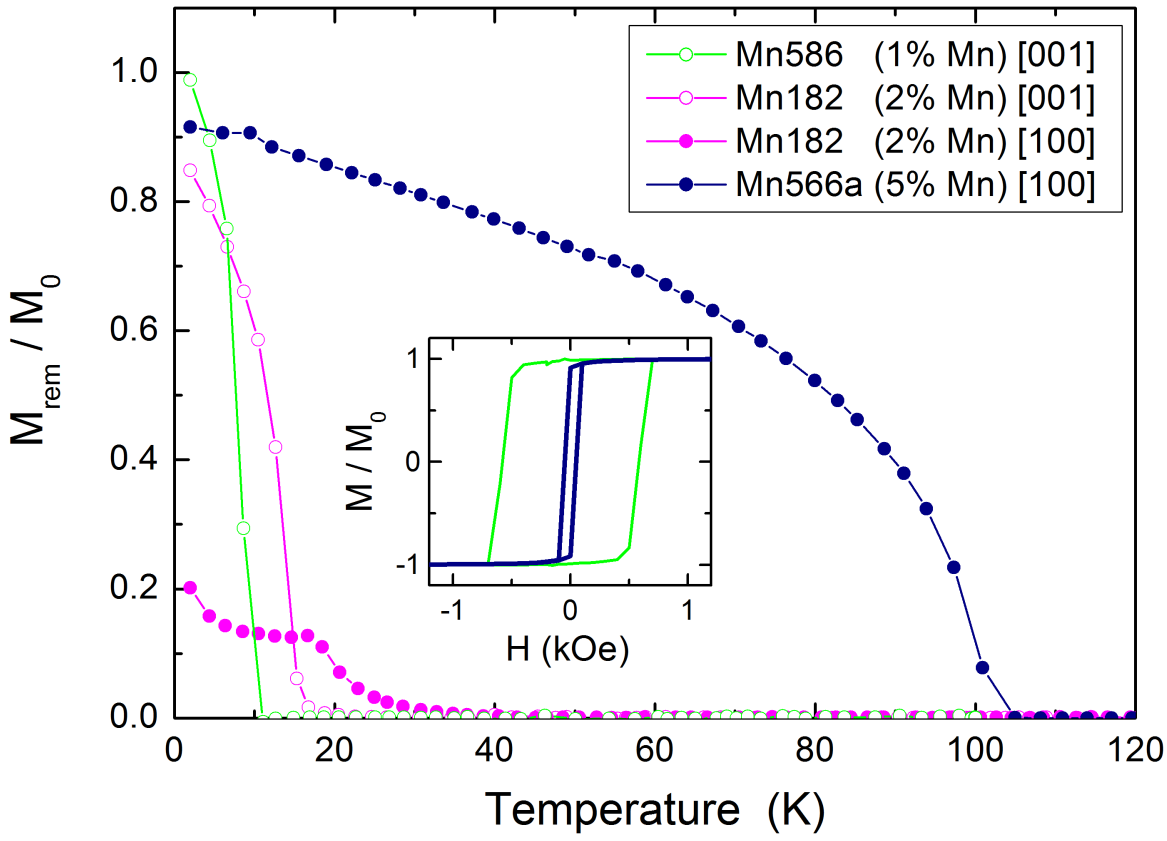

Figure 5.5 – Magnetisation at remnance versus temperature. (inset) Shows the magnetic hysteresis for the lowest and most highly doped sample.

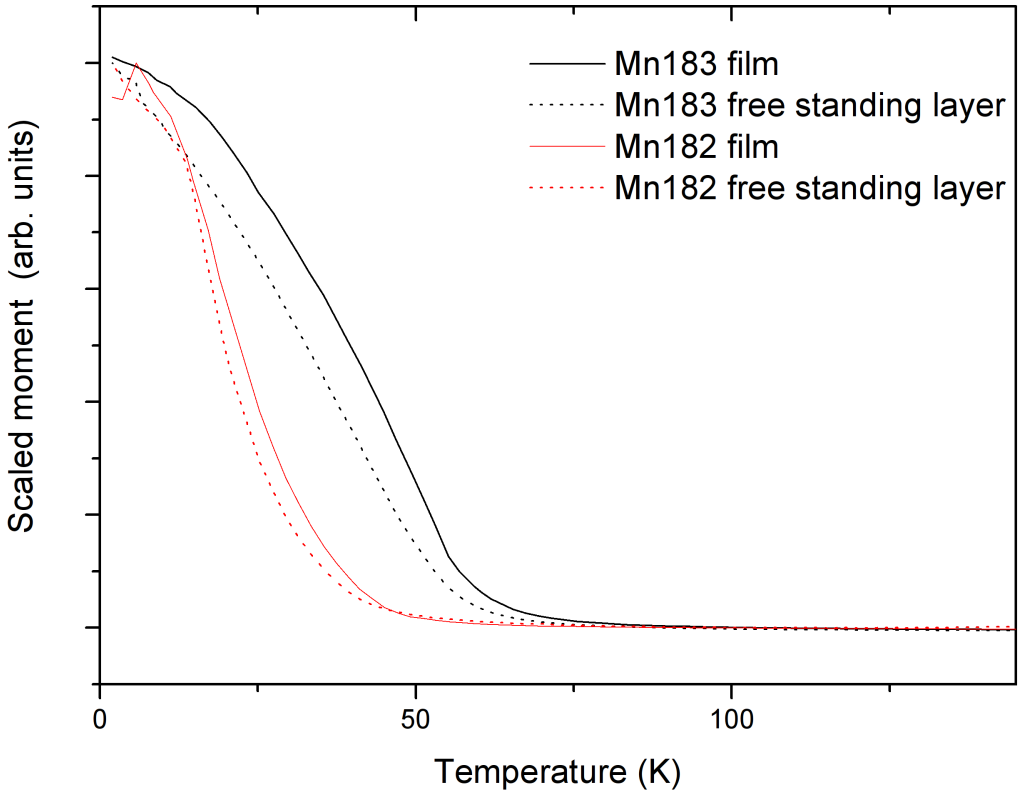

Figure 5.6 – Field cool measurements for samples Mn182 and Mn183 before and after etching with 1000 Oe field applied along the [0 0 1] direction.

5.2 K edge XMCD

The x-ray absorption and XMCD measurements were performed using 98% circularly polarized x-rays on beamline ID12 of the European Synchrotron Radiation Facility. Mn and As K edge measurements were performed on (Ga,Mn)As samples, excepting As K edge measurements on Mn586, and As K edge measurements were performed on the (In,Ga,Mn)(As) samples. All of the absorption spectra were recorded in total fluorescence yield mode, for either normal or grazing (15°) incidence of the x-ray beam. The XMCD signal was obtained from the difference in absorption for parallel and antiparallel alignments of the x-ray polarization vector with respect to an external magnetic field of up to 6 T, applied along the beam direction. Measurements, taken over several hours, were averaged in order to improve the signal-to-noise ratio. To avoid experimental artifacts, the x-ray helicity and the external magnetic field direction were alternately flipped. The XMCD signals are given as a percentage of the absorption edge jump. The size of the

calculated sum rules moments for the samples grown on InP with InGaAs buffer layers were corrected for the extra As absorption by the non-magnetic buffer layer.

5.2.1 XMCD at the As K absorption edge

The As K edge absorption and XMCD spectra are shown in Figure 5.7. The absorption spectra are similar to those previously reported for GaAs [97], with no significant differences in the near-edge part of spectra observed between the (Ga,Mn)As and (In,Ga,Mn)As samples. The XMCD manifests itself as a sharp Lorentzian-like peak which coincides with the onset of the As K absorption edge. The sign of the XMCD and its lineshape are consistent with previous observations [53]. However, its magnitude is strongly sample-dependent: in the most conductive sample (Mn566a), it is around a factor of 3 larger than previously observed [53], while in the insulating sample (Mn182) it is scarcely visible.

The As K edge absorption spectrum can be interpreted in terms of the part of the one-particle density of states that is accessible from the 1s core level [98,99] (in contrast to shallower absorption edges, where multiplet effects are important [100]). Due to the electric dipole selection rules and the Pauli Exclusion Principle, the absorption spectrum is determined by the partial densities of unoccupied states with As $4p$ character, and their corresponding transition probabilities. In semiconducting GaAs, the unoccupied $4p$ states lie in the conduction band. However, if it is doped with acceptors, then this will introduce additional unoccupied states near E_F, and transitions to these states will be allowed if they have As $4p$ character. Hence, the presence of an XMCD signal at lower energy than the main absorption edge is an indicator of a density of unoccupied As $4p$ states near the valence band edge in Mn-doped GaAs and (In,Ga)As. This clearly indicates that the holes in (Ga,Mn)As at least partly occupy GaAs-like valence band states with As $4p$ character. Furthermore, it also indicates that these states have a net orbital magnetic moment, and thus are participators in the magnetic order. Due to the absence of spin-orbit coupling in the core state, XMCD at the K edge is only sensitive to the orbital moment of the valence states, and not the spin. [60,61].

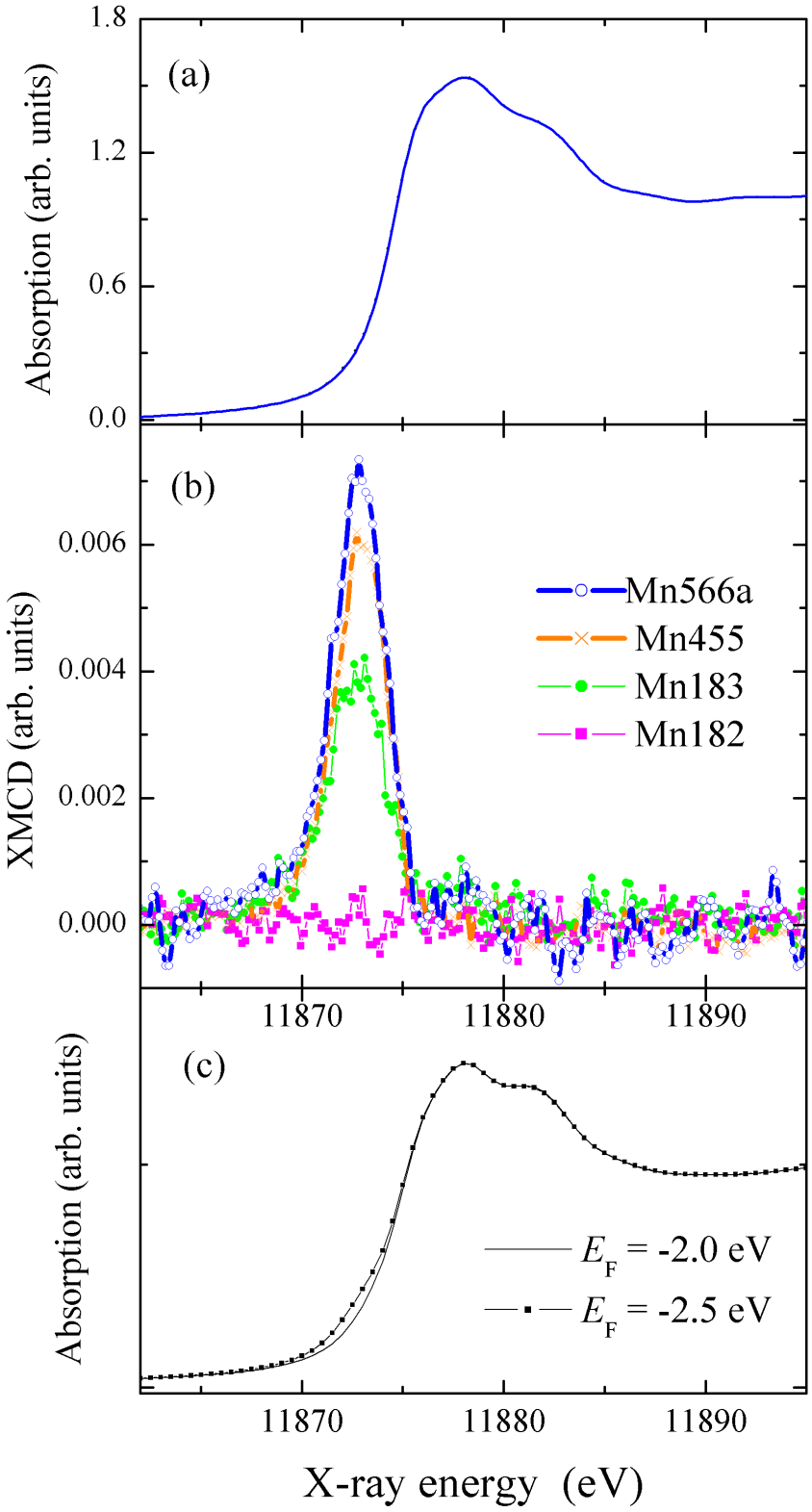

Figure 5.7 – XANES (a) and XMCD (b) curves at the As K edge. (c) shows simulation of the As K edge using the FDMNES code, for two different Fermi levels.

To add support to the above picture, Fig. 5.7(c) shows As K edge x-ray absorption spectra of GaAs calculated using the FDMNES code. [98] The calculation was performed for a 99-atom cluster, using a finite-differences method to model the interatomic potentials. The x-ray absorption lineshape is qualitatively reproduced by the calculation. Most significantly, shifting the Fermi level in the calculation results in an increased intensity at the energy position of the measured XMCD peak. This strongly suggests that, even though the XMCD peak does not coincide with a distinct feature in the absorption spectrum, it is associated with transitions into states near E_F that become unoccupied due to p-type doping.

More detailed first-principles calculations of the As K edge absorption and XMCD in (Ga,Mn)As have recently been reported by Antonov *et al* [99]. The calculated XMCD spectrum essentially consists of a single sharp peak at the onset of the edge, in agreement with the present measurements (see Figure 5.8). The XMCD was shown to arise due to a combination of the spin-orbit splitting of the As $4p$ states and exchange splitting at the neighbouring Mn site [99].

To confirm the dependence of the As XMCD on the ferromagnetic order of the Mn, we measured the XMCD signal as a function of both the external magnetic field and temperature. The absorption signal was measured for left- and right-handed circular polarization, at a fixed energy E=11873 eV corresponding to the XMCD peak. The difference as a function of magnetic field is shown in Figure 5.9, for sample Mn454. A transition from a ferromagnetic to a paramagnetic response is observed on crossing T_C =62 K. The inset compares the temperature dependence of the XMCD and the bulk magnetization obtained by SQUID magnetometry, at a fixed field of 0.1 T. The measurements are in agreement, showing that the As orbital moment is clearly associated with the magnetic order of the Mn ions.

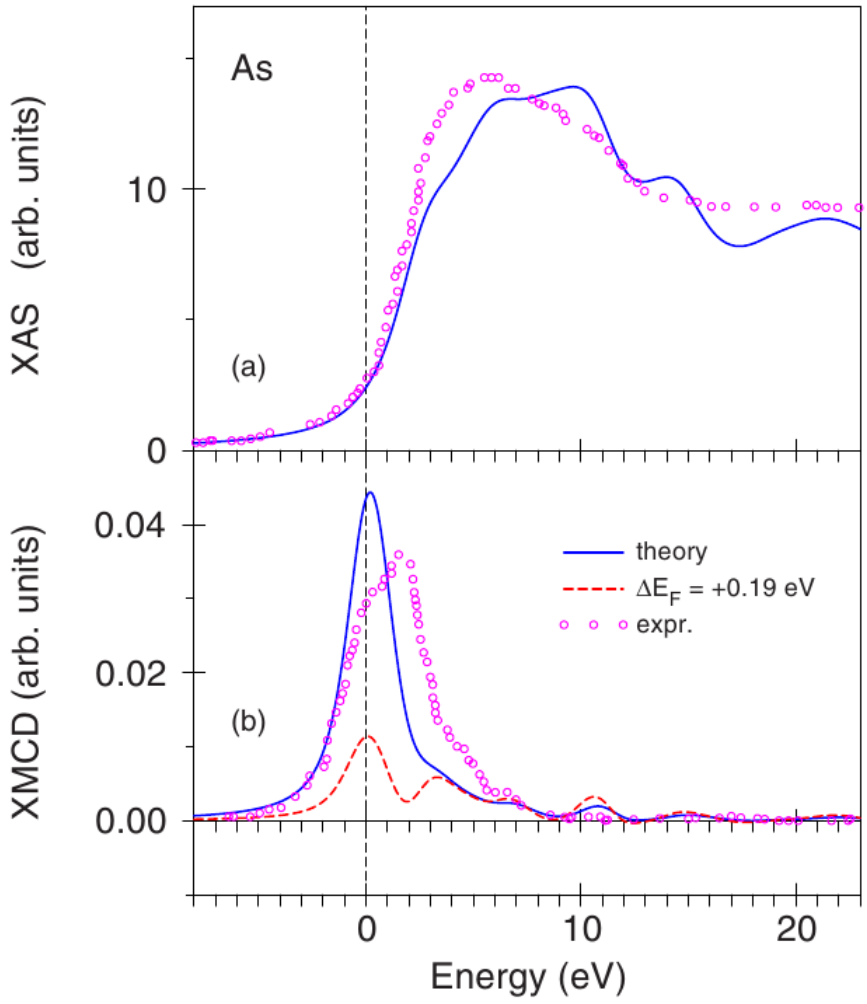

Figure 5.8 – (a) Experimentally measured XAS (purple circles) for the As K edge in (Ga,Mn)As and first principles theoretical model (blue solid). (b) experimentally measured and theoretically calculated XMCD spectra. The red dashed line shows the affect of an artificially shifted Fermi level on the model XMCD. Adapted from paper by Antonov *et al* [99]. The experimentally measured XAS and XMCD were reported in Ref. [53] and correspond to sample Mn183 of the present study.

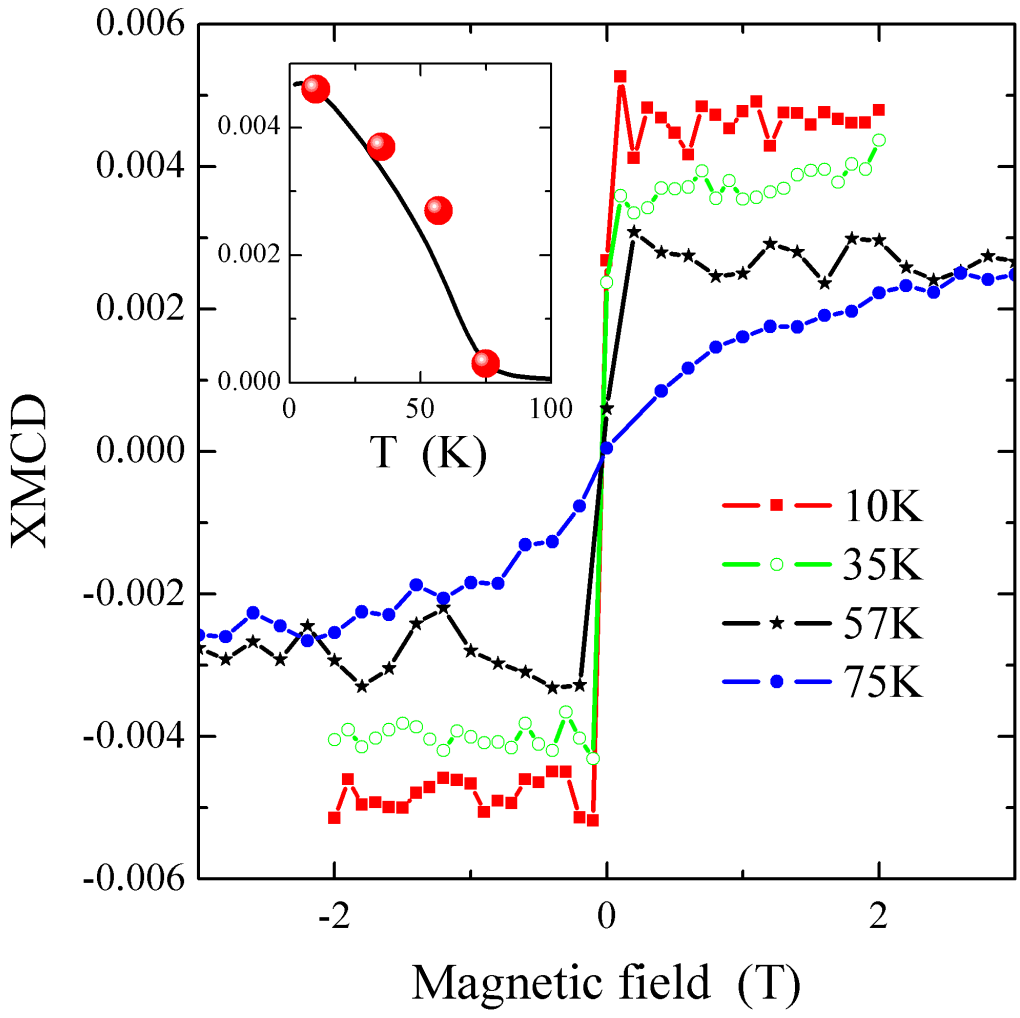

Figure 5.9 – Hysteresis loops generated using the size of the As K edge XMCD at its peak energy and sweeping the field for sample Mn454. The XMCD data was generated at 30° grazing incidence. (inset) The magnitude of the XMCD against temperature (filled red circles) with SQUID data (solid black line) at fixed field of 0.1 T. The SQUID measurements were taken in-plane.

The integrated XMCD intensity can be related to the element-specific orbital magnetic moment by application of the magneto-optical sum rule for orbital moment (as described in Section 2.4.2. [60] For the As K edge, the $4p$ orbital moment per As ion is given by $m_{orb,4p} = -(6 - n_{4p})(2I_{XMCD}/3I_{XAS})$, where I_{XMCD} and I_{XAS} are the integrated XMCD signal over the absorption edge and the integrated absorption for $1s$ to $4p$ transitions respectively. n_{4p} is the electron count in the $4p$ shell, which we take to be equal to 3 (i.e. fully covalent bonding is assumed). We separate the $1s$ to $4p$ contributions to the absorption edge from the $1s$ to continuum background by modelling the background as a step function positioned under the highest intensity point of the absorption spectrum. The estimated 10-20% uncertainties introduced by these assumptions are systematic, so that the relative values of the orbital moments per ion from the different samples can be compared with high accuracy.

Figure 5.10 shows the obtained orbital moments per As ion from sum rule analysis of the six samples studied. The result is plotted against the saturation magnetization M_S [Fig. 5.10(a)] and the T_C [Fig. 5.10(b)] of the (Ga,Mn)As and (In,Ga,Mn)As films obtained by SQUID magnetometry. The As $4p$ orbital moment increases approximately linearly with increasing M_S, which is a measure of the concentration of Mn local magnetic moments that are participating in the ferromagnetism. This further indicates that the As polarization is induced by proximity to ferromagnetically ordered substitutional Mn. However, the As orbital moment falls to zero (within the experimental uncertainty) for finite values of M_S and T_C, suggesting that the presence of a significant As orbital polarization is not a necessary condition for ferromagnetism in (III,Mn)As materials.

Substitution of In for Ga results in competing effects which may influence the magnitude of the orbital moment on the As ion. On the one hand, it expands the lattice, leading to a weaker overlap of As and Mn orbitals. On the other, it enhances the valence band spin-orbit splitting, and also shifts the position of the host valence band edge relative to the Mn acceptor level. The similar magnitude of As $4p$ orbital moment in (Ga,Mn)As and (In,Ga,Mn)As is likely to be due to the interplay of these competing effects.

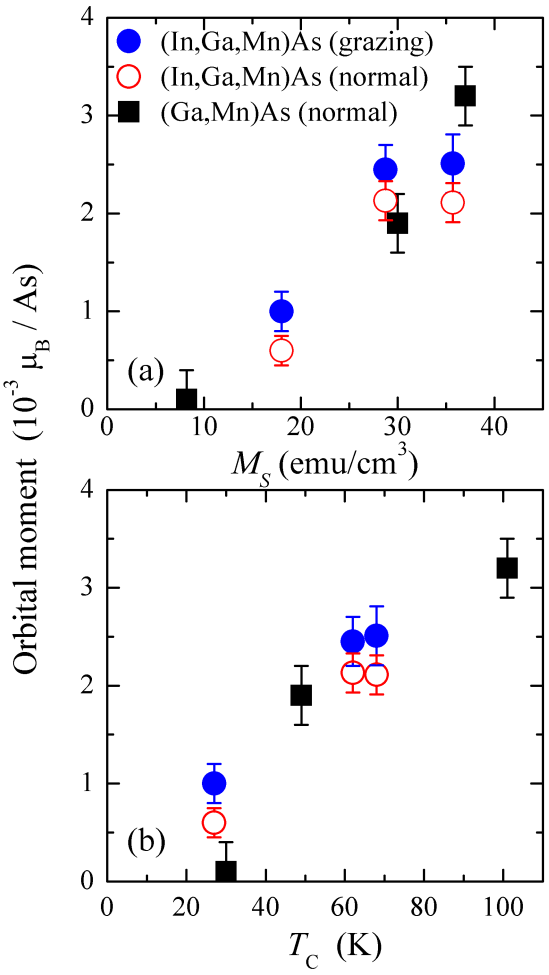

Figure 5.10 – As 4*p* Orbital magnetic moment calculated using applied sum rules versus T_C and magnetization, as measured by SQUID magnetometry. XMCD data was recorded at 7 K with 6 T applied field.

5.2.2 XMCD at the Mn *K* edge

The absorption and XMCD spectra recorded at the Mn K edge are shown in Figure 5.11. The absorption spectra are consistent with earlier studies, including the weak pre-edge peak centred at 6540 eV, followed by a broad and structured absorption edge [101, 102]. The largest contribution to the XMCD signal consists of a sharp double-peak structure centred on the small pre-edge peak, together with a broader component of the same sign around 6545 eV. The most remarkable observation is that both the magnitude of the XMCD and the intensity ratio of the double-peak structure are strongly dependent on the Mn concentration. At low doping, where samples are on the insulating side of the metal-insulator transition, there is a dramatic increase in the intensity of the lowest energy XMCD peak,

labelled A in Figure 5.11. At 1% Mn doping (Mn586) the peak A is around a factor of 5 larger than for the more metallic annealed 5% film (Mn566a). The low-doped films also show increased intensity in the region between the second and third peaks in the XMCD spectra, centred around 6543 eV.

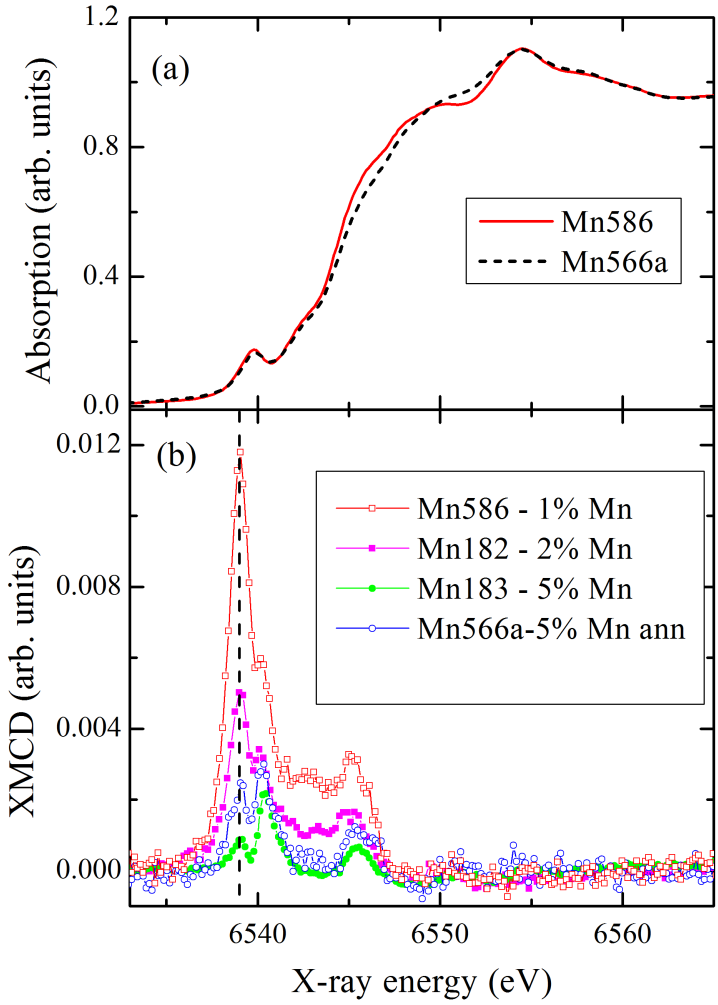

Figure 5.11 – XANES and XMCD curves at the Mn K absorption edge

Pre-edge structures are a common feature in the K edge absorption spectra of $3d$ ions, and are usually associated with a $1s$ to $3d$ transition. While such a transition is formally electric-dipole forbidden, it can gain intensity through a mixing of $3d$ and $4p$ orbitals. [103,104] First principles calculations have shown that

the pre-edge feature consists of two merged peaks, corresponding to transitions from the $1s$ core level to two bands of hybridized Mn $4p$ states. [99, 104] The lower energy peak corresponds to a spin-up band at E_F, while the higher energy peak corresponds to an unoccupied spin-down band within the energy gap. The resulting XMCD spectrum is closely related to the energy-resolved Mn $4p$ orbital polarization per Mn ion. [99] The calculated XMCD spectrum, obtained in Ref. [99] using the local spin density approximation (LSDA), shows a comparable ratio of the pre-edge double peak heights to our measured result for low-doped films, with peak A dominant in the spectrum.

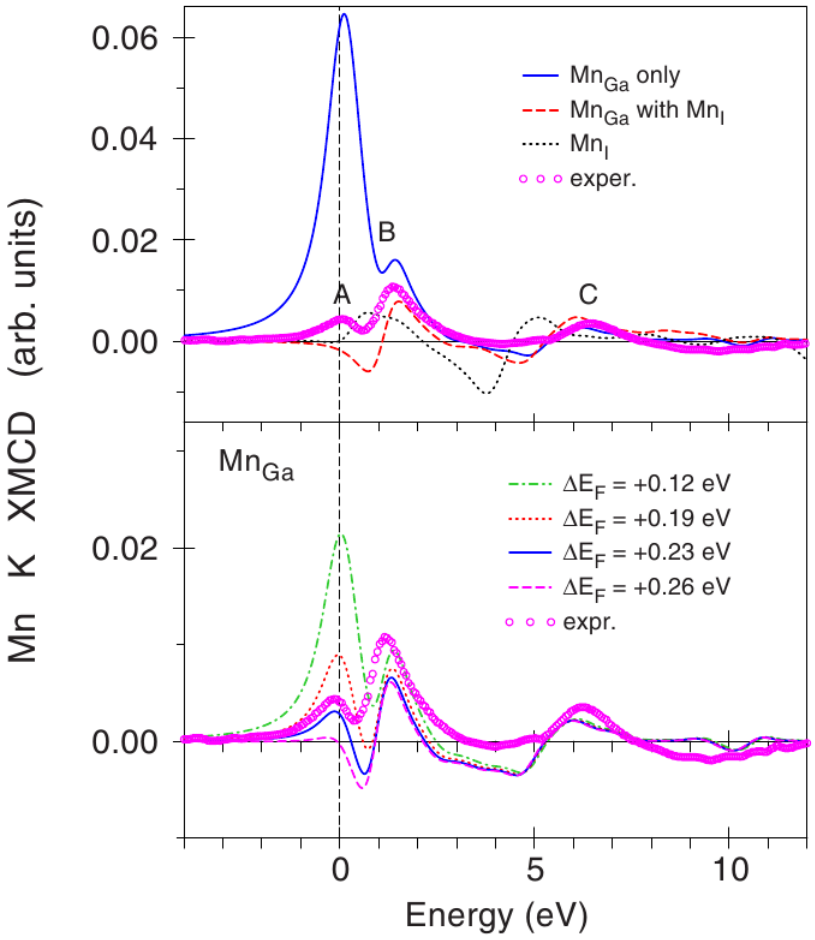

Figure 5.12 – XMCD at the Mn K edge calculated using the local spin density approximation (LSDA). The blue solid line in the top panel shows the calculation for Mn_{int} only with no artificial shift to the Fermi level. The bottom panel shows the effect of shifting the Fermi level towards the gap in a rigid band model. Adapted from Antonov *et al* [99]. The experimentally measured XAS and XMCD were reported in Ref. [53] and correspond to sample Mn183 of the present study.

In Ref. [99], it was shown that the height of peak A is considerably reduced if E_F is shifted towards the gap in a rigid-band picture (see Figure 5.12). Therefore, the small size of the measured peak A in the metallic (Ga,Mn)As films, reported previously in Ref. [53] was attributed to a Fermi level shift induced by compensating defects such as interstitial Mn. The increase of peak A in the annealed film Mn566a compared to the as-grown film Mn183 is qualitatively consistent with this. However, this increase is small compared to the dramatic enhancement of peak A in the insulating layers.

It is known that the LSDA used in Ref. [99] tends to overestimate the $3d$ weight of the states at E_F [105]. In the metallic regime of (Ga,Mn)As, due to screening of the Coulomb interactions between the holes and acceptors, the states at E_F are not bound to the Mn ions, but are instead delocalized across the system. The above considerations suggest the following interpretation of the dependence of the Mn XMCD peak A on doping. In the low doped, insulating regime, the valence holes are bound to the Mn acceptors, and are thus accessible from a Mn $1s$ core level excitation. Below T_C, these bound holes have a large orbital polarization, so that the XMCD at the onset of the Mn K pre-edge is large. At higher doping, the valence holes are more extended, leading to a reduction in the probability of exciting a transition to these states from the $1s$ core level. There is thus a clear connection between the XMCD signals at the lowest energies of the Mn and As K edges: on crossing the metal-insulator transition, there is a transfer of the orbital polarization of the states near E_F from the Mn to the As ions; as a result, the XMCD at the Mn K edge decreases, and the XMCD at the As K edge increases.

5.3 Conclusions

In both the As and Mn K edge XMCD spectra of (Ga,Mn)As and (In,Ga,Mn)As films, we observe features at the onset of the edge that are associated with transitions into states at or just above the Fermi level. The intensity of these features is a measure of the orbital magnetic moment per ion of the corresponding valence states. A marked dependence on the Mn doping is observed. In low doped samples, the Mn XMCD is large, and the As XMCD is small; with increasing doping, the lowest energy Mn XMCD peak decreases dramatically in intensity. The As XMCD increases with the saturation magnetization (which is proportional to the concentration of Mn that is participating in the ferromagnetic order) and the ferromagnetic Curie temperature. These results are ascribed to a qualitative change

in the character of the polarized states at E_F that occurs on crossing the transition from the low-doped insulating state to the high-doped metallic state in the (III,Mn)As systems.

A transfer of the hole orbital magnetic moment from Mn to As sites may explain the success of 'host-like hole' models in calculating the magnetic and magnetotransport anisotropies, which are closely related to the valence band orbital polarization, in metallic (III,Mn)As materials [27, 29]. The presence of a significant As XMCD at the onset of the absorption edge is a clear indication of an As $4p$ character of the valence band holes, and its correlation with the magnetisation shows that the As $4p$ states participate in the magnetic order.

Consistent with the present results, these models break down for low-doped insulating (Ga,Mn)As, where the holes have a hybridized Mn $4p$ character. Anomalous properties of low-doped insulating films include giant anisotropic magnetoresistance, perpendicular-to-plane magnetic anisotropy [106] and a qualitatively different dependence of T_C on the carrier density [30]. In spite of the very different conductivity and nature of the states at E_F, ferromagnetism is observed in both regimes, with markedly lower T_C in the insulating case.

The XMCD at the Mn K edge shows a clear signature of hole localization in the insulating regime of (Ga,Mn)As. It would be of interest to determine whether such behaviour is observed in other transition metal doped semiconductors and insulators that are close to a metal-nonmetal transition. For example, alloying (Ga,Mn)As with AlAs shifts the transition to higher Mn concentrations due to the wider band gap of the semiconductor host, [43] so that the large Mn K edge XMCD may persist to higher doping. Similarly, (Ga,Mn)P shows hopping conductivity together with ferromagnetism up to the highest Mn concentrations studied; [107] for this material, due to hole localization the Mn K edge XMCD may be expected to be much larger than for metallic (Ga,Mn)As, even though the Mn $L_{2,3}$ edge XMCD spectra (which is primarily sensitive to the Mn $3d$ states) are very similar. [83] The K edge XMCD is a much more sensitive detector of hole localization than the unpolarized absorption spectrum, due to the sharply peaked orbital polarization at the Fermi level.

Chapter 6

Conclusions and future work

This thesis used a set of combined techniques to shed new light on some important processes in III-Mn-V dilute magnetic semiconductors. Using K edge XMCD, qualitative changes in the character of the states mediating ferromagnetism were demonstrated. These findings are consistent with models which portray the mediating carriers as being merged with the host valence band and itinerant across the whole system in metallic samples, and more localised in the insulating regime. L edge XMCD provided a detailed picture of the interlayer coupling in Fe/(Ga,Mn)As heterostructures, and revealed room temperature polarisation in a thin (Ga,Mn)As layer. Phosphorus doping in (Ga,Mn)As was shown to affect the strain present in the layer. This caused changes in the features of the XMCD of the Mn L edges, and led to changes in magnetic anisotropy, as well the magnetisation and conductivity.

6.1 Fe/(Ga,Mn)As heterostructures

A set of metal-semiconductor Fe/(Ga,Mn)As samples were grown using low temperature MBE, and characterised using SQUID magnetometry and XRR. The detailed coupling of the layers was then examined using XMCD, in a layer specific and element specific manner. An exchange bias effect was observed in the Fe/(Ga,Mn)As heterostructures, which was shown to affect the entire (Ga,Mn)As layer. The size of the exchange bias effect was larger than that observed previously for antiferromagnetically pinned (Ga,Mn)As layers [108]. A sub-nanometer interfacial region of (Ga,Mn)As was shown to be strongly exchange coupled to the Fe layer even above room temperature, whereas the bulk (Ga,Mn)As while also coupled antiferromagnetically at low fields could be rotated into alignment with larger fields. The thickness of the strongly coupled layer was estimated using the

magneto-optical sum rules to be $\sim 0.7\,\text{nm}$, which equates to approximately 2-3 monolayers assuming uniform material. This is also of the order of the depletion depth for a (Ga,Mn)As film with carrier density of $\sim 10^{20}\,cm^3$, which may explain the weak nature of the coupling to the remainder of the film.

Possible future work could include growing a similar structure but with a highly compensated (Ga,Mn)As layer. If the weak coupling to the bulk layer and the strongly coupled interfacial layer are indeed related to the depletion region then it may be possible to decouple the bulk layer from the Fe layer by increasing the size of the depletion region at the interface. This may also affect the size of the strongly coupled layer, and could shed more light on the nature of the coupling.

6.2 XMCD study of Phosphorus doping in (Ga,Mn)(As,P)

A set of $Ga_{0.94}Mn_{0.6}As_{1-y}P_y$ samples were grown with $y = 0, 0.03, 0.06, 0.09, 0.1, 0.2$ and 0.3. The samples were examined using XRD, SQUID magnetometry and XMCD at the Mn $L_{3,2}$ edge.

The change in the height of a uniaxial prepeak feature in the L edge XMCD of Mn at normal incidence, first identified by Edmonds et al [84], was related to the percentage strain, calculated using high resolution XRD, and found to scale linearly. The weak dependence of the height of this same feature at 60° demonstrates that the local electronic environment of the Mn is not affected significantly by the P incorporation. The changes in layer strain were shown to strongly affect the magnetic anisotropy of the (Ga,Mn)(As,P) films, without significantly altering the Mn local environment, or altering the crystal quality.

X-ray magneto-optical sum rules analysis was used to show a steady decrease in total moment per Mn atom with P concentrations above $\sim 10\%$. Lineshape analysis of the XMCD demonstrates that this is not due to a change in the local magnetic moment of the Mn, and therefore it seems likely that the decrease in moment is due to reduced participation of Mn in the ferromagnetic order. Since the XMCD line shape is nearly identical across all concentrations this also precludes increased localisation of the carriers with $3d$ character. However, since XMCD at the L edge is not directly sensitive to carriers with $4p$ character, an increased localisation in these carriers, as seen in the K edge analysis of (Ga,Mn)As and

(In,Ga,Mn)(As) samples in Chapter 5, may be responsible.

It would be interesting to investigate the origin of the decreased moment observed in highly doped (Ga,Mn)(As,P) films. A similar trend in T_C with doping is observed in $Al_yGa_{1-y-x}Mn_xAs$, indicating that similar mechanisms may be responsible. It would be interesting to conduct a K edge XMCD study on a range of doping in both (Ga,Mn)(As,P) and (Al,Ga,Mn)As, in the same manner as in Chapter 5, to see if a localisation in carriers with $4p$ character occurs there as well.

Apart from the decrease in T_C and moment, (Ga,Mn)(As,P) provides a system with high quality crystalline and micromagnetic properties, as well as tunable anisotropy over a large range. This would be useful for detecting domain wall motion, electric-field driven magnetisation reversal, and any other effects which lend themselves to detection via the sensitive magneto-optical Kerr effect.

This study also highlights the potential usefulness of XMCD as a simultaneous probe of strain and magnetic properties. This would be useful for studies involving magnetostriction and piezoelectrically or ferroelectrically driven magnetisation reversal. (Ga,Mn)(As,P) also provides a model system for further quantifying the strain dependence of XMCD.

6.3 K-edge XMCD study of (III,Mn)As samples

A set of (In,Ga,Mn)(As) and (Ga,Mn)As samples were grown and characterised using transport and SQUID measurements. These samples were then examined using XMCD at the Mn and As K absorption edges. For both the Mn and As absorption edges XMCD is observed at the onset of the absorption edge. This indicates that the states connected with these magnetic features are at or just above the Fermi level. A remarkable transfer of orbital moment from the Mn to the As sites was seen on increasing the doping level. This result is interpreted as a marked change in the character of the polarised states upon crossing from the insulating regime to the metallic. This result explains the success of 'host-like' models in reproducing the magnetic and magnetotransport properties of metallic (III,Mn)As materials. It is also consistent with the breakdown of these models for the insulating low-doped samples, where the holes seem to have a more localised

hybridized Mn4p character.

Both (Ga,Mn)(As,P) and (Al,Ga,Mn)As show a similar trend in T_C with doping as discussed in Section 6.2. It would be very interesting to see if a similar transfer of orbital momentum was observed in these systems also.

The increase in orbital momentum associated with the Mn 4p states increased with decreased doping, and did not appear to saturate in this study. Despite the apparent highly localised nature of the magnetic states at low doping the samples were still ferromagnetic, albeit with low T_C. It would be interesting to see at what stage the Mn moment saturates and what the magnetic properties of such samples are.

References

[1] M. N. Baibich, J. M. Broto, A. Fert, F. Nguyen Van Dau, F. Petroff, P. Etienne, G. Creuzet, A. Friederich, and J. Chazelas. Giant magnetoresistance of (001)Fe/(001)Cr magnetic superlattices. *Phys. Rev. Lett.*, 61:2472–2475, Nov 1988.

[2] S. A. Wolf, D. D. Awschalom, R. A. Buhrman, J. M. Daughton, S. von Molnar, M. L. Roukes, A. Y. Chtchelkanova, and D. M. Treger. Spintronics: A Spin-Based Electronics Vision for the Future. *Science*, 294(5546):1488–1495, 2001.

[3] J. A. Gupta, R. Knobel, N. Samarth, and D. D. Awschalom. Ultrafast manipulation of electron spin coherence. *Science*, 292(5526):2458–2461, 2001.

[4] J. K. Furdyna. Diluted magnetic semiconductors. *Journal of Applied Physics*, 64(4):R29–R64, 1988.

[5] Y. Ohno, D. K. Young, B. Beschoten, F. Matsukura, H. Ohno, and D. D. Awschalom. Electrical spin injection in a ferromagnetic semiconductor heterostructure. *Nature*, 402(6763):790–792, December 1999.

[6] H. Ohno, D. Chiba, F. Matsukura, T. Omiya, E. Abe, T. Dietl, Y. Ohno, and K. Ohtani. Electric-field control of ferromagnetism. *Nature*, 408(6815):944–946, December 2000.

[7] D. Chiba, M. Yamanouchi, F. Matsukura, and H. Ohno. Electrical manipulation of magnetization reversal in a ferromagnetic semiconductor. *Science*, 301(5635):943–945, 2003.

[8] M. Yamanouchi, D. Chiba, F. Matsukura, and H. Ohno. Current-induced domain-wall switching in a ferromagnetic semiconductor structure. *Nature*, 428(6982):539–542, April 2004.

[9] C. Gould, C. Rüster, T. Jungwirth, E. Girgis, G. M. Schott, R. Giraud, K. Brunner, G. Schmidt, and L. W. Molenkamp. Tunneling anisotropic

magnetoresistance: A spin-valve-like tunnel magnetoresistance using a single magnetic layer. *Phys. Rev. Lett.*, 93:117203, Sep 2004.

[10] J. Wunderlich, T. Jungwirth, B. Kaestner, A. C. Irvine, A. B. Shick, N. Stone, K.-Y. Wang, U. Rana, A. D. Giddings, C. T. Foxon, R. P. Campion, D. A. Williams, and B. L. Gallagher. Coulomb blockade anisotropic magnetoresistance effect in a (Ga, Mn)As single-electron transistor. *Phys. Rev. Lett.*, 97:077201, Aug 2006.

[11] K. W. Edmonds, K. Y. Wang, R. P. Campion, A. C. Neumann, N. R. S. Farley, B. L. Gallagher, and C. T. Foxon. High-curie-temperature $Ga_{1-x}Mn_xAs$ obtained by resistance-monitored annealing. *Applied Physics Letters*, 81(26):4991–4993, 2002.

[12] H. Munekata, H. Ohno, S. von Molnar, Armin Segmüller, L. L. Chang, and L. Esaki. Diluted magnetic III-V semiconductors. *Phys. Rev. Lett.*, 63:1849–1852, Oct 1989.

[13] C. T. Foxon and B. A. Joyce. Fundamental aspects of molecular beam epitaxy. *Current Topics in Materials Science*, 7:3–68, 81.

[14] J. H. Neave, B. A. Joyce, and P. J. Dobson. Dynamic RHEED observations of the MBE growth of GaAs. *Applied Physics A: Materials Science & Processing*, 34:179–184, 1984. 10.1007/BF00616915.

[15] H. Ohno, H. Munekata, S. von Molnr, and L. L. Chang. New (III,V) diluted magnetic semiconductors (invited). 69(8):6103–6108, 1991.

[16] H. Ohno, H. Munekata, T. Penney, S. von Molnár, and L. L. Chang. Magnetotransport properties of p-type (In,Mn)As diluted magnetic III-V semiconductors. *Phys. Rev. Lett.*, 68(17):2664–2667, Apr 1992.

[17] H. Ohno, A. Shen, F. Matsukura, A. Oiwa, A. Endo, S. Katsumoto, and Y. Iye. (Ga,Mn)As: a new diluted magnetic semiconductor based on GaAs. *Applied Physics Letters*, 69(3):363–365, 1996.

[18] L. X. Zhao, C. R. Staddon, K. Y. Wang, K. W. Edmonds, R. P. Campion, B. L. Gallagher, and C. T. Foxon. Intrinsic and extrinsic contributions to the lattice parameter of GaMnAs. *Applied Physics Letters*, 86(7):071902, 2005.

[19] J. Blinowski and P. Kacman. Spin interactions of interstitial Mn ions in ferromagnetic GaMnAs. *Phys. Rev. B*, 67:121204, Mar 2003.

[20] G. M. Schott, G. Schmidt, G. Karczewski, L. W. Molenkamp, R. Jakiela, A. Barcz, and G. Karczewski. Influence of growth conditions on the lattice constant and composition of (Ga,Mn)As. *Applied Physics Letters*, 82(26):4678–4680, 2003.

[21] T. Jungwirth, Jairo Sinova, A. H. MacDonald, B. L. Gallagher, V. Novak, K. W. Edmonds, A. W. Rushforth, R. P. Campion, C. T. Foxon, L. Eaves, E. Olejnik, J. Masek, S.-R. Eric Yang, J. Wunderlich, C. Gould, L. W. Molenkamp, T. Dietl, and H. Ohno. Character of states near the fermi level in (Ga,Mn)As: Impurity to valence band crossover. *Physical Review B (Condensed Matter and Materials Physics)*, 76(12):125206, 2007.

[22] M. A. Mayer, P. R. Stone, N. Miller, H. M. Smith, O. D. Dubon, E. E. Haller, K. M. Yu, W. Walukiewicz, X. Liu, and J. K. Furdyna. Electronic structure of $Ga_{1-x}Mn_xAs$ analyzed according to hole-concentration-dependent measurements. *Phys. Rev. B*, 81:045205, Jan 2010.

[23] K. S. Burch, D. B. Shrekenhamer, E. J. Singley, J. Stephens, B. L. Sheu, R. K. Kawakami, P. Schiffer, N. Samarth, D. D. Awschalom, and D. N. Basov. Impurity band conduction in a high temperature ferromagnetic semiconductor. *Phys. Rev. Lett.*, 97:087208, Aug 2006.

[24] T. Jungwirth, K. Y. Wang, J. Mašek, K. W. Edmonds, Jürgen König, Jairo Sinova, M. Polini, N. A. Goncharuk, A. H. MacDonald, M. Sawicki, A. W. Rushforth, R. P. Campion, L. X. Zhao, C. T. Foxon, and B. L. Gallagher. Prospects for high temperature ferromagnetism in (Ga,Mn)As semiconductors. *Phys. Rev. B*, 72:165204, Oct 2005.

[25] M. Wang, R. P. Campion, A. W. Rushforth, K. W. Edmonds, C. T. Foxon, and B. L. Gallagher. Achieving high curie temperature in (Ga,Mn)As. *Applied Physics Letters*, 93(13):132103, 2008.

[26] T. Dietl, H. Ohno, F. Matsukura, J. Cibert, and D. Ferrand. Zener model description of ferromagnetism in zinc-blende magnetic semiconductors. *Science*, 287(5455):1019–1022, 2000.

[27] A. W. Rushforth, K. Výborný, C. S. King, K. W. Edmonds, R. P. Campion, C. T. Foxon, J. Wunderlich, A. C. Irvine, P. Vašek, V. Novák, K. Olejník, Jairo Sinova, T. Jungwirth, and B. L. Gallagher. Anisotropic magnetoresistance components in (Ga,Mn)As. *Phys. Rev. Lett.*, 99(14):147207, Oct 2007.

[28] Maciej Sawicki, Daichi Chiba, Anna Korbecka, Yu Nishitani, Jacek A. Majewski, Fumihiro Matsukura, Tomasz Dietl, and Hideo Ohno. Experimental probing of the interplay between ferromagnetism and localization in (Ga, Mn)As. *Nat Phys*, 6(1):22–25, January 2010.

[29] T. Dietl, H. Ohno, and F. Matsukura. Hole-mediated ferromagnetism in tetrahedrally coordinated semiconductors. *Phys. Rev. B*, 63(19):195205, Apr 2001.

[30] B. L. Sheu, R. C. Myers, J.-M. Tang, N. Samarth, D. D. Awschalom, P. Schiffer, and M. E. Flatté. Onset of ferromagnetism in low-doped $Ga_{1-x}Mn_xAs$. *Phys. Rev. Lett.*, 99(22):227205, Nov 2007.

[31] Gerrit van der Laan. Magnetic linear x-ray dichroism as a probe of the magnetocrystalline anisotropy. *Phys. Rev. Lett.*, 82:640–643, Jan 1999.

[32] Hans Christoph Siegmann Joachim Stöhr. *Magnetism - From Fundamentals to Nanoscale Dynamics*. Springer series in solid - state sciences, 2006.

[33] W. H. Meiklejohn and C. P. Bean. New magnetic anisotropy. *Phys. Rev.*, 102:1413–1414, Jun 1956.

[34] S. S. P. Parkin, N. More, and K. P. Roche. Oscillations in exchange coupling and magnetoresistance in metallic superlattice structures: Co/Ru, Co/Cr, and Fe/Cr. *Phys. Rev. Lett.*, 64:2304–2307, May 1990.

[35] P. Bruno. Theory of interlayer magnetic coupling. *Phys. Rev. B*, 52:411–439, Jul 1995.

[36] T. Jungwirth, W. A. Atkinson, B. H. Lee, and A. H. MacDonald. Interlayer coupling in ferromagnetic semiconductor superlattices. *Phys. Rev. B*, 59:9818–9821, Apr 1999.

[37] J.-H. Chung, S. J. Chung, Sanghoon Lee, B. J. Kirby, J. A. Borchers, Y. J. Cho, X. Liu, and J. K. Furdyna. Carrier-mediated antiferromagnetic interlayer exchange coupling in diluted magnetic semiconductor multilayers $Ga_{1-x}Mn_xAs/GaAs:Be$. *Phys. Rev. Lett.*, 101:237202, Dec 2008.

[38] K. Dziatkowski, Z. Ge, X. Liu, and J. K. Furdyna. Identification of unidirectional anisotropy in exchange-biased MnO/GaMnAs bilayers using ferromagnetic resonance. *Applied Physics Letters*, 88(14):142513, 2006.

[39] H. T. Lin, Y. F. Chen, P. W. Huang, S. H. Wang, J. H. Huang, C. H. Lai, W. N. Lee, and T. S. Chin. Enhancement of exchange coupling between

GaMnAs and IrMn with self-organized Mn(Ga)As at the interface. *Applied Physics Letters*, 89(26):262502, 2006.

[40] Peter R. Stone, Jeffrey W. Beeman, Kin M. Yu, and Oscar D. Dubon. Tuning of ferromagnetism through anion substitution in Ga-Mn-pnictide ferromagnetic semiconductors. *Physica B: Condensed Matter*, 401-402:454 – 457, 2007. Proceedings of the 24th International Conference on Defects in Semiconductors.

[41] P. R. Stone, K. Alberi, S. K. Z. Tardif, J. W. Beeman, K. M. Yu, W. Walukiewicz, and O. D. Dubon. Metal-insulator transition by isovalent anion substitution in $Ga_{1-x}Mn_xAs$: Implications to ferromagnetism. *Phys. Rev. Lett.*, 101(8):087203, Aug 2008.

[42] A. Lemaitre, A. Miard, L. Travers, O. Mauguin, L. Largeau, C. Gourdon, V. Jeudy, M. Tran, and J.-M. George. Strain control of the magnetic anisotropy in (Ga,Mn) (As,P) ferromagnetic semiconductor layers. *Applied Physics Letters*, 93(2):021123, 2008.

[43] A. W. Rushforth, M. Wang, N. R. S. Farley, R. P. Campion, K. W. Edmonds, C. R. Staddon, C. T. Foxon, and B. L. Gallagher. Molecular beam epitaxy grown (Ga,Mn)(As,P) with perpendicular to plane magnetic easy axis. *Journal of Applied Physics*, 104(7):073908, 2008.

[44] A. Casiraghi, A. W. Rushforth, M. Wang, N. R. S. Farley, P. Wadley, J. L. Hall, C. R. Staddon, K. W. Edmonds, R. P. Campion, C. T. Foxon, and B. L. Gallagher. Tuning perpendicular magnetic anisotropy in (Ga,Mn)(As,P) by thermal annealing. *Applied Physics Letters*, 97(12):122504, 2010.

[45] M. Cubukcu, H. J. von Bardeleben, Kh. Khazen, J. L. Cantin, O. Mauguin, L. Largeau, and A. Lemaître. Adjustable anisotropy in ferromagnetic (Ga,Mn) (As,P) layered alloys. *Phys. Rev. B*, 81(4):041202, Jan 2010.

[46] J. Masek, J. Kudrnovsky, F. Máca, Jairo Sinova, A. H. MacDonald, R. P. Campion, B. L. Gallagher, and T. Jungwirth. Mn-doped Ga(As,P) and (Al,Ga)As ferromagnetic semiconductors: Electronic structure calculations. *Phys. Rev. B*, 75:045202, 2007.

[47] Jerzy M. Langer, C. Delerue, M. Lannoo, and Helmut Heinrich. Transition-metal impurities in semiconductors and heterojunction band lineups. *Phys. Rev. B*, 38:7723–7739, Oct 1988.

[48] J.L. Xu and M. van Schilfgaarde. Optimizing in the (Mn,Cr,Ga)As and (Mn,Ga)(As,P) ternary alloys. *Journal of Magnetism and Magnetic Materials*, 305(1):63 – 67, 2006.

[49] F. Maccherozzi, M. Sperl, G. Panaccione, J. Minár, S. Polesya, H. Ebert, U. Wurstbauer, M. Hochstrasser, G. Rossi, G. Woltersdorf, W. Wegscheider, and C. H. Back. Evidence for a magnetic proximity effect up to room temperature at Fe/(Ga,Mn)As interfaces. *Phys. Rev. Lett.*, 101(26):267201, Dec 2008.

[50] M. Sperl, F. Maccherozzi, F. Borgatti, A. Verna, G. Rossi, M. Soda, D. Schuh, G. Bayreuther, W. Wegscheider, J. C. Cezar, F. Yakhou, N. B. Brookes, C. H. Back, and G. Panaccione. Identifying the character of ferromagnetic Mn in epitaxial Fe/(Ga,Mn)As heterostructures. *Phys. Rev. B*, 81:035211, Jan 2010.

[51] T. Jungwirth, Jairo Sinova, J. Masek, J. Kucera, and A. H. MacDonald. Theory of ferromagnetic (III,Mn)V semiconductors. *Reviews of Modern Physics*, 78(3):809, 2006.

[52] Kenta Takata & Masaaki Tanaka Shinobu Ohya. Nearly non-magnetic valence band of the ferromagnetic semiconductor gamnas. *Nature Physics*, 7:342?347, 2011.

[53] A. A. Freeman, K. W. Edmonds, G. van der Laan, R. P. Campion, N. R. S. Farley, A. W. Rushforth, T. K. Johal, C. T. Foxon, B. L. Gallagher, A. Rogalev, and F. Wilhelm. Valence band orbital polarization in III-V ferromagnetic semiconductors. *Phys. Rev. B 77*, 073304 (2008), 2008.

[54] T.A. Ezquerra M.C. García-Gutiérrez A.Nogales. *Applications of Synchrotron Light to Scattering and Diffraction in Materials and Life Sciences.* Springer, 2009.

[55] Shigemi Sasaki. Analyses for a planar variably-polarizing undulator. *Nuclear Instruments and Methods in Physics Research Section A: Accelerators, Spectrometers, Detectors and Associated Equipment*, 347(1-3):83 – 86, 1994.

[56] W. J. Bartels. Characterization of thin layers on perfect crystals with a multipurpose high resolution x-ray diffractometer. *Journal of Vacuum Science Technology B: Microelectronics and Nanometer Structures*, 1(2):338 –345, apr 1983.

[57] J. L. Erskine and E. A. Stern. Calculation of the $m23$ magneto-optical absorption spectrum of ferromagnetic nickel. *Phys. Rev. B*, 12(11):5016–5024, Dec 1975.

[58] G. Schütz, W. Wagner, W. Wilhelm, P. Kienle, R. Zeller, R. Frahm, and G. Materlik. Absorption of circularly polarized x rays in iron. *Phys. Rev. Lett.*, 58(7):737–740, Feb 1987.

[59] C. T. Chen, F. Sette, Y. Ma, and S. Modesti. Soft-x-ray magnetic circular dichroism at the $L_{2,3}$ edges of Nickel. *Phys. Rev. B*, 42(11):7262–7265, Oct 1990.

[60] B. T. Thole, P. Carra, F. Sette, and G. van der Laan. X-ray circular dichroism as a probe of orbital magnetization. *Phys. Rev. Lett.*, 68(12):1943–1946, Mar 1992.

[61] Paolo Carra, B. T. Thole, Massimo Altarelli, and Xindong Wang. X-ray circular dichroism and local magnetic fields. *Phys. Rev. Lett.*, 70(5):694–697, Feb 1993.

[62] C. T. Chen, Y. U. Idzerda, H.-J. Lin, N. V. Smith, G. Meigs, E. Chaban, G. H. Ho, E. Pellegrin, and F. Sette. Experimental Confirmation of the X-Ray Magnetic Circular Dichroism Sum Rules for Iron and Cobalt. *Phys. Rev. Lett.*, 75(1):152–155, Jul 1995.

[63] U. Fano. Spin orientation of photoelectrons ejected by circularly polarized light. *Phys. Rev.*, 178(1):131–136, Feb 1969.

[64] Eli Stavitski and Frank M.F. de Groot. The ctm4xas program for eels and xas spectral shape analysis of transition metal l edges. *Micron*, 41(7):687 – 694, 2010.

[65] F. de Groot and A. Kotani. *Core Level Spectroscopy of Solids - Advances in Condensed Matter Science.* CRC Press, Boca Raton, FL, 2008.

[66] H. Ohldag, V. Solinus, F. U. Hillebrecht, J. B. Goedkoop, M. Finazzi, F. Matsukura, and H. Ohno. Magnetic moment of mn in the ferromagnetic semiconductor $(Ga_{0.98}Mn_{0.02})As$. 76(20):2928–2930, 2000.

[67] K. W. Edmonds, N. R. S. Farley, T. K. Johal, G. van der Laan, R. P. Campion, B. L. Gallagher, and C. T. Foxon. Ferromagnetic moment and antiferromagnetic coupling in (Ga,Mn)As thin films. *Phys. Rev. B*, 71(6):064418, Feb 2005.

[68] R. P. Campion, K. W. Edmonds, L. X. Zhao, K. Y. Wang, C. T. Foxon, B. L. Gallagher, and C. R. Staddon. The growth of GaMnAs films by molecular beam epitaxy using arsenic dimers. *Journal of Crystal Growth*, 251(1-4):311 – 316, 2003. Proceedings of the Twelfth International Conference on Molecular Beam Epitaxy.

[69] G. Wastlbauer and J. A. C. Bland. Structural and magnetic properties of ultrathin epitaxial Fe films on GaAs(001) and related semiconductor substrates. *Advances in Physics*, 54(2):137–219, Mar 2005.

[70] J. Haigh. *A Study of the Magnetic and Magneto-transport Properties of Fe and GaMnAs*. University of Nottingham, 2012.

[71] CXRO The centre for x-ray optics. Interactions with matter.

[72] Reiko Nakajima, J. Stöhr, and Y. U. Idzerda. Electron-yield saturation effects in L-edge x-ray magnetic circular dichroism spectra of Fe, Co, and Ni. *Phys. Rev. B*, 59(9):6421–6429, Mar 1999.

[73] G. R. Harp, S. S. P. Parkin, W. L. O'Brien, and B. P. Tonner. X-ray magnetic-circular-dichroism study of Fe/V multilayers. *Phys. Rev. B*, 51(5):3293–3296, Feb 1995.

[74] F. Schedin, E. W. Hill, G. van der Laan, and G. Thornton. Magnetic properties of stoichiometric and nonstoichiometric ultrathin Fe_3O_4(111) films on Al_2O_3(0001). *Journal of Applied Physics*, 96(2):1165–1169, 2004.

[75] F. Schedin, P. Morrall, V.N. Petrov, S. Case, M.F. Thomas, E. Dudzik, G. van der Laan, and G. Thornton. Magnetic properties of ultrathin epitaxial Fe_3O_4 films on Pt(111). *Journal of Magnetism and Magnetic Materials*, 211(1-3):266 – 270, 2000.

[76] Luca Signorini, Luca Pasquini, Federico Boscherini, Ennio Bonetti, Isabelle Letard, Sandrine Brice-Profeta, and Philippe Sainctavit. Local magnetism in granular Iron/Iron Oxide nanostructures by phase- and site-selective x-ray magnetic circular dichroism. *Phys. Rev. B*, 74(1):014426, Jul 2006.

[77] K. Olejnik, P. Wadley, J. A. Haigh, K. W. Edmonds, R. P. Campion, A. W. Rushforth, B. L. Gallagher, C. T. Foxon, T. Jungwirth, J. Wunderlich, S. S. Dhesi, S. A. Cavill, G. van der Laan, and E. Arenholz. Exchange bias in a ferromagnetic semiconductor induced by a ferromagnetic metal: Fe/(Ga,Mn)As bilayer films studied by XMCD measurements and SQUID magnetometry. *Phys. Rev. B*, 81(10):104402, Mar 2010.

[78] K. W. Edmonds, A. A. Freeman, N. R. S. Farley, K. Y. Wang, R. P. Campion, B. L. Gallagher, C. T. Foxon, G. van der Laan, and E. Arenholz. Secondary magnetic phases in (Ga,Mn)As determined by x-ray magnetic circular dichroism. *Journal of Applied Physics*, 102(2):023902, 2007.

[79] M. Overby, A. Chernyshov, L. P. Rokhinson, X. Liu, and J. K. Furdyna. GaMnAs-based hybrid multiferroic memory device. *Applied Physics Letters*, 92(19):192501, 2008.

[80] A. Shen, H. Ohno, F. Matsukura, Y. Sugawara, N. Akiba, T. Kuroiwa, A. Oiwa, A. Endo, S. Katsumoto, and Y. Iye. Epitaxy of (Ga, Mn)As, a new diluted magnetic semiconductor based on GaAs. *Journal of Crystal Growth*, 175-176(Part 2):1069 – 1074, 1997. Molecular Beam Epitaxy 1996.

[81] K. Y. Wang, A. W. Rushforth, V. A. Grant, R. P. Campion, K. W. Edmonds, C. R. Staddon, C. T. Foxon, B. L. Gallagher, J. Wunderlich, and D. A. Williams. Domain imaging and domain wall propagation in (Ga, Mn)As thin films with tensile strain. *Journal of Applied Physics*, 101(10):106101, 2007.

[82] K. W. Edmonds, N. R. S. Farley, R. P. Campion, C. T. Foxon, B. L. Gallagher, T. K. Johal, G. van der Laan, M. MacKenzie, J. N. Chapman, and E. Arenholz. Surface effects in Mn L(3,2) x-ray absorption spectra from (Ga,Mn)As. *Applied Physics Letters*, 84:4065, May 2004.

[83] P. R. Stone, M. A. Scarpulla, R. Farshchi, I. D. Sharp, E. E. Haller, O. D. Dubon, K. M. Yu, J. W. Beeman, E. Arenholz, J. D. Denlinger, and H. Ohldag. Mn L_3 x-ray absorption and magnetic circular dichroism in ferromagnetic $Ga_{1-x}Mn_xP$. *Applied Physics Letters*, 89(1):012504, 2006.

[84] K. W. Edmonds, G. van der Laan, A. A. Freeman, N. R. S. Farley, T. K. Johal, R. P. Campion, C. T. Foxon, B. L. Gallagher, and E. Arenholz. Angle-dependent x-ray magnetic circular dichroism from (Ga,Mn)As: Anisotropy and identification of hybridized states. *Physical Review Letters*, 96:117207, 2006.

[85] K. W. Edmonds, G. van der Laan, N. R. S. Farley, E. Arenholz, R. P. Campion, C. T. Foxon, and B. L. Gallagher. Strain dependence of the Mn anisotropy in ferromagnetic semiconductors observed by x-ray magnetic circular dichroism. *Physical Review B (Condensed Matter and Materials Physics)*, 77(11):113205, 2008.

[86] G. van der Laan, R. V. Chopdekar, Y. Suzuki, and E. Arenholz. Strain-induced changes in the electronic structure of $mncr_2o_4$ thin films probed by x-ray magnetic circular dichroism. *Phys. Rev. Lett.*, 105(6):067405, Aug 2010.

[87] P. A. Korzhavyi, I. A. Abrikosov, E. A. Smirnova, L. Bergqvist, P. Mohn, R. Mathieu, P. Svedlindh, J. Sadowski, E. I. Isaev, Yu. Kh. Vekilov, and O. Eriksson. Defect-induced magnetic structure in $(ga_{1-x}mn_x)as$. *Phys. Rev. Lett.*, 88(18):187202, Apr 2002.

[88] K. M. Yu, W. Walukiewicz, T. Wojtowicz, I. Kuryliszyn, X. Liu, Y. Sasaki, and J. K. Furdyna. Effect of the location of Mn sites in ferromagnetic $Ga_{1-x}Mn_xAs$ on its curie temperature. *Phys. Rev. B*, 65(20):201303, Apr 2002.

[89] A. W. Rushforth, N. R. S. Farley, R. P. Campion, K. W. Edmonds, C. R. Staddon, C. T. Foxon, B. L. Gallagher, and K. M. Yu. Compositional dependence of ferromagnetism in (Al,Ga,Mn)As magnetic semiconductors. *Phys. Rev. B*, 78(8):085209, Aug 2008.

[90] E. Sarigiannidou, F. Wilhelm, E. Monroy, R. M. Galera, E. Bellet-Amalric, A. Rogalev, J. Goulon, J. Cibert, and H. Mariette. Intrinsic ferromagnetism in wurtzite (Ga,Mn)N semiconductor. *Phys. Rev. B*, 74(4):041306, Jul 2006.

[91] A. A. Freeman, K. W. Edmonds, N. R. S. Farley, S. V. Novikov, R. P. Campion, C. T. Foxon, B. L. Gallagher, E. Sarigiannidou, and G. van der Laan. Depth dependence of the Mn valence and Mn-Mn coupling in (Ga,Mn)N. *Phys. Rev. B*, 76(8):081201, Aug 2007.

[92] P. Wadley, A. A. Freeman, K. W. Edmonds, G. van der Laan, J. S. Chauhan, R. P. Campion, A. W. Rushforth, B. L. Gallagher, C. T. Foxon, F. Wilhelm, A. G. Smekhova, and A. Rogalev. Element-resolved orbital polarization in (III,Mn)As ferromagnetic semiconductors from K -edge x-ray magnetic circular dichroism. *Phys. Rev. B*, 81(23):235208, Jun 2010.

[93] F. M. F. de Groot, S. Pizzini, A. Fontaine, K. Hämäläinen, C. C. Kao, and J. B. Hastings. Local-spin-selective x-ray absorption and x-ray magnetic circular dichroism of mnp. *Phys. Rev. B*, 51(2):1045–1052, Jan 1995.

[94] F. Matsukura, H. Ohno, A. Shen, and Y. Sugawara. Transport properties and origin of ferromagnetism in (Ga,Mn)As. *Phys. Rev. B*, 57(4):R2037–R2040, Jan 1998.

[95] V. Novák, K. Olejník, J. Wunderlich, M. Cukr, K. Výborný, A. W. Rushforth, K. W. Edmonds, R. P. Campion, B. L. Gallagher, Jairo Sinova, and T. Jungwirth. Curie point singularity in the temperature derivative of resistivity in (ga,mn)as. *Phys. Rev. Lett.*, 101(7):077201, Aug 2008.

[96] M. Sawicki, F. Matsukura, A. Idziaszek, T. Dietl, G. M. Schott, C. Ruester, C. Gould, G. Karczewski, G. Schmidt, and L. W. Molenkamp. Temperature dependent magnetic anisotropy in (Ga,Mn)As layers. *Phys. Rev. B*, 70:245325, Dec 2004.

[97] P Fornasini A Kuzmin G Dalba, D Diop and F Rocca. Exafs and xanes study of GaAs on Ga and As K edges. *J. Phys.: Condens. Matter*, 5:1643–1654, 1993.

[98] Y. Joly. X-ray absorption near-edge structure calculations beyond the muffin-tin approximation. *Phys. Rev. B*, 63(12):125120, Mar 2001.

[99] V. N. Antonov, A. N. Yaresko, and O. Jepsen. X-ray magnetic dichroism in iii-v diluted magnetic semiconductors: First-principles calculations. *Phys. Rev. B*, 81(7):075209, Feb 2010.

[100] G. van der Laan and B. T. Thole. Strong magnetic x-ray dichroism in 2p absorption spectra of 3d transition-metal ions. *Phys. Rev. B*, 43(16):13401–13411, Jun 1991.

[101] A. Titov, X. Biquard, D. Halley, S. Kuroda, E. Bellet-Amalric, H. Mariette, J. Cibert, A. E. Merad, G. Merad, M. B. Kanoun, E. Kulatov, and Yu. A. Uspenskii. X-ray absorption near-edge structure and valence state of Mn in (Ga,Mn)N. *Phys. Rev. B*, 72(11):115209, Sep 2005.

[102] C. Bihler, G. Ciatto, H. Huebl, G. Martinez-Criado, P. J. Klar, K. Volz, W. Stolz, W. Schoch, W. Limmer, F. Filippone, A. Amore Bonapasta, and M. S. Brandt. Local structure of Mn in hydrogenated $Ga_{1-x}Mn_xAs$. *Phys. Rev. B*, 78(23):235208, Dec 2008.

[103] J. G. DeWitt B. Hedman K. O. Hodgson T. E. Westre, P. Kennepohl and J. E. I. Solomon. A multiplet analysis of Fe K-edge $1s \rightarrow 3d$ pre-edge features of iron complexes. *J. Am. Chem. Soc.*, 119:6297–6314, 1997.

[104] J. Kucera N. A. Goncharuk and L. Smrcka. Pre-edge XANES structure of Mn in (Ga,Mn)As from first principles. *Chem. Met. Alloys*, 2:34–38, 2009.

[105] L. M. Sandratskii, P. Bruno, and J. Kudrnovský. On-site coulomb interaction and the magnetism of (Ga,Mn)N and (GaMn)As. *Phys. Rev. B*, 69(19):195203, May 2004.

[106] K. Y. Wang, K. W. Edmonds, R. P. Campion, L. X. Zhao, C. T. Foxon, and B. L. Gallagher. Anisotropic magnetoresistance and magnetic anisotropy in high-quality (Ga,Mn)As films. *Phys. Rev. B*, 72(8):085201, Aug 2005.

[107] M. A. Scarpulla, B. L. Cardozo, R. Farshchi, W. M. Hlaing Oo, M. D. McCluskey, K. M. Yu, and O. D. Dubon. Ferromagnetism in $Ga_{1-x}Mn_xP$: Evidence for inter-Mn exchange mediated by localized holes within a detached impurity band. *Phys. Rev. Lett.*, 95(20):207204, Nov 2005.

[108] K. F. Eid, M. B. Stone, K. C. Ku, O. Maksimov, P. Schiffer, N. Samarth, T. C. Shih, and C. J. Palmstrøm. Exchange biasing of the ferromagnetic semiconductor $Ga_{1-x}Mn_xAs$. *Applied Physics Letters*, 85(9):1556–1558, 2004.